The Dissertation Committee for Naresh Neupane Certifies that this is the approved version of the following dissertation:

Understanding Precipitation Changes over West Africa and North America under Global Warming and Identifying a Congo Basin Walker Circulation

Committee:

Kerry H. Cook, Supervisor

Robert E. Dickinson

Rong Fu

Charles S. Jackson

Bridget R. Scanlon

Understanding Precipitation Changes over West Africa and North America under Global Warming and Identifying a Congo Basin Walker Circulation

by

Naresh Neupane, M.S.

Dissertation

Presented to the Faculty of the Graduate School of

The University of Texas at Austin

in Partial Fulfillment

of the Requirements

for the Degree of

Doctor of Philosophy

The University of Texas at Austin

May, 2015

Acknowledgements

My deepest appreciation goes to my advisor Kerry H. Cook. For me, she started right from the basics of Atmospheric Science. She always inspired me to pay close attention to my research and constantly motivated me to remain focused on the topic. Thank you Kerry for providing me all the careful suggestions and guidance, and for pointing my mistakes and weaknesses. Pursuing graduate studies was definitely not an easy ride for me, I had to face many unexpected situations in the past six years, thank you for your support in all aspect of my life and finally thank you for making this dissertation possible.

The other person, who has had a great influence upon me and has always been helpful in my research would have to be Edward K. Vizy (Ned). Thank you Ned for teaching me how to run WRF (Weather Research and Forecasting) model. Without learning WRF, these researches would not have been possible. Apart from technical help, I have tremendously benefitted from your scientific comments and suggestions.

The classes taught by Charles Jackson, Rong Fu, Robert E. Dickinson, Zong-Liang Yang, and Kerry H. Cook were very helpful and provided me the fundamental understanding of atmospheric science.

I would like to thank Samson Hagos and Lai-yung Ruby Leung at Pacific Northwest National Laboratory for providing me the opportunity to be an intern during the summer of 2012. The summer was intellectually enriching, and I also had an opportunity to hone my skill in Matlab and parallel computing.

Thanks to my mother, Bhagawati Neupane, and father, Kashi Nath Neupane, for their never ending encouragement and support. Thanks to my wife, Sagun Bhattarai, who has always inspired me in doing what I really love to do. Thanks to my brother Suresh Nath Neupane and sister Sirjana Suraiya for their inspiration. Thanks to the Jackson School of Geosciences and this beautiful city of Austin, where we were blessed with a son, who we named, Vedanta Krishna Neupane.

Furthermore, I would like extend my sincere thanks to Ravi Ale, Utsav K.C., Naween Dahal, Kumar Mainali, Prabhat Bhattarai, Sagar Parajuli, Sudip Chakraborty, Gang Zhang, Bing Pu, and Christina Patricola.

Understanding Precipitation Changes over West Africa and North America under Global Warming and Identifying a Congo Basin Walker Circulation

Naresh Neupane, Ph.D.

The University of Texas at Austin, 2015

Supervisor: Kerry H. Cook

Studies have shown that the Atlantic Ocean affects West African rainfall. However, the response of the West African monsoon to Atlantic warming is not understood clearly. My dissertation explores this by analyzing idealized simulations with a regional climate model. Below 1.5 K warming of the Atlantic, rainfall increase by 30-50% over the Sahel. In contrast, above 2 K, rainfall decreases substantially. Atlantic warming is accompanied by decreases in low-level geopotential heights in the Atlantic decreasing the large-scale meridional geopotential height gradient across West Africa. This leads to easterly wind anomalies in the Sahel. Below 2 K, these easterly anomalies allow moisture transport to the Sahel. Above 2 K, the easterly anomalies reverse the westerly flow and reduce precipitation in the Sahel.

Models predict increases of precipitation in the future under global warming. Theoretical understanding of this is founded in the Clausius–Clapeyron equation. I compare precipitation from the theory with the model simulations over the U.S. for the mid-21st century and investigate the physics of the departure of the model from theory. In the spring and fall precipitation increases, up to 30%/ K, and the modeled precipitation

matches the theoretical prediction. In contrast, rainfall lowers and prediction fails in the summer. These differences are associated with the soil moisture distributions. Associated with the increased soil moisture, model follows theoretical prediction in the spring and fall, while reduced soil moisture is associated with failure of the theoretical prediction in the summer.

The Gulf of Guinea in the eastern Atlantic shows subsidence. This subsidence becomes well established in the low-level from July–September. Using observations, I contribute to understanding its cause and relationship with the regional precipitation and circulation. This subsidence is associated with the subsiding-branch of a Congo basin Walker circulation identified here. The circulation has a rising-branch over the Congo basin, and is driven by temperature gradient. Basin temperature remains almost uniform throughout the year, but in association with the Atlantic cold tongue formation, Guinean temperature cools up to -4 K in the summer. This gradient drives the circulation. A strong Walker circulation is associated with enhanced northward moisture transport.

Table of Contents

List of Table

List of Figures

Chapter 1: General Introduction

This dissertation is structured into five chapters. The first chapter provides a general introduction to the succeeding three chapters, which correspond to three independent manuscripts. The first chapter is already published in the Journal of Climate and the rest manuscripts are in process of submission. General conclusions are drawn in the fifth chapter.

Considering West African's dependence on summer rainfall for agricultural practices, it is important that we understand the response of the West African monsoon (WAM) to global warming. Past observations and paleo-climate proxy evidence suggests that the WAM system is susceptible to abrupt changes from characteristically wet to dry conditions (Gasse and Van Campo 1994; Petit-Maire and Guo, 1996). Even the evolution of the WAM system and the northward migration of rainfall from the Guinean Coast into the continental interior (i.e., the WAM jump) exhibit signs of abrupt transitions (Sultan and Janicot 2003; Hagos and Cook 2007). These indicate that the West African climate is susceptible to abrupt changes in the future.

Understanding that several factors, such as solar radiation (deMenocal and Rind, 1993; De Menocal 2000), global SSTs (Meehl et al. 2007), aerosols (Rosenfeld et al. 2001), and land surface /vegetation (Li et al. 2007) can influence the evolution of the WAM and rainfall distributions across West Africa, here I segregate one aspect of the problem, which is the Atlantic SSTs.

In the second chapter, I focus on better understanding the variability of the Sahelian precipitation related to warming of Atlantic SSTs only. The Atlantic Ocean is selected because it is known to be one of the most important sources of moisture for the West African monsoon and it is more influential to the Sahelian rainfall than the other factors (Folland et al. 1986; Fontaine and Janicot 1996; Vizy and Cook 2001; Giannini et al. 2003).

The next chapter of this dissertation is on understanding future increases in precipitation over the U.S. In association with increased greenhouse gases, climate models project increases of mean precipitation (Meehl et al. 2000; Cubasch and Meehl 2001; Wilby and Wigley 2002). An understanding of these increases is based upon the Clausius–Clapeyron relation, which indicates that a 1 K increase in surface temperature will be accompanied by approximately a 7% increase in the saturation mixing ratio along with the relative humidity remaining approximately constant as the climate warms.

In the third chapter, the theoretical prediction of precipitation from the Clausius-Clapeyron relation is compared with the modeled precipitation for the mid-21st century. Using a regional climate model, physics of the departure of the modeled precipitation from the theory is explored on regional and seasonal space scales. Simulation output provided by Patricola and Cook (2012a, 2012b) is used in this study, and the study area is North America.

The fourth chapter again focuses over the African continent. Present-day climate conditions show that there is atmospheric subsidence over the Gulf of Guinea in the eastern equatorial Atlantic. This subsidence appears over the Gulf of Guinea during the West African monsoon season, which is from July-September. Also, the Gulf of Guinea is an

important source of moisture for the WAM system (Vizy and Cook 2001, 2002; Cook and Vizy 2006; Neupane and Cook 2013). Understanding the presence of this subsidence and its impact upon precipitation across West Africa is important for present and assessing impacts for the future. Despite its potential implications upon moisture and precipitation distributions across West Africa, this subsidence remains poorly documented and rarely explored.

In this chapter, I document the presence of this seasonal scale subsidence in the Gulf of Guinea. Then, motivated to understanding the cause of this subsidence, as a consequence, a seasonal Walker circulation above the Gulf of Guinea and the Congo basin is identified and the relationship between the Walker circulation and rainfall across West Africa is explored.

Chapter 2: A nonlinear response of Sahel rainfall to Atlantic warming[1]

2.1 ABSTRACT

The hydrodynamics of the response over West Africa to uniform warming of the Atlantic Ocean is analyzed using idealized simulations with a regional climate model. With modest warming of 1 K and 1.5 K, rainfall rates increase by 30-50% over most of West Africa. With Atlantic warming of 2 K and higher, coastal precipitation still increases but Sahel rainfall decreases substantially. This nonlinear response in Sahel rainfall is the focus of the analysis.

Warming in the Atlantic Ocean is accompanied by decreases in low-level geopotential heights in the Gulf of Guinea and decreases the large-scale meridional geopotential height gradient across West Africa. By geostrophic argument, this leads to easterly wind anomalies in the central Sahel. With Atlantic warming below 2 K, these easterly anomalies allow moisture transport from the Gulf of Guinea to penetrate farther north over the western Sahel, and this leads to precipitation increases in that region. With Atlantic warming of 2 K and above, the easterly anomalies reverse the westerly flow over

---

[1] This chapter was published in Journal of Climate: Neupane, N., and K. H. Cook, 2013: A nonlinear response of Sahel rainfall to Atlantic warming. *J. Climate,* **26,** 7080–7096. Idea of this project was conceived by Kerry H. Cook. Model simulations were performed and figures were prepared by Naresh Neupane. This chapter is jointly written by the authors.

the Sahel. The result is dry air advection into the Sahel and precipitation reductions. Increased low-level moisture provides moist static energy to initiate convection with Atlantic Ocean warming at 1.5 K and below, while decreased moisture and stable thermal profiles suppress convection with additional warming. In all of the simulations, the southerly monsoon flow onto the Guinean coast is maintained, and precipitation in that region increases.

The relevance of these results to the global warming problem is limited by the focus on Atlantic warming alone. However, confident prediction of climate change requires an understanding of the physical processes of change, and this paper contributes to that goal.

2.2. INTRODUCTION

An improved understanding of the physical processes associated with climate change in West Africa and the Sahel is needed for producing reliable predictions to aid resource management and planning as the planet warms. Nonlinear responses in the climate system can lead to surprises and even abrupt climate change, presenting greater challenges for adaptation. Paleoclimate proxy data show that the West African climate is prone to rapid changes between wet and dry conditions. Even the seasonal evolution of the monsoon system is characterized by abrupt transitions since the northward migration of rainfall from the Guinean Coast into the Sahel does not occur smoothly.

The purpose of this paper is to contribute to an improvement in our physical understanding of how the West African monsoon will respond under global warming. We isolate one aspect of the problem, namely, the hydrodynamics of the response to uniform warming of the Atlantic Ocean within the model domain (58°W–48°E and 19°S–34°N;

Section 3). Forcing from the Atlantic Ocean is chosen because of the known sensitivity of the monsoon system to Atlantic sea surface temperature anomalies (SSTAs). Uniform warming is chosen for simplicity and clarity, and because the modeling results of Patricola and Cook (2011) indicate that much of the global warming signal forced from the Atlantic in West Africa and the Sahel is due to uniform warming, with a dependence on structure in the SSTAs present only along the west coast.

Climate change and variability in West Africa and the Sahel is complicated, with demonstrated dependence on SSTAs in the Indian, Atlantic, and Pacific Oceans, land surface feedbacks, aerosol forcing, midlatitude/tropical interactions, and other factors – and we do not mean to imply otherwise by focusing on Atlantic sea surface temperatures (SSTs) forcing alone. However, confident prediction of twenty-first-century climate change in the region requires that we build a solid understanding of the physical processes of that change, and here we contribute to that goal in a process study that isolates the response to uniform Atlantic SSTAs.

Background is provided in Section 2, including an overview of the region's sensitivity to Atlantic SSTs and our current understanding of the potential for change under greenhouse gas forcing. The regional climate model and experimental design are described in Section 3, and the model is validated against observations, reanalysis, and satellite measurements in Section 4. Results are reported in Section 5, and conclusions and implications are discussed in Section 6.

2.3. BACKGROUND

Paleoclimate proxy data show that the West African climate can change substantially on millennial time scales. For example, 14.8 – 5.5 ka is known as the African Humid Period (AHP), when the western Sahel and Sahara received rainfall sufficient to support large lakes, small trees, and large fauna such as hippopotamus (e.g., Gasse and Van Campo 1994, Petit-Maire and Guo 1996). The onset of the AHP was associated with some major atmospheric changes. For example, the atmospheric CO_2 concentration increased by about 50 ppmv, the Atlantic meridional overturning circulation (AMOC) weakened and the northern ice sheets retreated during the onset, and summer insolation in the Northern Hemisphere was about 5% greater than today at 8ka (White et al. 1994, Monnin et al. 2001, McManus et al. 2004).

Of potential relevance to the development of the global warming response over West Africa and the Sahel is the ability of the region's climate to change abruptly. For example, the transition into and out of the AHP was abrupt, at least in some regions, occurring within decades to centuries despite gradual and smooth changes in the precessional forcing of insolation (e.g., deMenocal et al. 2000, Russell et al. 2003, Peck et al. 2004). Also, in a more recent model simulation, Timm et al. (2010) demonstrate that the abrupt onset of the AHP was due to the combined effects of increases in local insolation and drastic melting of the Northern Hemisphere ice sheets.

Paleoclimate studies also provide an indication of the sensitivity of the West African climate to Atlantic SSTs. The African Humid Period was interrupted by an arid interval corresponding to the Younger Dryas event (~ 12.9 – 11.5 ka), when a weakening

of the AMOC occurred in response to a sudden influx of fresh water from deglaciation in North America (Alley 2000; Lowell et al. 2005). Heinrich events are also reflected in African paleoclimate records; there is evidence that North Atlantic cooling at 17 ka associated with Heinrich event 1 caused a wide-spread drought in the African monsoon region (Stager et al. 2011).

Present-day climate records also indicate that the West African climate is sensitive to Atlantic SSTs (e.g., Folland et al. 1986, Fontaine and Bigot 1993, Camberlin et al. 2001, Liu and Chiang 2012). One particular SSTA forcing pattern known to influence West Africa rainfall is centered in the Gulf of Guinea, where the onshore monsoon flow originates. With positive SSTAs of 1-2 K in the Gulf of Guinea, rainfall is enhanced along the Guinean coast and suppressed in the western and central Sahel (Ward 1998, Nicholson 2000, Mo et al. 2001). An opposite pattern occurs with cool SSTAs in the Gulf of Guinea. Vizy and Cook (2001, 2002) explain the physics of this mechanism. Evaporation is enhanced over the warm SSTAs, but a precipitation anomaly does not develop over the ocean because of regional subsidence associated with the Walker circulation. As a consequence, the moisture content of the northward monsoon inflow is increased along with rainfall along the coast. Anomalous subsidence and drying in the Sahel is a secondary response to enhanced rainfall along the coast generated by conservation of potential vorticity requirements.

Although the focus of this paper is on the physics of the response to uniform Atlantic Ocean warming, many factors are known to influence precipitation over West Africa. These include changes in SST patterns in the Atlantic (e.g., Mohino et al. 2011a),

SSTAs in the Pacific and Indian Oceans (e.g., Paeth and Friederichs 2004, Hagos and Cook 2008, Mohino et al. 2011b), changes in land surface/vegetation (e.g., Li et al. 2007, Patricola and Cook 2008), aerosol forcing (e.g., Gu et al. 2012, Joseph and Zeng 2011, Zhao et al. 2011) , and relative positions of the African easterly jet and the tropical easterly jet (Nicholson 2009). Since the model domain does not include the Indian and Pacific Oceans, the impacts of large scale circulations such as the Madden-Julian Oscillation, the El Niño-Southern Oscillation, and the Indian summer monsoon on the West African monsoon are not included.

The need to improve our basic understanding of the physics of the African monsoon's response to climate forcing is evident in the uncertainty about how the region's rainfall will change in the future (Biasutti and Giannini 2006, Biasutti et al. 2008, Cook 2008). Cook and Vizy (2006) examined output from 18 coupled GCMs from CMIP3 (Coupled Model Intercomparison Project 3; Meehl et al. 2007) over West Africa. Half of the CMIP3 simulations failed to produce the West African monsoon at all in the sense that they did not bring the summer precipitation maximum onto the continent. Three GCMs were selected based on their ability to represent major features of the twentieth century climate, including its variability. But in the future simulations, these three models diverged widely, demonstrating that a reasonable simulation of the present climate is not a sufficient condition for accurate projection. Inclusive analyses of the CMIP3 coupled GCMs (Cook 2008) shows that most of the CMIP3 models predict only small increases or decreases of annual precipitation over West Africa by the end of the century.

There is no overall improvement in simulating the West African monsoon system in the coupled GCMs from the CMIP5 (Vizy et al. 2012). Some GCMs, such as CCSM4 (Cook et al. 2012), produce an improved representation over West Africa compared with the CMIP3, but in other models the simulation is worse. Maynard et al. (2002) used a coupled GCM to simulate African climate at the end of the 21st century under the IPCC B2 scenario and found that the summer monsoon precipitation over the Sahel increases.

Patricola and Cook (2010, 2011) use a regional model at 90-km resolution centered over West Africa to produce two, 9-member ensembles for the end of the 20th and 21st centuries, with boundary conditions for future simulations applied as anomalies based on output from nine coupled GCM. Despite the differences in SSTAs and lateral boundary conditions in the nine GCMs, there is good agreement in the predictions over most of West Africa and the Sahel among the nine ensemble members. Annual precipitation changes are relatively small, similar to the CMIP3 multi-model ensemble mean (Cook 2008), but regional and monthly analysis reveals large changes in temperature, heat stress, precipitation, and extreme rainfall events that would produce pronounced impacts. In particular, rainfall in the Sahel increases in July and August, and decreases along the Guinean coast in June and July.

The reason for the agreement among the ensemble members in the regional model simulations of Patricola and Cook (2010) is that the first-order response over West Africa and the Sahel at the end of the twenty-first-century is to overall ocean warming, which is demonstrated by an additional simulation with uniform SSTAs of 2 K. The changes in precipitation in the uniform warming case are similar to those from the ensemble mean

across West Africa and the Sahel, with the only exception in the far western Sahel where the response is sensitive to the structure of the imposed SSTAs.

Building on these results, we explore the physics of the response to uniform Atlantic warming alone in a series of idealized simulations. We are particularly interested in identifying and understanding non-linearity in the monsoon system's response to gradual warming, since these can be a source of abrupt change.

2.4. MODEL DESCRIPTION AND EXPERIMENTAL DESIGN

The National Center for Atmospheric Research (NCAR) advanced Weather Research and Forecasting model (WRF) v. 3.1.1 is used for this study (Skamarock et al. 2008). The model is fully compressible and non-hydrostatic, with 28 vertical levels in this case. The top of the model is set to 50 hPa. The model is used at a spatial resolution of 90 km with a time step of 3 minutes.

The outcome of past regional climate modeling efforts over Africa (e.g., Vizy and Cook 2002, 2003; Patricola and Cook 2010, 2011) and extensive testing were used to select parameterizations, a model domain, and lateral and surface boundary conditions that produce a realistic simulation of the present day West African climate. Parameterizations chosen include the Mellor-Yamada-Janjic planetary boundary layer scheme (Mellor and Yamada 1982; Janjic 1990, 1996, 2002), the Monin-Obukhov Janjic surface layer scheme (Monin and Obukhov 1954; Janjic 1994, 1996, 2002), the new Kain-Fritsch cumulus scheme (Kain and Fritsch 1990, 1993), the Purdue-Lin microphysics scheme (Lin et al. 1983), the rapid radiative transfer model longwave radiation parameterization (Mlawer et

al. 1997), the MM5 shortwave parameterization (Dudhia 1989), and the unified NOAH land surface model (Chen and Dudhia 2001).

Figure 1 shows the model domain selected for this study. The large domain minimizes the effects of the lateral boundaries on the region of interest. It includes most of northern Africa as well as the tropical and eastern North Atlantic.

Initial and lateral/surface boundary conditions for all simulations are initialized at 00Z on 15 March using climatological March conditions interpolated onto the regional model grid. Lateral boundary conditions for horizontal winds, temperature, relative humidity, and geopotential height are derived from the 1958-2001 NCEP/NCAR reanalysis (Kalnay et al. 1996) monthly climatology. Initial surface boundary conditions for skin temperature, soil temperature, soil moisture, and sea-level pressure are derived from the ECMWF 1958-2001 ERA 40 reanalysis monthly climatology (Uppala et al. 2005). The ERA 40 reanalysis is used for the surface initialization instead of the NCEP reanalysis climatology because the NCEP reanalysis has a cold and wet bias over the Sahara. Patricola and Cook (2010) show that WRF produces a more realistic simulation of the monsoon when ERA 40 surface conditions are used to initialize the simulation.

Lateral boundary conditions are updated every 6 hours using the NCEP reanalysis climatology interpolated onto the model boundaries. Monthly mean values from the reanalysis are taken to represent the middle of the month, and linear interpolation in time is used to generate 6-hourly boundary conditions. Boundary conditions produced by this method include seasonality, but diurnal and synoptic timescales are suppressed. This "climate-mode" approach works for large domains in the tropics (Cook and Vizy 2008,

Hagos and Cook 2007, Patricola and Cook 2010), but fails for applications in middle latitudes where transients propagating into the domain are important for determining the time mean state (Patricola and Cook 2012a and b, Pu et al. 2012). Seven 231-day simulations (15 March–31 October) are produced, and 3 hourly output is averaged to generate daily and monthly means. This period covers the entire evolution of the boreal summer monsoon. The first 2.5 months of each simulation, from 15 March to 31 May, are devoted to model spin–up and not used in the analysis. Such a long period for spin–up is necessary to avoid errors associated with the persisting initial soil moisture properties (Simmonds and Hope 1998).

A control simulation, referred to as CTL, uses climatological SSTs that are prescribed and updated every 6 hours. These 6-hourly SSTs are derived from the 1958-2001 ERA 40 reanalysis monthly climatology using the same linear interpolation method discussed above for the lateral boundary conditions. Six additional simulations are produced with uniform Atlantic SSTAs added to the climatological SSTs, but otherwise identical to CTL. These SSTs preserve the structure of current Atlantic SST gradients, but create an overall warmer ocean basic state. Uniform positive SSTAs are applied in six additional simulations referred to as 1K, 1.5K, 2K, 2.5K, 3K, and 4K.

2.5. MODEL EVALUATION

Figure 2 shows boreal summer monthly rainfall from the 0.25°-resolution NASA Tropical Rainfall Measuring Mission (TRMM 3B42V6) satellite-derived 1998–2009 climatology (Kummerow et al. 1998), the 0.5°-resolution Climate Research Unit (CRU; CRUTS3.0) 1979–2006 climatology (Mitchell and Jones 2005) over land and the 2.5°-resolution Global Precipitation Climatology Project (GPCP; Adler et al. 2003) 1979–2006 climatology over the ocean, and the control simulation. Each climatology is presented at its original resolution to preserve as much spatial information as possible. The regional model simulation is able to realistically capture the seasonal migration of rainfall over West Africa, including the movement of the precipitation maximum into the continental interior that is often missed in coupled GCMs.

Overall, the simulated rainfall intensity is larger than observed. This wet bias varies based on location and can range from 2 to more than 18 mm/day. For example, over the far western Sahel (6°W-12°W and 10°N-12°N) the difference between the simulated and observed precipitation is approximately 8 mm/day in July and 4 mm/day in August. Also, the summer precipitation minimum over the Guinean Coast in July and August is more pronounced in the control simulation compared to the TRMM and CRU climatologies.

The accuracy of the simulated rainfall distribution is similar to that of the most accurate GCMs in this region, and better than most GCM simulations. This includes the sudden shift of the rainfall maximum from the Guinean coast into the Sahel in early July known as the monsoon jump (not shown).

925-hPa June geopotential heights and winds from the 1989-2010 ERA-Interim reanalysis climatology at 1.5° resolution (Dee et al. 2011) and the control simulation are shown in Figs. 3a and b, respectively. The summertime thermal low has developed over the central Sahel and Sahara in the reanalysis (Fig. 3a). The model (Fig. 3b) produces geopotential heights of realistic magnitude, but the low is centered farther north and west than in the reanalysis. The position and strength of the North Atlantic subtropical high are realistically simulated, but the onshore flow along the Guinean and west coasts are stronger in the model simulation than in the reanalysis. The West African westerly jet (Grodsky et al. 2003; Pu and Cook 2010, 2011) near 8°N is in place on the west coast in the model, earlier than its formation in the reanalysis.

Figures 3c and d show reanalysis and model 925-hPa geopotential heights and winds for July through September. The magnitude of the thermal low is captured accurately in the simulation, but it is located about 5° south of its center in the reanalysis. The West African westerly jet has moved a few degrees north in the simulation, and formed in the reanalysis; it is stronger in the model. [Higher-resolution reanalyses available for individual years capture the West African westerly jet more strongly than the ERA-Interim product.] Other features of the low-level flow are captured in the model with good accuracy.

Figures 4a and b show geopotential heights and winds at 600 hPa from the ERA-Interim reanalysis climatology and the control simulation for June. The mid–tropospheric Saharan anticyclone is centered near 23°N and 0°E in the reanalysis (Fig. 4a), and only

slightly west of that position in the simulation (Fig. 4b). The African easterly jet has formed and is realistically simulated.

In the July-September mean, the Saharan high expands northward over the Sahara in both the reanalysis and the model (Figs.4c and d) compared with the June average, positioning the African easterly jet a little farther north consistent with the repositioning of geopotential height, surface temperature, and moisture gradients (Cook 1999).

In summary, the regional model produces a state-of-the-art representation of the major circulation and precipitation features of the West African climate and their seasonal evolution.

2.6. RESULTS

2.6.1 The dependence of West African precipitation anomalies on Atlantic Ocean warming

Figure 5a shows July–September precipitation differences between the control simulation and the simulation with 1 K SSTAs in the Atlantic, denoted "1K-CTL". Rainfall rates are enhanced by 2 - 6 mm/day along the Guinean coast and on the west coast south of 15°N, and over the western Sahel. There are negative precipitation anomalies up to 2 mm/day north of the Guinean coast (near 5°W and 12°N) and in the central Sahel (10°E and 14°N). Differences are small north of 20°N.

Figure 5b shows summer rainfall anomalies for 1.5K-CTL. Positive rainfall differences in the western Sahel are greater by up to 2 mm/day than in the 1K-CTL case (Fig. 5a), but the spatial structure and magnitudes of the precipitation anomalies are similar.

Precipitation increases on the west coast and the Guinean coast are further enhanced in the 2K case (Fig. 5c). The two small regions of drying in Figs. 5a and b are also larger, and the drying in the central Sahel extends to the west. The positive anomalies between 13°N and 15°N near the Greenwich meridian in Figs. 5a and b are now replaced with negative anomalies.

Negative precipitation anomalies over the central Sahel continue to strengthen and extend westward with additional Atlantic warming. Figures 5d-f display precipitation differences for 2.5K-CTL, 3K-CTL and 4K-CTL, respectively. Each produces a response similar in structure to the 2.5K simulation, but with larger anomalies and more extensive Sahel drying. Rainfall rates over the west coast and Guinean coast increase by more than 18 mm/day in the 2.5K simulation, for example, and rainfall rates over the Sahel decrease by up to 10 mm/day in 3K and 4K simulations.

Figure 6a shows percentage differences in summer (July–September) precipitation averaged from 12°W to 6°E over West Africa for 1K-CTL. Each bar represents a one degree latitude band, and Sahel latitudes (13°N-16°N) are shaded. Rainfall rates increase up to 35% over West Africa between 8°N and 10°N. They do not change, or decrease slightly, between 10°N and 13°N. North of 13°N, precipitation rates increase everywhere. The largest percentage change occurs between 16°N and 19°N where rainfall rates increase by 90–167%.

Figure 6b displays the results for 1.5K-CTL. Between 8°N and 16°N, the response is similar to the 1K-CTL differences (Fig. 6a). Rainfall increases are not as large as in the 1K case north of 17°N.

With 2K warming in the Atlantic (Fig. 6c), precipitation increases between 8°N and 12°N are a little larger than with 1.5K warming but similar in structure, but there is a sign change in the precipitation anomaly over the Sahel. The 1.5K case has 4–66% precipitation increases between 12°N and 17°N, but Sahel rainfall rates in the 2K simulation decrease by 3–18%. Percentage precipitation enhancements north of 17°N are greater than in the 1K and 1.5K cases.

Figure 6d-f display precipitation differences for the 2.5K-CTL, 3K-CTL and 4K-CTL simulations, respectively. Precipitation differences between 8°N and 11°N are positive, between 38% and 140% in the 2.5K simulation and 45% to 225% in the 3K case. The Sahel drying that was relatively modest in the 2K simulation (Fig. 6c) is larger and more extensive with 2.5K Atlantic warming, with precipitation increases north of 17°N replaced by drying. With greater Atlantic warming, the same pattern of drying in the Sahel persists, becoming more severe and spreading southward.

Figure 6 demonstrates that the precipitation response to Atlantic SSTAs over the Sahel is nonlinear. For Atlantic SST increases up to +1.5K, Sahel rainfall rates increase. When the warming reaches and exceeds +2K, Sahel rainfall decreases. The existence of a threshold Atlantic SSTA between 1.5K and 2K in the model complicates climate prediction and suggests a possibility for abrupt climate change over the Sahel in association with SST forcing from the Atlantic Basin.

Reference to Fig. 5 indicates that there is some regional dependence for the threshold warming value. In general, rainfall rates increase (decrease) west (east) of 6°W from 12°N–19°N in all of the warming simulations. In the Sahel, rainfall rates increase

from 6°W–12°W in 1K and 1.5K, but decrease with warming of 2K and higher. In 1K and 1.5K, overall increases are offset by a simulated decrease east of 6°W. However, from 17°N–19°N, the decrease east of 6°W does not offset the increase over the western portion of the averaging region until SSTAs exceed 2.5 K. This regional increase in rainfall rates west of 6°W is largely confined to the month of August.

Two other recent model simulations have been conducted with uniform SST increases, both with 2 K warming. Held et al. (2005) simulated annual mean drying in the Sahel, especially from 10°N–15°N, in an atmospheric GCM. Patricola and Cook (2010, 2011) found that JAS Sahel rainfall decreased, especially during July, up to 6 mm/day in response to uniform Atlantic warming in a regional climate model. These results are consistent with the 2K simulation presented here.

To focus on the mechanisms of this nonlinear dependence on Atlantic SSTAs, we examine the 26 June to 26 July time period. This time period is largely responsible for the fact that Sahel JAS rainfall is less in 2K than in 1K and 1.5K (not shown). Average daily precipitation over the Sahel in this period in the CTL simulation is about 5 mm/day. It increases to about 8 mm/day in 1.5K, and decreases to about 3 mm/day in 2K. At the end of July, rainfall rates in the 2K simulation are greater than in CTL. During the rest of the summer (e.g., August and September) rainfall rates in the CTL, 1.5K, and 2K simulations are similar.

Figure 7 displays rainfall differences for four of the warming simulations averaged from 26 June to 26 July. As was the case for the full summer average (Figs. 5a and b), the basic spatial structure of rainfall anomalies over the Sahel in the 1K (Fig. 7a) and 1.5K

(Fig. 7b) simulations is similar. Precipitation differences in the southern Sahel (near 13°N) and the eastern Guinean coast region are greater in the 1.5K simulation than in the 1K simulation, as is the rainfall reduction in the central Sahel (along 14°N east of 6°W).

Precipitation decreases in the central Sahel become more pronounced with Atlantic warming of 2K and 2.5K (Figs. 7c and d), and the dry anomalies extend to the west. As Atlantic SSTAs are increased above 2.5K, the drying becomes stronger but the spatial structure is similar to the 2K and 2.5K cases (not shown). Precipitation over the Gulf of Guinea increases in all the Atlantic warming simulations.

2.6.2. The hydrodynamic response to small Atlantic SSTAs: The 1K and 1.5K simulations

The hydrodynamics of the West African and Sahel precipitation increases with Atlantic warming less than 2 K is examined first, and then compared with the response to SSTAs of 2K and greater in the following section to understand the sign change in the response,

Figure 8a shows winds and geopotential heights at 925 hPa averaged from 26 June – 26 July from the CTL simulation. The southerly monsoon flow from the Gulf of Guinea flows into the Guinean coast region and turns southwesterly over the continent under the influence of Coriolis accelerations. The West African westerly jet is in place on the west coast centered near 10°N (Grodsky et al. 2003, Pu and Cook 2010). The pronounced meridional gradients that characterize the region (Fig. 3) are strongest between 9°N and 17°N.

Difference fields for 1.5K-CTL are shown in Fig. 8b. Here, the differences in 925 hPa geopotential heights are normalized by the domain-averaged difference of 13.4 gpm to highlight changes in gradients. The anomalous geopotential height gradient is positive, indicating a weakening of the negative climatological gradient (Fig. 8a). This weakening is greatest in the Sahel, centered around 15°N, and it is accompanied by a westward wind anomaly of up to 2 m/s indicating that the eastward curvature of the flow over the Sahel (Fig. 8a) is reduced. Warming in the Atlantic Ocean – and, in particular, in the Gulf of Guinea – decreases the large-scale meridional geopotential height gradients across West Africa. As a result, the southerly monsoon flow onto the Guinean coast is not diverted to the east as strongly, and it penetrates farther north. This leads to the precipitation increases in the western Sahel in the 1K and 1.5K simulations, and also to the small region of decreased precipitation in the central Sahel (Figs. 5a and b).

Another consequence of the decreased magnitude of the large-scale meridional geopotential height gradients across the Sahel is a weakening of the African easterly jet. Figure 9 displays the cross-section of the difference in the zonal wind averaged from 12°W to 6°E for 1.5K-CTL. Easterly wind anomalies occur below 700 hPa throughout the domain, consistent with Fig. 8b. The positive (westerly) anomalies centered near 13°N and 550 hPa indicate a weakening of the African easterly jet by more than 2 m/s in the 1.5K simulation. The African easterly jet is a result of strong coupling between the atmosphere and land surface over the Sahel, and it weakens as a result of geostrophic dynamics (via the thermal wind relation) when meridional temperature gradients below the level of the jet also weaken (Cook 1999). In these simulations there is no shift in the position of the

African easterly jet, which is known to be associated with Sahel rainfall variations on interannual time scales (Nicholson and Grist 2001).

The increases in Guinean coast precipitation in response to Atlantic Ocean warming (Figs. 5a and b) are not fully explained by examining differences in the low-level flow in Figs. 8a and b. The southerly monsoon flow onto the Guinean coast is increased in magnitude somewhat and turned to the northwest by the warming of the Atlantic Ocean, with anomalous convergence along the coast; the West African westerly jet is weaker in the 1.5K simulation than in CTL. To fully understand the response on the coast, atmospheric moisture fields must be considered.

Figure 10a displays 925-hPa mixing ratios and moisture transport from the CTL simulation averaged over 26 June to 26 July. Similar to Simmonds et al. (1999), moisture flux is expressed as the sum of mean and the transient eddy components. The transient eddy component, however, is negligible in this case. While some moisture is transported onto the continent in the southerly monsoon flow, reduced evaporation associated with the relatively cool temperatures of the Atlantic cold tongue lower the moisture content of the southerly flow. A primary source of moisture for the Sahel at this time of year is the West African westerly jet (Pu and Cook 2011). As seen in the difference fields (Fig. 10b), mixing ratio values over the Gulf of Guinea double when 1.5 K warming is imposed in the Atlantic Basin. Warming of the sea surface combined with the low-level winds of the monsoon circulation (Fig. 8a) drive enhanced evaporation. The increased moisture content of the inflowing monsoon circulation fuels the Guinean coast precipitation increases. Note

also the anomalous westward moisture transport from the central Sahel to the western Sahel that is associated with the wind anomalies shown in Fig. 8b.

It may seem counterintuitive that rainfall rates over the Guinean coast increase when Atlantic SSTs are warmed if one thinks about this region's rainfall as being supported by a monsoon circulation that is ultimately related to the juxtaposition of a cooler ocean surface and a warmer land surface, since warming the ocean would decrease the land/sea temperature contrast in the summer (all other factors remaining the same). This mechanism operates on large space scales and leads to increases in rainfall in the western Sahel in response to these mild SSTAs, as discussed above. But along the Guinean coast, the precipitation increase is explained through the moisture budget analysis. When Gulf of Guinea SSTs increase, evaporation rates and low-level moisture levels also increase over the SSTAs, but local precipitation rates are not enhanced because of the presence of subsidence in this region. As seen in Figure 11 from the CTL simulation, and similar to the reanalyses (not shown), subsiding air over the Gulf of Guinea suppresses convection, so the result is an increase in the moisture flux onto the coast and precipitation increases north of the SSTAs.

A similar mechanism is prominent in the hydrodynamics of the region's interannual variability, in which warm years in the Gulf of Guinea are associated with enhanced rainfall on the Guinean coast (Vizy and Cook 2002). It is also consistent with the requirements of the region's vorticity balance. Cook (1997) showed that the maintenance of rainfall along the Guinean coast requires that low planetary vorticity from the south be transported into the region to balance the positive relative vorticity tendency associated with mid-

tropospheric condensational heating and low-level vorticity stretching. Here we find that the meridional advection of low relative vorticity air also contributes to this balance.

2.6.3. The hydrodynamic response to stronger Atlantic SSTAs: The 2K, 2.5K, 3K and 4K simulations

As seen in Fig. 6, Guinean coast rainfall rates increase with increased warming in the Atlantic Ocean, but Sahel rainfall rates reverse the trend and decrease when Atlantic warming reaches 2 K and higher.

Figure 12 explains why the response over the Sahel is nonlinear. Increased warming in the Atlantic leads to further reductions in the large-scale meridional geopotential height gradient over West Africa as geopotential heights in the Gulf of Guinea decrease. In the 2K simulation, shown in Figure 12a, the monsoon flow and the West African westerly jet continue to impinge on the Guinean coast supporting rainfall in that region. Farther north, the meridional geopotential height gradient is weaker, as seen in the difference fields shown in Fig. 12b, and the associated easterly wind anomalies over the Sahel become large enough to reverse the direction of the flow. In the 2K simulation, easterly flow develops in the Sahel east of 5°E. This easterly flow is associated with dry air advection and precipitation reductions.

With continued warming in the Atlantic – particularly in the Gulf of Guinea – the easterly full-field flow expands westward and strengthens as the meridional geopotential height gradients flatten. In the 3K simulation, shown in Figs. 12c, easterly flow stretches across the western Sahel due to very large easterly anomalies (Fig. 12d).

To understand the mechanisms of the nonlinear response, we distinguish between the non-convective and convective components of precipitation. Differences in the non-convective precipitation among all of the warming simulations and the control are small (not shown). The differences in total precipitation, displayed in Figures 5a-d, are similar to the differences in the convective precipitation. To connect differences in convective precipitation with the dynamical fields, we examine moist static energy (MSE) profiles. MSE is a linear combination of the thermal, latent and the geopotential energy defined as

$$\text{MSE} = c_p T + Lq + gz \quad (1)$$

where c_p is the specific heat of air at constant pressure, T is air temperature, L is the latent heat of vaporization, q is specific humidity, g is the acceleration due to gravity, and z is the geopotential height. A stable atmosphere will have increasing MSE with elevation. A high value of MSE at low levels destabilizes the atmosphere.

Figures 13 a and b display differences in the moist static energy profiles from the 1.5K–CTL and 2K–CTL simulations, respectively. The profiles are averaged from 26 June–26 July over the region 10°W–0°E; 13°N–16°N to emphasize the nonlinear signal in convective precipitation. Negative slopes of the anomalous MSE profiles (solid line), especially below 850 hPa, indicate that the low-level atmosphere is more unstable than the control in both simulations. The increased instability is associated with low-level moisture anomalies (Lq; dotted line). Atmospheric moisture increases from the surface to 550 hPa in 1.5K, but it decreases at all levels in the 2K simulation. Consistent with these differences, convective precipitation increases in the 1.5K simulation and decreases in the 2K simulation.

The thermal profiles (*cpT;* black dashed line) show that there is warming of the entire atmospheric column in the 1.5K and 2K simulations (Figs. 13 a and b). The profile is almost neutral in the 1.5K simulation. On the other hand, there is greater warming at 850 hPa than at the surface in the 2K simulation, and this stabilizes the vertical column. Differences in the geopotential energy (*gz;* faint-dashed line) are negligible in both. Factors associated with increases in precipitation over the Gulf of Guinea and the Guinean coasts in the 2K, 3K, and 4K simulations are similar to those in the 1.5K simulation, and there is no nonlinear behavior in this region. To confirm the robustness of the nonlinear response of Sahel rainfall to warming Atlantic SSTAs, a second set of seven simulations for each case was run with a different initialization date in March. The same nonlinear response of the Sahelian rainfall to the warming of the Atlantic was reproduced in the second set of simulations.

2.7. SUMMARY AND CONCLUSIONS

To contribute to an improvement in our physical understanding of how the West African monsoon will respond under global warming, we isolate one aspect of the problem, namely, the hydrodynamics of the response to a uniform warming of the Atlantic Ocean. Forcing from the Atlantic Ocean is chosen because of the known sensitivity of the monsoon system to Atlantic SSTAs. Idealized simulations with a regional climate model and uniform Atlantic warming ranging from 1 K to 4 K are conducted. The model has 90-km resolution and produces a state-of-the-art simulation of the present day climate of West Africa, including the precipitation and flow fields.

With 1 K and 1.5 K SSTAs prescribed in the Atlantic, rainfall rates increase by 30-50% over most of West Africa, including both the Guinean coast region (8°N – 10°N) and the Sahel (13°N – 16°N). With Atlantic warming of 2 K and higher, precipitation still increases between 8°N and 12°N, but Sahel rainfall decreases. These decreases are quite substantial, with approximately 60% reductions with Atlantic warming of 2.5 K and 85° with 4 K SSTAs. This nonlinear response in Sahel rainfall is the focus of the analysis of the model simulations.

Warming less than 2 K in the Atlantic Ocean is accompanied by decreases in low-level geopotential heights in the Gulf of Guinea and, as a consequence, decreases the large-scale meridional geopotential height gradients across West Africa. By a geostrophic argument, this leads to easterly wind anomalies in the central Sahel and the southerly monsoon flow onto the Guinean coast is not diverted to the east as strongly. The moisture from the Gulf is able to penetrate farther north over the western Sahel, and this leads to precipitation increases in that region. With greater Atlantic warming, the weakening of the continental-scale meridional geopotential height gradient continues, and the easterly anomalies strengthen. With 2 K warming – the threshold value in these simulations – the easterly anomalies reverse the westerly flow over the Sahel. The result is dry air advection into the Sahel and precipitation reductions. A moist static energy analysis shows that the entire atmospheric column warms in all warm SSTAs simulations. The destabilization at low-levels that supports convection in the 1K and 1.5K simulations is due to increases in the low-level moisture content of the atmosphere. The moisture content of the atmosphere

decreases, and the low-level atmosphere is stabilized, with Atlantic warming of 2K and higher.

In all of the simulations, the southerly monsoon flow onto the Guinean coast is maintained, and precipitation in that region increases. These increases become more closely confined to the coast as the Atlantic warms. The hydrodynamics in this region is dominated by moisture considerations. Warmer Gulf of Guinea SSTs are associated with enhanced evaporation, and the moisture content of the southerly monsoon flow increases. Precipitation anomalies do not develop over the SST anomalies because of the presence of large-scale subsidence over the Gulf of Guinea. Warming even up to 4 K does not break through this subsidence.

Climate change and variability in West Africa and the Sahel is complicated and regional. In this analysis, we focus only on Atlantic SST forcing to develop a deeper understanding of the region's hydrodynamic response. The application of these results to the global warming problem is limited by this focus. For example, we do not take into account Indian Ocean warming that is known to be a prominent forcing factor for decadal variability over the Sahel and we do not increase CO_2 levels in these idealized simulations. One could hypothesize that the physical processes that are at the heart of the response analyzed here would be interrupted if increasing greenhouse gas levels cause the Sahara to warm and the continental thermal low to strengthen as the Atlantic warms. However, confident prediction of twenty-first-century climate change in the region requires that we build a solid understanding of the physical processes of that change, and here we contribute to that goal in a process study that isolates the response to uniform Atlantic SSTAs.

2.8. ACKNOWLEDGEMENTS

Department of Energy (Award DE-FG02-08ER64610) is gratefully acknowledged. The Texas Advanced Computing Center (TACC) at the University of Texas at Austin provided the high-performance computing and database resources. The authors also acknowledge Dr. Edward K. Vizy, Dr. Christina M. Patricola, and Dr. Bing Pu for their helpful discussions and suggestions.

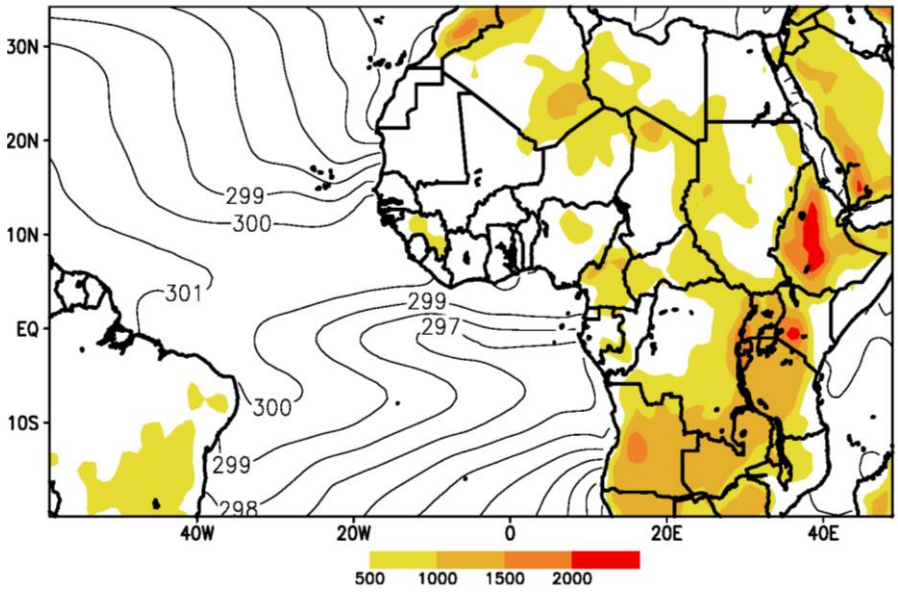

Figure 1. Model domain with topography (shaded, m) and average 26 June – 26 July sea surface temperatures (contoured, K) from the CTL simulation.

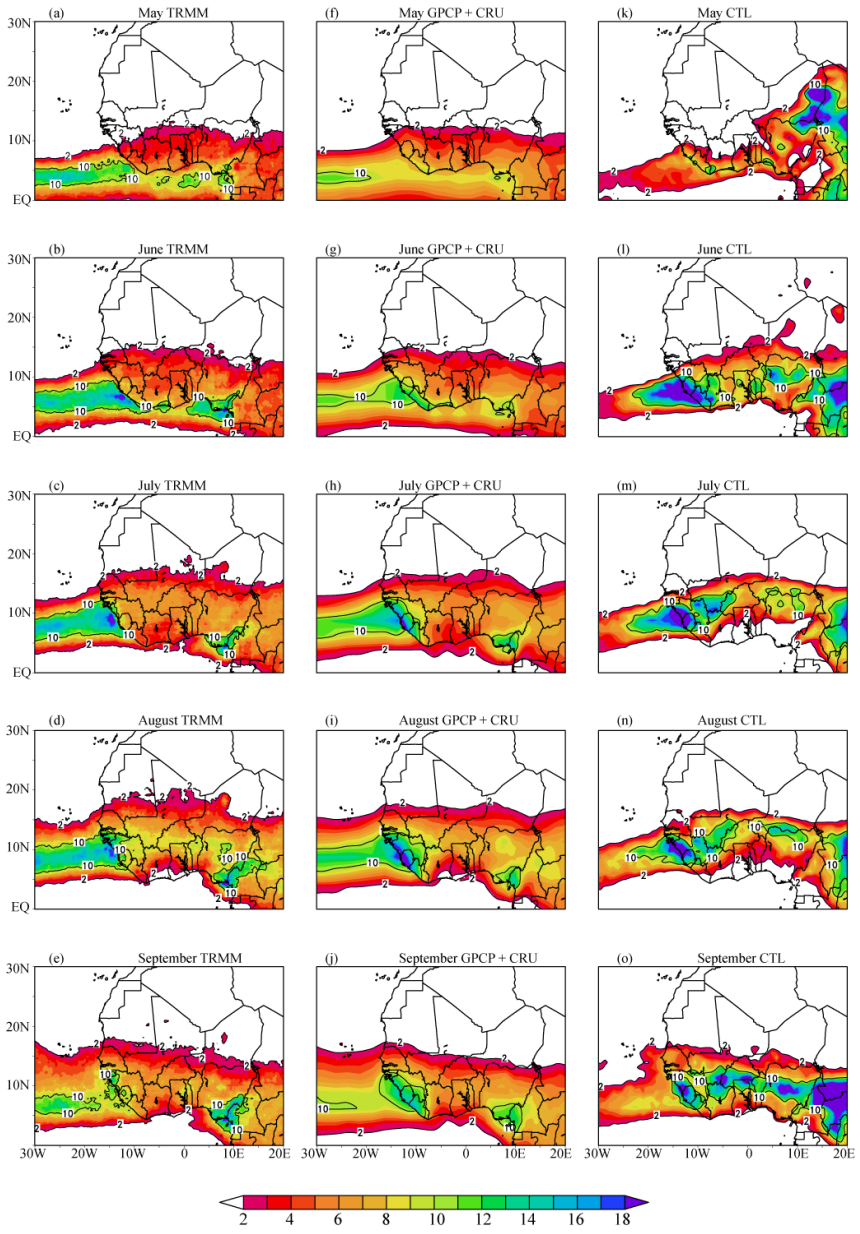

Figure 2. Monthly rainfall (mm/day) for the (left column) TRMM climatology, (center column) the GPCP climatology over the ocean and the CRU climatology over land, and (right column) the control simulation. Contours are drawn for 2 mm/day and 10 mm/day rainfall rates, and the shading interval is 1 mm/day.

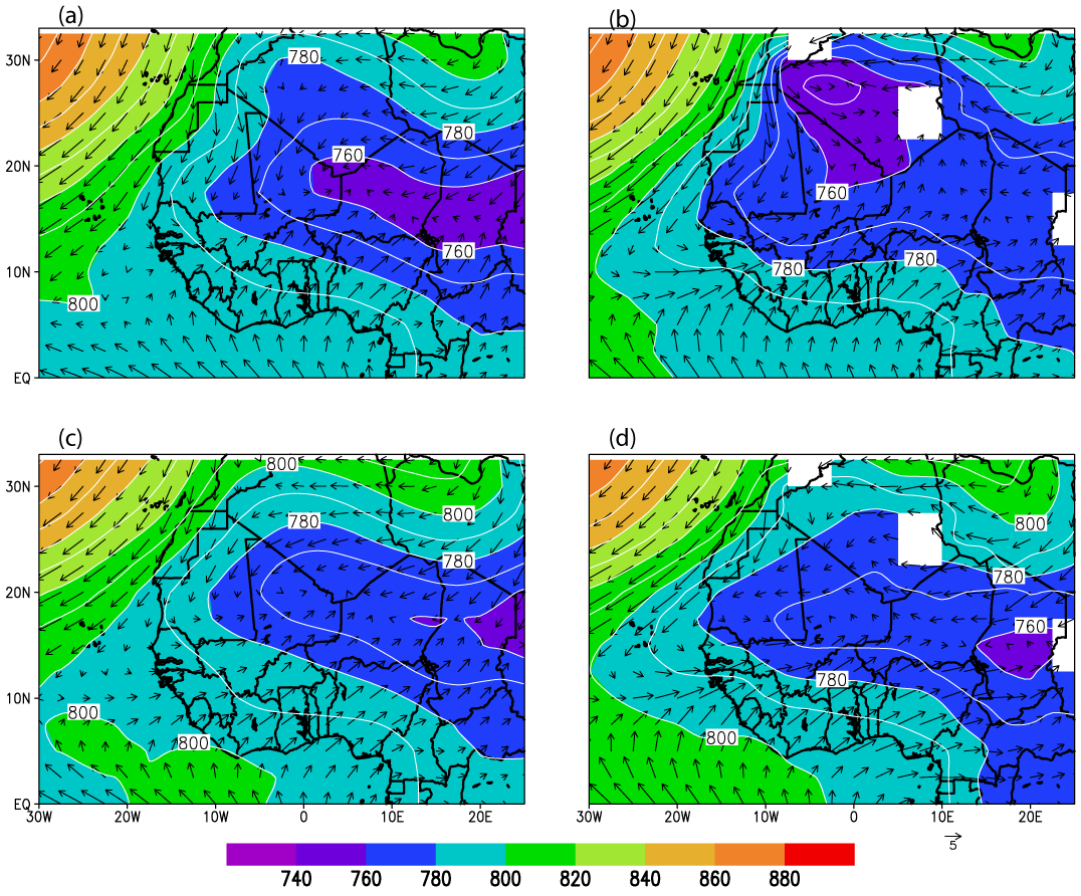

Figure 3. 925-hPa June geopotential heights (gpm) and winds (m/s) from the (a) ERA-Interim reanalysis climatology and (b) control simulation. Also, the 925-hPa geopotential heights (m) and winds (m/s) averaged for July-September from the (c) ERA-Interim climatology and (d) control simulation. Contour and shading interval is every 10 meters.

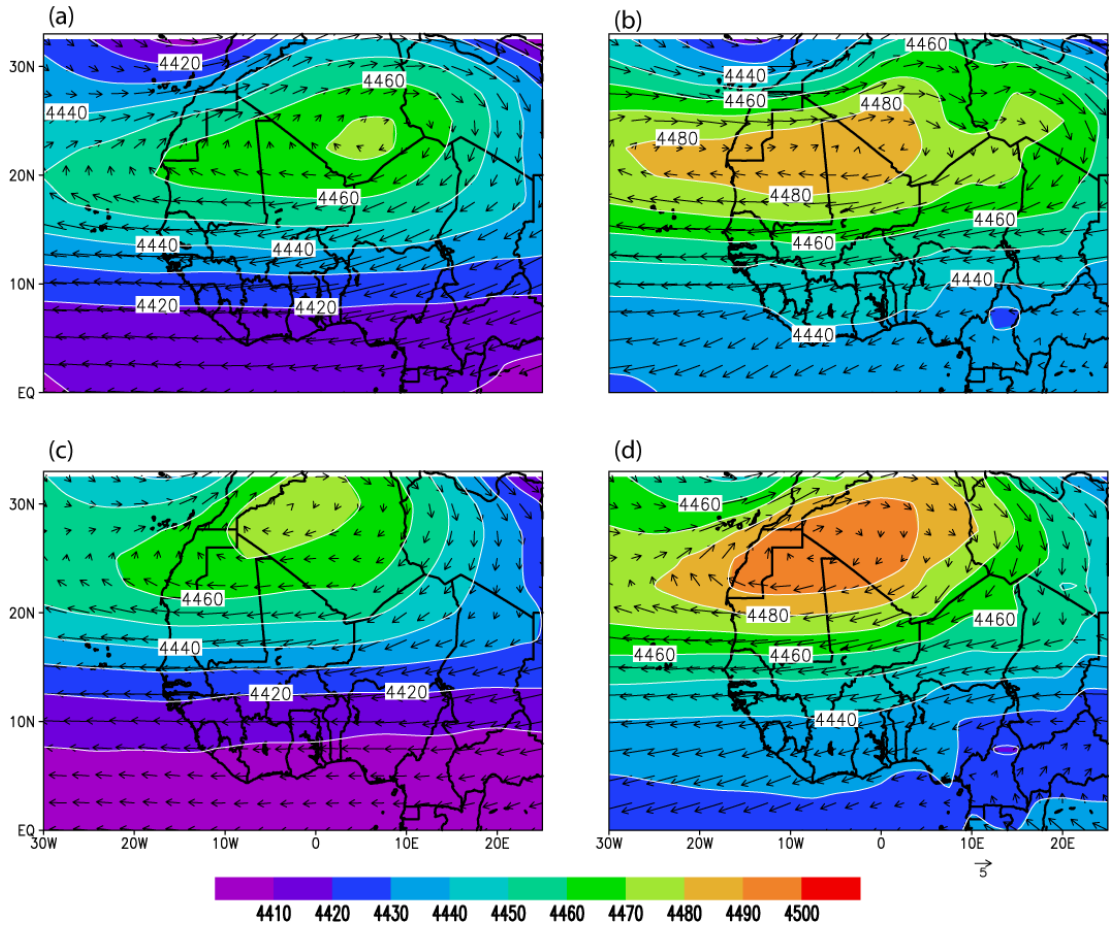

Figure 4. 600-hPa June geopotential heights (gpm) and winds (m/s) for the (a) ERA-Interim climatology and (b) control simulation. Also, 600-hPa geopotential heights (gpm) and winds (m/s) averaged for July-September from the (c) ERA-Interim climatology and (d) control simulation. Contour and shading intervals are 10 gpm.

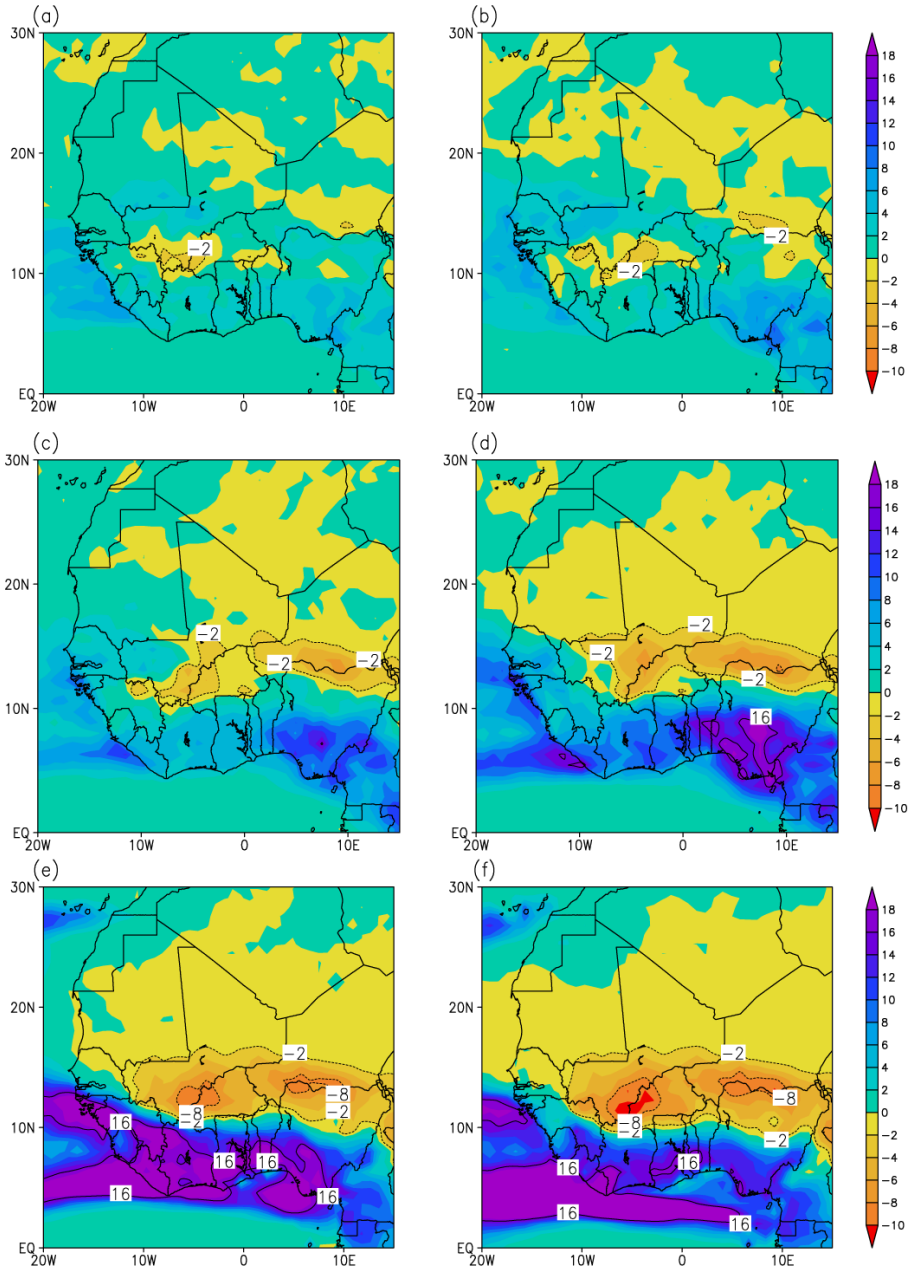

Figure 5. Precipitation differences from the control simulation averaged over July–September for simulations with (a) 1K, (b) 1.5K, (c) 2K, (d) 2.5K, (e) 3K and (f) 4K warming of the Atlantic Ocean. Contours are drawn for precipitation differences of -8, -2, +2 and +8 mm/day.

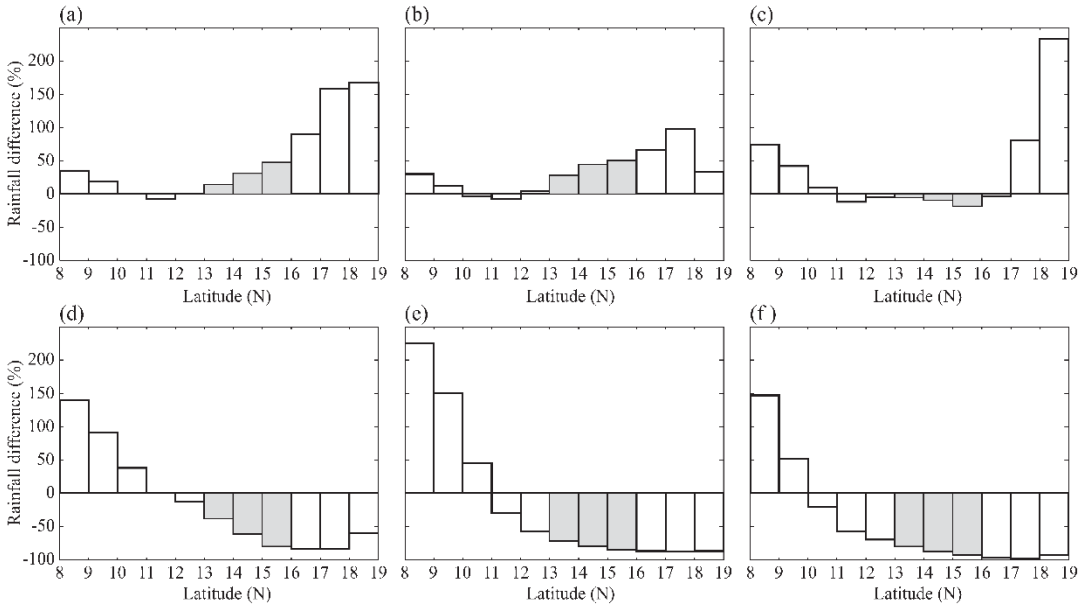

Figure 6. Percentage differences in the average July–September precipitation (mm/day) for the (a) 1K-CTL, (b) 1.5K-CTL, (c) 2K-CTL, (d) 2.5K-CTL, (e) 3K-CTL and (f) 4K-CTL simulations, respectively. The averaging box in each case has a width of 1° of latitude and extends from 12°W to 6°E. The Sahelian region from 13°N–16°N are shaded.

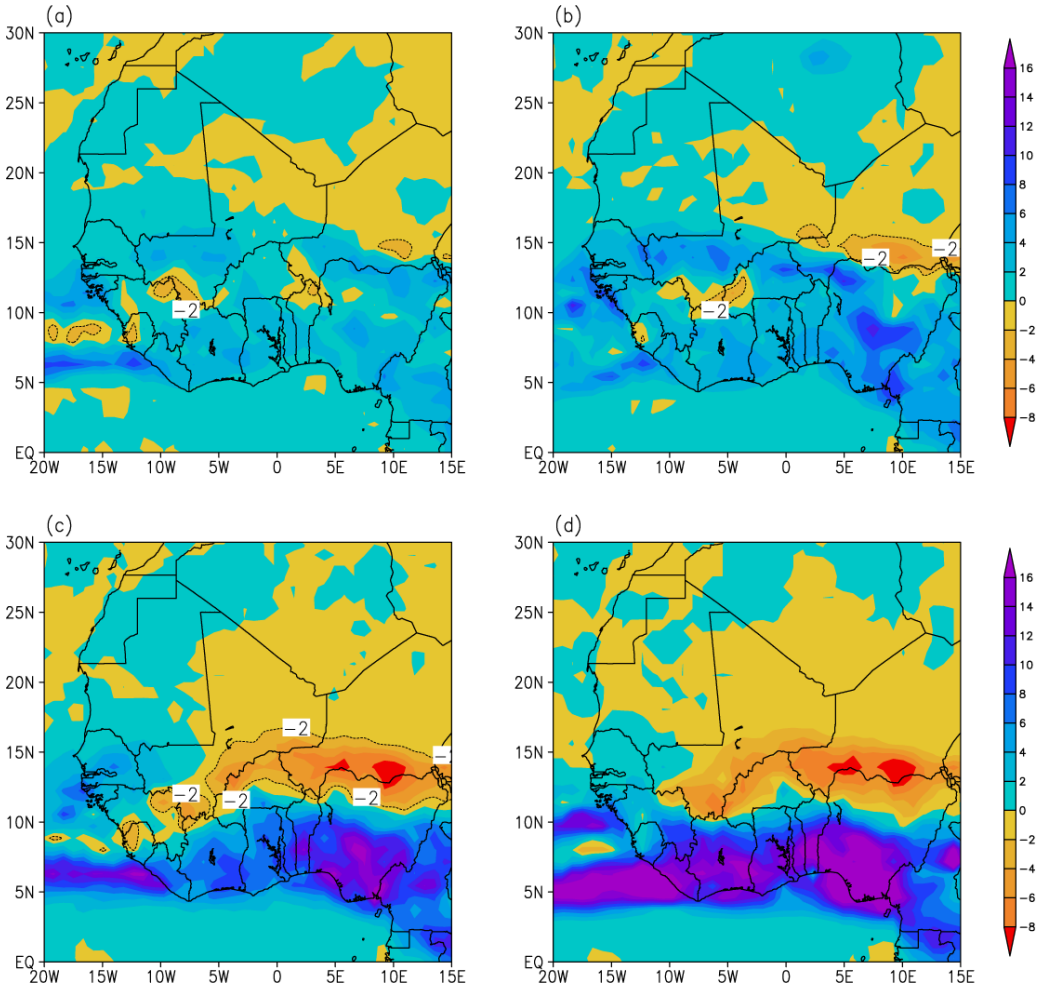

Figure 7. Average 26 June–26 July precipitation (mm/day) anomalies for the (a) 1K-CTL, (b) 1.5K-CTL, (c) 2K-CTL, and (d) 2.5K-CTL simulations, respectively. Contouring indicates precipitation anomalies of –2 mm/day.

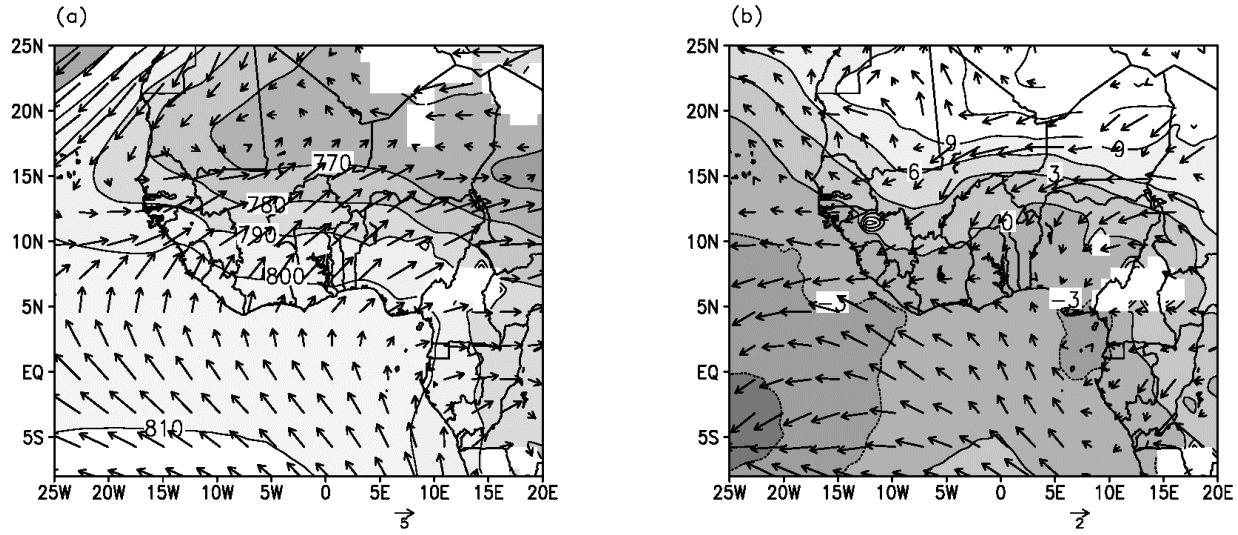

Figure 8. (a) 925-hPa geopotential heights (10 gpm contour interval) and winds (m/s, vector scale at bottom) from the CTL simulation. (b) Differences in 925-hPa normalized geopotential heights (3 gpm contour interval) and winds (m/s, vector scale at bottom) for 1.5K-CTL. All values are averaged over 26 June–26 July.

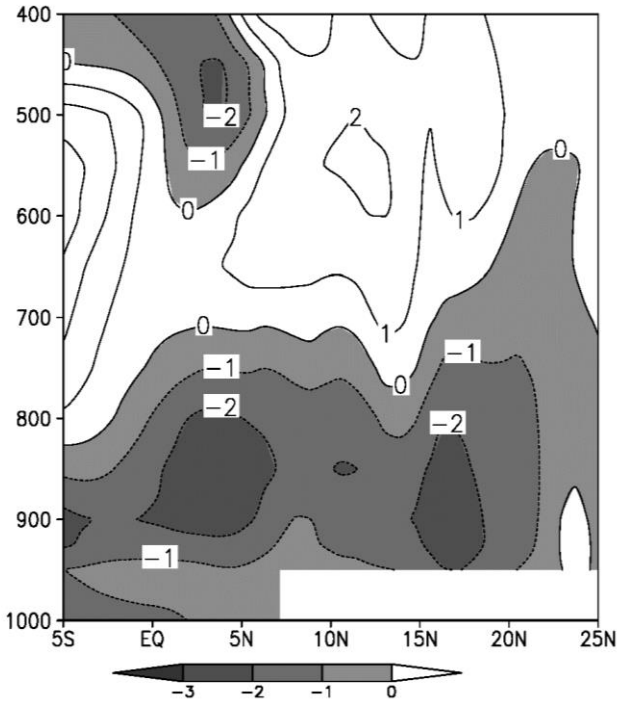

Figure 9. Latitude-height cross section of the difference in zonal wind speed (1.5K-CTL) for the 26 June–26 July period averaged from 12°W to 6°E. The contour interval is 1 m/s and negative values are shaded.

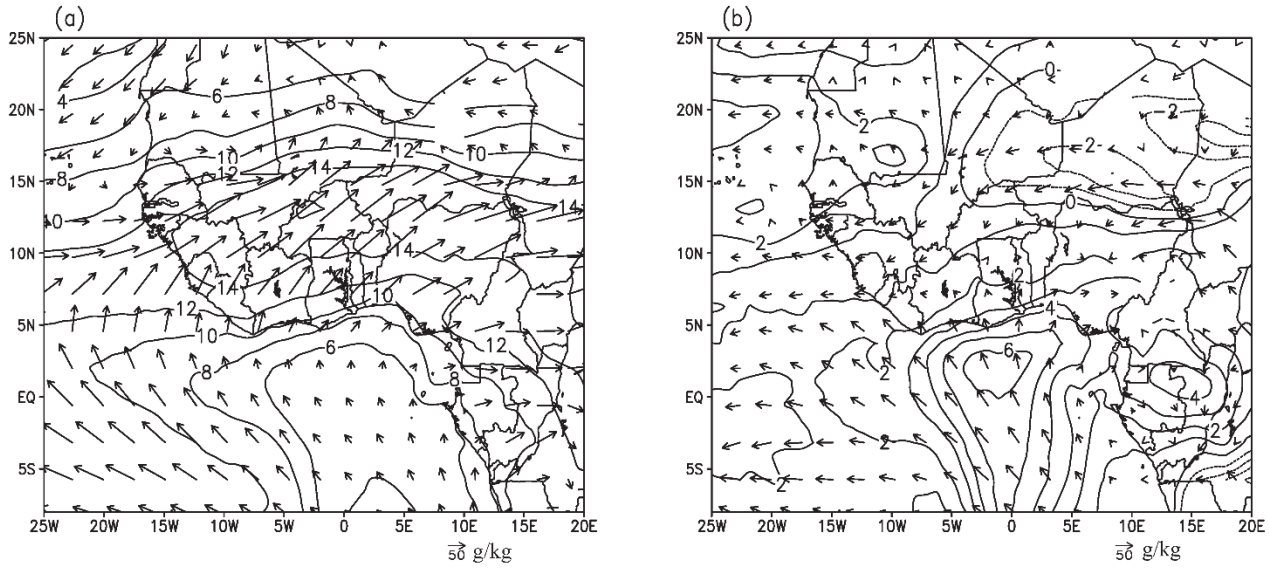

Figure 10. (a) 925-hPa horizontal moisture transport (vectors; 10^{-3} g-m/kg-s) and mixing ratios from the CTL simulation. (b) Differences in the 925-hPa horizontal moisture transport (vectors; 10^{-3} g-m/kg-s) and mixing ratios (1 g/kg contour interval) for 1.5K-CTL. All values are averaged over 26 June–26 July. Contour interval is 2 g/kg in (a) and 1 g/kg in (b).

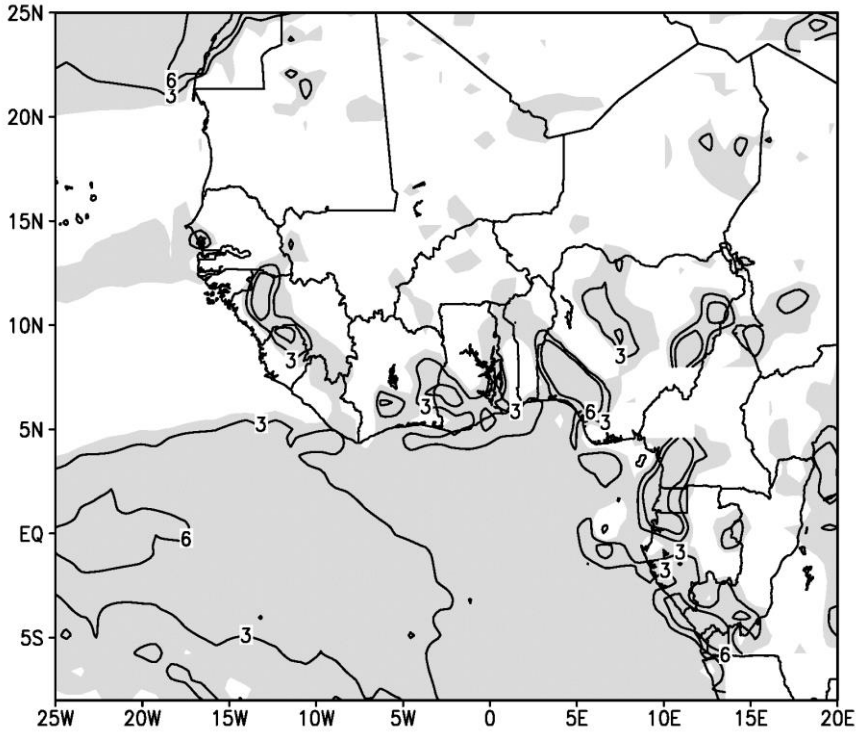

Figure 11. Average 26 June–26 July 925-hPa vertical p-velocity (10^{-2} Pa/s) from the CTL simulation. Contours are drawn for vertical p-velocity values of 3 and 6 × 10^{-2} Pa/s, and positive values indicating subsidence are shaded.

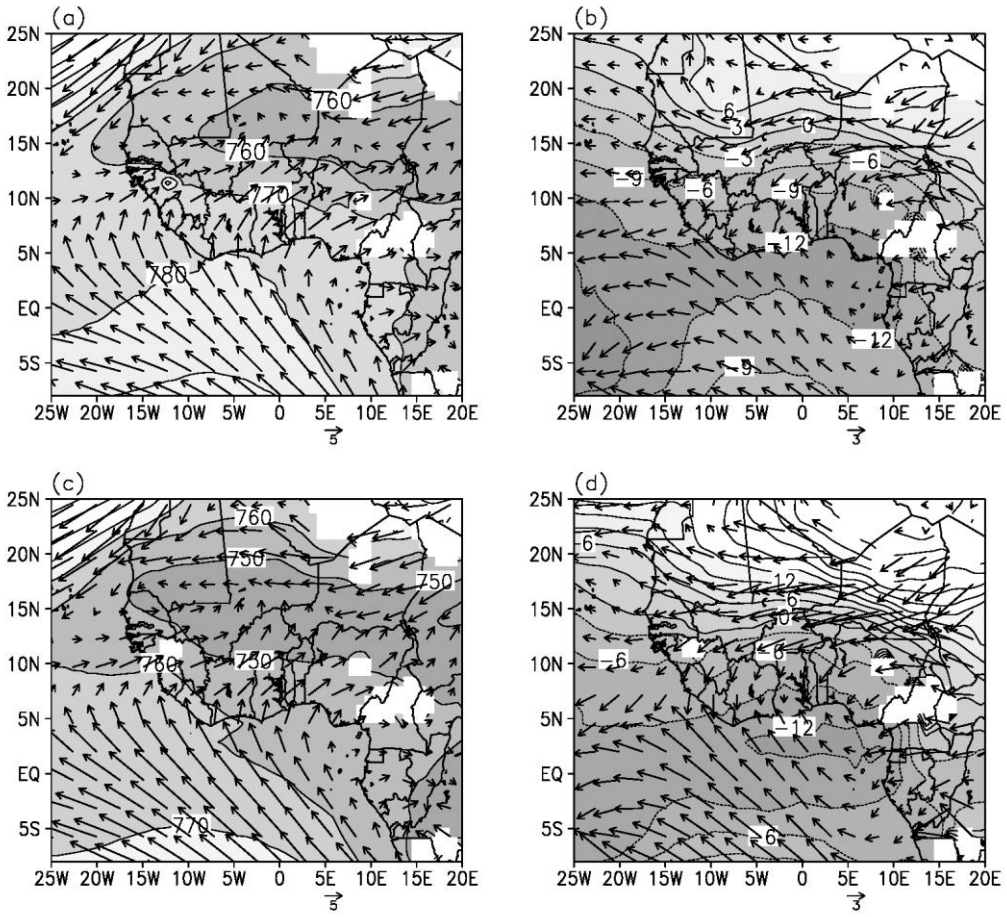

Figure 12. (a) 925-hPa geopotential heights (10 gpm contour interval) and winds (m/s, vector scale at bottom) from the 2K simulation and (b) differences in the 925-hPa normalized geopotential heights and winds for 2K-CTL. Normalization factor is 13.4 gpm. (c) 925-hPa geopotential heights (10 gpm contour interval) and winds (m/s, vector scale at bottom) from the 3K simulation and (d) differences in the 925-hPa normalized geopotential heights and winds for 3K-CTL. Normalization factor is 33.5 gpm. All values are averaged over 26 June–26 July.

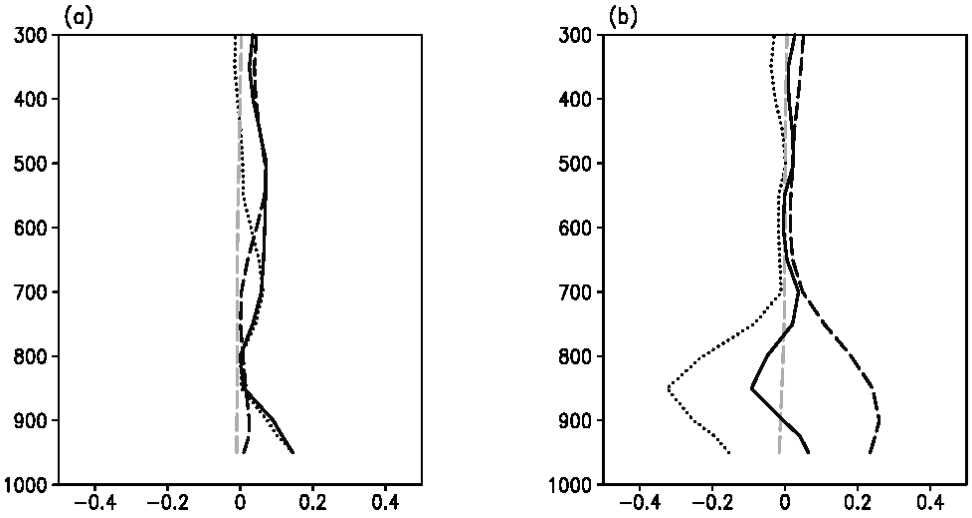

Figure 13. Average 26 June–26 July moist static energy ($\times 10^4$ j/kg) profiles over 10°W–0°E; 13°N–16°N in the (a) 1.5K-CTL and (b) 2K-CTL simulations, respectively. The solid, black-dashed, grey-dashed, and the dotted lines denote *MSE*, c_pT, *gZ*, and *Lq*, respectively.

Chapter 3: Understanding projections of increased precipitation intensity in the U.S. [2]

3.1 ABSTRACT

Climate models predict that there will be more intense precipitation events in the future as the climate warms under greenhouse gas forcing. A theoretical understanding of this change is founded in the Clausius–Clapeyron equation, which associates a 1 K increase in surface temperature with a 7% increase in the saturation mixing ratio, along with model simulations which predict that relative humidity remains fairly constant as the climate warms. Using regional model simulations, the Clausius-Clapeyron predicted theoretical precipitation is compared with the modeled precipitation on seasonal and regional scales over the U.S. for the mid-21st century. We investigate the physics of the departure of the theory from the model.

Most precipitation differences between the future and present day simulations in the analysis region, east of the Rockies, are associated with the convective precipitation. In spring and fall, the temperature scaled convective precipitation increases up to 30%/K, while reductions, up to -15%/K, occur in the summer. Increases in the convective component follow the theoretical predictions from the Clausius-Clapeyron scaling relation

[2] Model output analyzed in this chapter is obtained from Patricola and Cook (2013). Idea of this project was conceived by Kerry H. Cook, figures were prepared by Naresh Neupane, and this is jointly written by Kerry H. Cook and Naresh Neupane.

in the spring and fall, while the theoretical predictions fail completely in the summer. An analysis of the moist static energy balance reveals that the primary reason for the differences between the simulated and theoretical predictions are associated with soil moisture distributions. Associated with the increases of soil moisture, as in the spring and fall, increases in convective rainfall intensities agree with the theoretical predictions. Associated with the reductions in soil moisture, warming leads to enhanced dry convection but there is no precipitation increase, and the theoretical prediction based on the Clausius–Clapeyron equation fails.

3.2. INTRODUCTION

Climate models often project increases of precipitation in association with increases in atmospheric greenhouse gases. Physical understanding of these increases is based upon two factors. The first is the Clausius–Clapeyron relation, which indicates that a 1 K increase in surface temperature is accompanied by approximately a 7% increase in the saturation mixing ratio. The second factor is the idea that the relative humidity remains approximately constant as climate warms (Manabe and Wetherald 1975). Taken together, the tropospheric water vapor content increases, which is associated with increases of precipitation in a warmer climate.

The purpose of this paper is to improve our physical understanding of the projected increases in mean rainfall intensity on regional and seasonal scales over the U.S. in the mid-21st century compared with the 20th century.

Given simulated changes in surface temperature due to increasing atmospheric carbon dioxide concentrations, we use the Clausius–Clapeyron equation and the assumption of constant relative humidity to estimate theoretical changes in moisture fields, including precipitation. These estimates are compared with regional model simulations of the mid-21st century climate to understand the degree to which the theory is valid and evaluate the reasons for departures from the estimates. The analysis focuses on understanding the changes in convective precipitation. This is because convective precipitation is more closely associated with surface temperature than non-convective precipitation (Mitchell and Ingram 1992; Gordon et al. 1992; Whetton et al. 1993), and it provides an opportunity for evaluating the predictive ability of the Clausius-Clapeyron relation on regional and seasonal scales.

Section 2 provides background, and section 3 describes the model and method of analysis. A control simulation is compared with reanalysis and observations in section 4. Results are reported and discussed in section 5, and conclusions are drawn in section 6.

3.3. BACKGROUND

Models simulate increases in global mean precipitation associated with the increases in greenhouse gases (Meehl et al. 2000; Cubasch et al. 2001; Wilby and Wigley 2002; Emori et al. 2005). These increases have been related to increased atmospheric convection (e.g., Noda and Tokioka 1989; Mitchell et al. 1995; Royer 1998), and they exhibit strong regional variations (Kitoh et al. 2005).

These simulated increases in precipitation include the U.S. (Meehl et al. 2007; Dominguez et al 2012; Field et al. 2012). Over the U.S. to the east of the Rockies, which is the focus of this paper, studies have shown significant changes in mean precipitation in the future. For example, a regional climate model (RegCM3), supplied with future boundary conditions from the Community Climate System Model version 3, shows increases of about 20% in mean precipitation intensity in the spring and fall, while reductions of larger than -30% are shown for the summer of mid-21st century (Singh et al. 2013). Also, the Inter-governmental Panel on Climate Change Fifth Assessment Report (IPCC/AR5) along with regional model projections indicate that the mean precipitation increases in the spring and fall, while reduces in the summer in the future (IPCC 2013; Sillmann et al. 2013; Gao et al. 2014). These changes in precipitation under global warming are often studied in association with the changes in surface temperature.

Observations indicate that there have been increases in precipitation intensity along with the surface temperature in the past three decades (Easterling et al. 2000; Groisman et al. 2005) and, in some cases, these increases are close to the 7% per 1 K warming of the surface, as predicted by the Clausius-Clapeyron relation. Wentz et al. (2007) showed that satellite observed precipitation increased in the global mean by 6%/K from 1987-2006. Other observational studies result in lower estimates for the rate of change of precipitation. For example, Adler et al. (2008) analyzed precipitation from the Global Precipitation Climatology Project and found a 2.3% rise in precipitation for every 1 K rise in surface temperature from 1979-2006, and Lin et al. (2006) showed that precipitation in Tropical Rainfall Measuring Mission satellite observations increased by 2%/K in the tropics.

Similar to the observation, GCMs simulate increases of precipitation and specific humidity in the future under global warming (Trenberth et al. 2003; O'Gorman and Schneider 2009; Zahn and Allan 2013). Evaluation of coupled GCM simulations of the mid-21st c. conducted for the Third and Fourth Assessment Reports of IPCC (2001, 2007) showed that most models predict global precipitation intensification of 1%–4%/K (Cubasch et al. 2001; Vecchi and Soden 2007; Stephens and Ellis 2008; Durack et al. 2012). In addition, models participating in IPCC AR5 also shows global average precipitation intensification in the range of 1.5–2.5%/K in the mid-21st century (Kharin et al. 2013).

When exploring the relationship between surface temperature and precipitation, it is important to distinguish between land and ocean. Generally, increases of precipitation take place over the regions where increases of temperature occur over the ocean (Xie et al. 2010), but not over land. For example, projections from four regional climate models from the North American Regional Climate Change Assessment Program show that land temperature increases are associated with precipitation decreases in the future (Rangwala et al. 2012), and precipitation changes under global warming also exhibit strong seasonal and regional dependence, as discussed above (e.g., Gao et al. 2014; Singh et al. 2013).

O'Gorman and Muller (2010) analyze output from the World Climate Research Programme's Coupled Model Inter-comparison Project phase 3 (CMIP3) coupled GCMs to understand future changes in the low-level specific humidity. Low-level specific humidity was found to increase up to 5.7%/K globally. The increases closely followed the Clausius–Clapeyron scaling over the oceans, with relative humidity remaining nearly constant, but the differences over land were much larger, for example in the central U.S.,

reductions of up to -2%/K occur. Similarly, studies have shown that relative humidity does not exactly remain constant under global warming (Xie et al. 2010; Richter and Xie 2008). This is also consistent with the recent observed trend of increase, up to 2%/decade, in relative humidity over the U.S. (Dai 2006).

In summary, past studies suggest that there are differences between modeled precipitation and moisture fields and their theoretical predictions on global scale. An improved understanding of how precipitation changes under greenhouse gas forcing, including its relationship with atmospheric moisture and surface temperature changes on both global and regional scales, is needed. To contribute to the development of this understanding, this paper focusses on precipitation responses on regional space scales.

3.4. MODEL AND METHODOLOGY

Regional climate model (RCM) output from simulations described in detail by Patricola and Cook (2013a, 2013b) is used. Here we provide a brief description of the model, which is the Weather Research and Forecasting (WRF) model version 3.1, and the simulation design.

The RCM is run with 30 vertical levels and the top of the atmosphere set to 30 hPa. Nested domains are used as shown in Fig. 14, with two-way interaction across the interior boundaries. The parent domain (125.1°W–14.9°W and 10.8°N–65.4°N) has grid point spacing of 90 km and the time step used is 6 minutes. The inner domain (103.0°W–84.3°W and 20.2°N–50.4°N) has grid point spacing of 30 km and the time step is 2 minutes. Here,

only model output on the parent domain is analyzed to provide coverage over a larger area. The analysis region is the east of the Rockies, as will be justified in section 4.

Physical parameterizations were tested by Patricola and Cook (2013a) and chosen to produce a state-of-the-art simulation. These include the Yonsei University (YSU) planetary boundary layer scheme (Hong et al. 2006), the Monin-Obukhov surface scheme (Monin and Obukhov 1954), the new Kain-Fritsch cumulus scheme (Kain and Fritsch 1990; 1993), the Lin et al. microphysics scheme (Lin et al. 1983; Rutledge and Hobbs 1984), the CAM longwave and shortwave radiation schemes (Collins et al. 2004), and the NOAH land surface model (Chen and Dudhia 2001), which solves the heat and moisture equations at four levels in the soil column and takes into account canopy effects.

The control climate, called 20C, consists of 21 years of annual integrations from 1980 to 2000. The first year of the integration (1980) is devoted to model spin-up. The simulation for 1981 is initialized on December 1, 1980, and run through December 31, 1981, and the first month is disregarded for spin-up. All 20 annual integrations are run in this way. The atmospheric variables are reinitialized from the reanalysis while surface temperature, snow cover and soil moisture are supplied from the previous model integration. Model output is saved every 3 hours. See Patricola and Cook (2013a) for further discussion.

Atmospheric initial surface boundary conditions for soil moisture and temperature are initialized from the North American Regional Reanalysis (NARR; Mesinger et al. 2006) from the 1980-2000 monthly climatology of January. Sea surface temperature is from the European Centre for Medium–Range Weather Forecasts (ECMWF 2002)

reanalysis. Lateral boundary conditions are from the National Center for Environmental Prediction/Department of Energy Atmospheric Model Inter-comparison Project II (NCEP/DOE AMIP-II) Reanalysis (Kanamitsu et al. 2002). The sea ice fraction comes from the NCEP/NCAR reanalysis (Kalnay et al. 1996). Monthly mean values were linearly interpolated in time to generate 6-hourly boundary conditions.

The future climate simulation, called 21C, consists of 21 years of annual integrations from 2040 to 2060 generated by the same method as 20C. Atmospheric concentrations of CO_2, N_2O, CH_4, CFC-11, and CFC-12 were prescribed according to the SRESA2 emission scenario (IPCC 2000).

Boundary conditions for 21C were prepared by adding monthly climatological anomalies from the average of six coupled atmosphere-ocean CMIP3 GCMs. See Patricola and Cook (2013a, 2013b) for additional information and evaluation of this anomaly forcing methodology.

3.5. MODEL EVALUATION

In order to build confidence in the results, the model's ability to represent the observed U.S. climate is examined. Comparisons with the state-of-the-art GCMs are also included to evaluate the quality of the RCM simulation. With a focus on understanding warm season precipitation projections for the mid-21st century, Patricola and Cook (2013a, 2013b) evaluate the modeled present day precipitation and compare those with the NARR on monthly scales, and the model represents the observed monthly precipitation features. Since this study focuses on seasonal scales, the model's ability to represent observed

precipitation on seasonal scales is assessed. Surface temperature and soil moisture distributions in the simulation are also evaluated.

Figure 15a displays the observed precipitation (mm/day) climatology averaged from 1981-2000 for the March-April-May (MAM) mean from the Climate Research Unit (CRU, Mitchell and Jones 2005) CRUTS3.0 dataset. Simulated values from the average of nine atmosphere–ocean GCMs (AOGCMs) for MAM from the CMIP5 historical runs are plotted in Fig. 15b, and the MAM RCM values are shown in Fig. 15c.

There is a rainfall maximum of about 5 mm/day along the borders of Mississippi, Louisiana, and Arkansas, and a strong rainfall gradient that decreases toward the northwest in the observations. For example, rainfall rates in New Mexico are about 1 mm/day and they are up to 5 mm/day in Louisiana (Fig. 15a). The AOGCM ensemble mean places the rainfall maximum further north over Kentucky and Tennessee (Fig. 15b) while the RCM places it over Kentucky and Pennsylvania (Fig. 15c). Magnitudes of the AOGCM and RCM simulated rainfall are comparable to those of the observations.

Figures 15d-f show precipitation distributions for the June-July-August (JJA) mean. Observed rainfall rates along the southern coast are about 8 mm/day, and there is a strong zonal precipitation gradient (Fig. 15d). The AOGCMs fail to represent this zonal gradient (Fig. 15e), but it is present in the RCM simulation, and the RCM also represents the locations of maximum rainfall along the coast (Fig. 15f).

September-October-November (SON; Figs. 15g-i) rainfall rates along the southeast coast are up to 3 mm/day smaller than in JJA, and a rainfall maximum of about 5 mm/day occurs over the Coastal Plains, for example, in Louisiana and Arkansas, in the observations

(Fig. 15g). The zonal rainfall gradient is maintained through the boreal fall. The AOGCMs do not produce maxima over Louisiana and fail to represent the zonal gradient in rainfall (Fig. 15h). The RCM represents the rainfall along the southern coast but it places the rainfall maximum of 4 mm/day over Kentucky and Tennessee (Fig. 15i).

Observed December-January-February (DJF; Figs. 15j-l) rainfall rates over the Coastal Plains are up to 3 mm/day greater than in SON, and the zonal rainfall gradient is stronger in DJF than in SON (Fig. 15j). The RCM captures the rainfall maximum over the Coastal Plains, for example, rainfall rates in Louisiana are about 4 mm/day, comparable to those in the observations, and it also captures the observed zonal rainfall gradient, and similar to SON, the AOGCMs fail to represent the rainfall maximum over Louisiana and the zonal gradient in rainfall (Figs. 15l, and k).

There are some notable differences between the 20C RCM simulation and the observations. Rainfall rates in the RCM are generally about 3 mm/day greater than in the observations in the Northeast. Precipitation maxima are stronger in the RCM than in the observations over Idaho, Utah, Wyoming, and Colorado. East of the Rockies, differences are small, in Illinois, for example, rainfall rates are up to 1 mm/day smaller in the RCM than in the observations.

Overall, the RCM captures the seasonal evolution and distribution of precipitation. Magnitudes of simulated rainfall rates in the region to the east of the Rockies are also comparable to those in the observations. The RCM simulated precipitation is more realistic than in the AOGCMs. This is not surprising because the RCM is constrained by observed SSTs, unlike the AOGCMs, and its higher resolution represents topography more

accurately. Recall also that physical parameterizations were selected to optimize the simulation of the U.S. climate. Compared with the observations, the RCM simulated precipitation for the warm season was found to match better than the NARCCAP simulations (Patricola and Cook 2013a).

Figures 16a and b display the surface temperature (K) climatology averaged from 1981-2000 for MAM from the NARR and the RCM simulation, respectively. The southern Coastal Plains are warmer than the northern U.S. by about 17 K, with maximum temperatures of 297 K in Texas and Florida. The temperature gradient is about is about 0.8 K/ degree latitude in the NARR (Fig. 16a). The RCM simulation accurately places a temperature maximum of 297 K over the Coastal Plains, and it also captures the meridional temperature gradient (Fig. 16b).

Figures 16c and d display surface temperatures for the JJA mean from the NARR and the RCM simulation, respectively. Observed summer surface temperatures are up to 10 K warmer than spring temperatures. Similar to the MAM temperature distribution, the warmest temperatures are located over the Coastal Plains, and the meridional temperature gradient in JJA is weaker than in MAM, with temperature decreases of about 0.33 K/ degree latitude from Louisiana to Minnesota (Fig. 16c). The RCM captures the location of maximum temperature of 305 K in Texas, for example, and the meridional temperature gradient in boreal summer is realistic (Fig. 16d).

Figures 16e and f display observed and modeled surface temperatures for SON, respectively. Temperatures are generally up to 10 K cooler than in JJA in the NARR. The warmest temperatures of 297 K are located over the Coastal Plains, and temperature

decreases up to 0.83 K/ degree latitude from Louisiana to Minnesota (Fig. 16e). The RCM simulation captures the locations of the temperature maxima, for example, 297 K in Texas and Florida, and the model also represents the meridional temperature gradient fairly accurately, with temperature decreases of about 0.7 K/ degree latitude from Louisiana to Minnesota (Fig. 16f).

Figures 16g and h display observed and modeled surface temperatures for DJF, respectively. Temperatures are up to 10 K cooler and the meridional temperature gradient is stronger than in SON in the NARR (Fig. 16g). The RCM simulation captures the meridional temperature gradient, and the magnitudes of the simulated temperatures are also similar to those of the NARR (Fig. 16h).

Climatological soil moisture fractions for MAM are shown in Figures 17a and b, defined as volumetric soil moisture fraction (m^3-H_2O/m^3-soil, Mesinger et al. 2006) in the top 10 cm. The wettest soil is located in the central and the northeastern U.S. in the NARR, with values of 36×10^{-2} m^3-H_2O/m^3-soil in the central U.S. (Fig. 17a). There is a gradient in soil moisture, with soil moisture values decreasing from the east to the west, and the smallest values of 15×10^{-2} m^3-H_2O/m^3-soil are found in western Texas, Oklahoma, Kansas, Florida, and eastern Georgia. The RCM simulation captures the gradient and the locations of maximum and minimum soil moisture, but soil moisture values in the RCM are up to 5×10^{-2} m^3-H_2O/m^3-soil smaller than in the NARR (Fig. 17b).

Figures 17c and d show soil moisture distributions for the JJA mean. There is a gradient in soil moisture decreasing from the east to the west in the NARR (Fig. 17c). The RCM simulation captures this gradient and the location of maximum soil moisture (Fig.

17d). In general, the RCM is drier than the NARR. For example, in Texas, Colorado, Nebraska, and Oklahoma, soil in the model is up to 6×10^{-2} m^3-H_2O/m^3-soil drier than in the NARR reanalysis. Similar to the MAM mean, modeled soil moisture is larger in the eastern than in the western regions of the country, and this gradient is consistent with the precipitation distributions (Figs. 15c, 15f, 16b, and 16d).

Figures 17e and f show soil moisture for the SON mean. Soil moisture distributions are similar to those in JJA, and there is a westward decreasing gradient of soil moisture in the NARR (Fig. 17e). The RCM captures the locations of greatest soil moisture, for example, 33×10^{-2} m^3-H_2O/m^3-soil in Pennsylvania, and it also represents the westward decreasing gradient (Fig. 17f). Similar to MAM and JJA, the zonal gradient in soil moisture in the RCM is associated with the rainfall distribution pattern that is decreasing westward in SON (Figs. 15i and 17f).

DJF mean soil moisture distributions are displayed in Figs. 17g and 17h. Maximum soil moisture values are located in the Northeast and the northern regions of the central U.S., and minima are located in southwestern Texas and the Florida panhandle in the NARR (Fig. 17g). The RCM represents the locations of maximum and minimum soil moisture although soil in most places in the RCM is up to 6×10^{-2} m^3-H_2O/m^3-soil drier than in the NARR (Fig. 17h).

In summary, the 20C RCM simulations represent seasonal precipitation and its evolution in the region to the east of the Rockies. For this reason, the analysis domain of this study is east of the Rockies. In this region, the model also represents the surface temperature and soil moisture that is suitable for this regional scale study.

3.6. RESULTS

Figure 18a displays differences in the 21C and 20C regional model simulations for annual mean precipitation in the analysis region. Over much of the northern Midwest, precipitation is about 0.2 mm/day (9%) lower in 21C than in the 20C simulation, while over the central Midwest, Louisiana, and along the east coast it is approximately 0.2 mm/day (15%) greater. Reductions, up to 0.25 mm/day (15%), occur over Florida, southern Georgia and Alabama, and east Texas.

Figure 18b shows differences in the convective component of the total precipitation. Convective precipitation in the 21C simulation is larger than in the 20C simulation in most regions. Reductions are concentrated in Florida, where the total precipitation also decreases (Fig. 18a). Increases in convective precipitation of about 0.3 mm/day over east Texas, Louisiana, Mississippi, northern Georgia and the Carolinas are similar to the increases in total rainfall (Fig. 18a). In contrast to the total precipitation differences, convective precipitation is greater in the future simulation by up to 0.1 mm/day over the northern Midwest.

Figure 18c displays differences in the 21C and 20C simulations for annual mean non-convective precipitation. Reductions of up to 0.2 mm/day occur across the northern Midwest and the Gulf coast. Regions of increased non-convective precipitation are located between 30°N and 40°N and over the far northeast.

Figure 18d shows the contribution of snow and graupel to the total precipitation differences. Differences are generally small, but reductions of about 0.1 mm/day occur over the Great lakes and the northeast.

In summary, the total annual mean precipitation differences in the 21C and 20C simulations (Fig. 18a) south of about 42°N in the analysis region and along the east coast are due in large part to convective precipitation differences (Fig. 18b). North of about 42°N in the continental interior, decreases in non-convective precipitation, snow, and graupel (Figs. 18c and d) dominate over the increases in convective rainfall (Fig. 18b). Understanding that the changes in convective precipitation alone do not completely explain the changes in total precipitation, here we focus on convective precipitation changes only, as justified in section 1.

Seasonal convective precipitation and surface temperature differences are shown in Figure 19 for the March-April-May (Figs. 19a and b), June-July-August (Figs. 19c and d), and September-October-November (Figs. 19e and f) means. (We do not consider the December-January-February mean because differences in precipitation are small in the winter.) Similar to the annual mean, convective precipitation differences in the spring are generally greater in the 21C simulation than in the 20C simulation (Fig. 19a). Largest differences, up to 0.5 mm/day (20%), occur in the region to the east of the Rockies in the central Midwest, the central Gulf coast, the mid-Atlantic east coast, and the southern tip of Florida. The distribution of springtime surface warming (Fig. 19b) does not match the distribution of convective rainfall in an obvious way. The smallest increases (~ 1 K) are located over the Midwest, where the greatest increases of convective precipitation occur.

In contrast to the spring, rainfall rates in the summer are lower by about 0.6 mm/day (15%) in 21C compared to 20C over much of the Midwest, where the largest warming of the surface (~ 3 K) occurs (Figs. 19c and d). This projection of summer drying is consistent

with previous studies (Manabe et al. 1981; Wetherald and Manabe 2002; Hayhoe et al. 2007; IPCC 2007) and is discussed in Patricola and Cook (2013). The largest decrease of rainfall occur over the eastern Gulf coast (~1 mm/day). Similar to the annual convective precipitation differences, enhancements of 1 mm/day (35%) and 0.6 mm/day (10%) occur over the Northeast and the Carolinas, respectively.

In the 21C simulation, convective precipitation increases in most regions of the Midwest in the fall, similar to the spring (Fig. 19e). Enhancements of about 0.5 mm/day (30%) occur over much of the Midwest, where the largest rise in surface temperature (~ 2.4 K) arises (Fig. 19f). The eastern Gulf coast exhibits decreased convective precipitation in the future, for example, reductions of around 0.3 mm/day (10%) develop in Florida over a surface that is about 2 K warmer.

Differences in precipitation show some seasonality. Differences are positive in the spring and fall, while they are negative in the summer. This is consistent with previous global warming studies (Gao et al. 2014; Singh et al. 2013). For example, regional climate model projects intensification of up to 20% in the spring and fall precipitation while greater than -30% reduction occur in the summer of the mid-21st century (Singh et al. 2013). Association between modeled precipitation and surface temperature changes under global warming is examined next.

The Clausius-Clapeyron scaling argument predicts that precipitation will increase by 7% for every 1 K temperature increase (7%/K), scaling with increases in the saturation vapor pressure. Here we examine that prediction. Differences between the 21C and 20C

simulations are categorized into four ranges, namely, (1) negative %/K, (2) sub-CC for 0 - 6%/K, (3) CC for 6 - 8%/K, and (4) super-CC for values greater than 8%/K.

Percentage changes in the total and convective precipitation for each 1 K of surface warming are shown for the March-April-May (Figs. 20a and b), June-July-August (Figs. 20c and d), and September-October-November (Figs. 20e and f) means. In the spring, large areas have sub-CC precipitation increases (yellow shading), with smaller regions of super-CC increases (blue shades) over parts of the central Midwest, Northeast, and Florida. There are also regions with negative values (red shading) dominating the western part of the domain, and scattered smaller regions in the north and northeast.

Differences in the convective component of the rainfall scaled by temperature change (Fig. 20b) account for much of the structure in the total (Fig. 20a). Values of the scaled convective precipitation differences are shifted to higher values compared with the values for total precipitation (Fig. 20a) everywhere in the spring except in the southeast, where the non-convective component (not shown) is largely sub-CC. The east coast experiences super-CC increases in convective precipitation, as do southern Canada, southern Florida, and large portions of the mid-west.

As shown in Fig. 19c, decreases in convection precipitation are common across the domain in the summer. Figs. 20c and d show that even regions with increased total and convective rainfall are sub-CC, for example, the northern Midwest. The Clausius-Clapeyron relation completely fails to predict the change in precipitation per degree warming during this season. The only exception is in New England, where sub-CC

increases in the total scaled precipitation differences are replaced with CC and slightly super-CC increases in the convective component.

As was the case for convective precipitation, differences in the scaled total and convective precipitation in the fall (Figs. 20e and f) are similar to the spring differences (Figs. 20a and b) over most of the domain. Differences in the scaled total precipitation are primarily sub-CC and negative, while differences in the scaled convective precipitation range above and below 7%/K. Again, New England experiences very high super-CC increases in convective precipitation. Scaled precipitation reductions, up to 7%/K, over Florida and Georgia are similar to the summer response in these regions (Figs. 20c and d).

In summary, the relationship between convective precipitation and the Clausius-Clapeyron scaling relation represents the relationship between the total precipitation and surface temperature in the spring and fall. In the summer, precipitation is generally lower in the 21C simulation compared with the 21C simulation, and predictions from the Clausius-Clapeyron relation fail.

Connection between surface temperature and precipitation in the Clausius-Clapeyron argument depends critically on the response of atmospheric moisture fields to the warming. One aspect is the assumption that relative humidity remains constant as the climate warms (Manabe and Wetherald 1967, 1975; Held and Soden 2000; Soden et al. 2005). However, the tropospheric relative humidity does not exactly remain unchanged in this case, and it also shows some regional and seasonal dependence. For these reasons, tropospheric relative humidity changes for each 1 K of surface warming is evaluated. Tropospheric average relative humidity is calculated by averaging the weighted relative

humidity vertically-integrated from the surface to the top. As a representative of the lower troposphere, the lowest model level, 2-m, above the surface is selected. Since the analysis focuses only over land, 2-m relative humidity can be expected to be closely associated with the availability of soil moisture and evaporation from the surface. 2-m relative humidity in the 21C and 20C simulations is calculated from the simulated 2-m temperature and specific humidity by using equations in common use for calculating relative humidity (e.g., Peixoto and Oort 1996; Ross and Elliott 1996).

Tropospheric average relative humidity and 2-m relative humidity percentage changes for each 1 K of surface warming are shown in Figure 21 for the March-April-May (Figs. 21a and b), June-July-August (Figs. 21c and d), and September-October-November (Figs. 21e and f) means. Tropospheric and 2-m relative humidity increase in most regions of the country in the spring, with up to 2%/K increases in the central Midwest and the Northeast (Figs. 21a and b). Some regions show reduction. For example, up to -2%/K reduction occur in the southern central U.S. and the Gulf coast. In contrast to the spring, reductions occur in most regions in the summer (Figs. 21c and d). Tropospheric relative humidity reduces by -1%/K in most parts of the central U.S., and some regions over Kansas and Florida show up to -2%/K reduction. Regions to the east of the Rockies show up to -2%/K reduction in 2-m relative humidity. Both measures of relative humidity show increases in some regions. For example, tropospheric relative humidity increases by 1%/K in the western Gulf coast and parts of the Great Lakes, and 2-m relative humidity enhances by 1%/K in the Northeast. Again in the fall, most regions of the country show increases in the tropospheric relative humidity (Fig. 21e). Increases are up to 2%/K in the central Gulf

coast and the Northeast. Similar to the tropospheric relative humidity, 2-m relative humidity enhances by about 2%/K in the central Gulf coast and southern central U.S. (Figs. 21e and f). There are some noticeable differences in the tropospheric and 2-m relative humidity changes in the central Midwest. For example, 2-m relative humidity reduces by up to -2%/K, while the tropospheric relative humidity shows some increases.

Fig. 21 indicates that there are some differences in relative humidity on regional and seasonal scales, and the relative humidity does not exactly remain constant under global warming. Such differences in relative humidity are also exhibited by other global warming studies (Richter and Xie 2008; Sherwood et al. 2010; Xie et al. 2010), as an example, CMIP3 AOGCMs for SRES A1B emission scenario show up to -2%/K reduction in relative humidity over the U.S. for the end of the 21st century (O'Gorman and Muller 2010). Here, in the analysis region, increases, up to 2%/K, occur in the spring and fall, while reductions of about -2%/K occur in the summer for the mid-21st century. Contributions of these relative humidity differences to specific humidity differences are discussed below.

Atmospheric moisture fields, mass weighted specific humidity vertically-integrated from the surface to the top of the troposphere and 2-m specific humidity, are analyzed for two reasons. First, to connect them with precipitation, and the second is to compare the atmospheric moisture changes under global warming with the Clausius-Clapeyron scaling argument. Analysis of 2-m specific humidity, which can be expected to be closely associated with the surface, helps connect the moisture fields with the surface.

Percentage changes in the tropospheric and 2-m specific humidity for each 1 K rise in surface temperature in the 21C simulation are shown in Figure 22 for the March-April-May (Figs. 22a and b), June-July-August (Figs. 22c and d), and September-October-November (Figs. 22e and f) means. In the spring, tropospheric moisture increases everywhere in the domain (Fig. 22a). As was the case for the temperature-scaled convective precipitation, increases generally exceed the Clausius-Clapeyron predictions in the central Midwest and the Northeast (Figs. 22a and 20b). Moisture increases generally follow the Clausius-Clapeyron relation over the central Gulf coast and northern Midwest, while increases are sub-CC in western Texas, Florida and parts of the Great Lakes. Scaling of the 2-m specific humidity is similar to that of the vertically-integrated specific humidity in the Northeast, the eastern Gulf coast and western Texas (Fig. 22b). 2-m specific humidity increases generally follow the Clausius-Clapeyron relation in the central Midwest, where the convective component of precipitation matches the theoretical prediction. In the central U.S., specific humidity variables increase up to 10%. Of this 10%, about 2% is associated with the relative humidity (Figs. 21a and b). Generally, specific humidity increases closely follow the Clausius-Clapeyron relation in regions where differences in relative humidity are small, up to ± 1%, Western Texas, Western and Northern Midwest, for example.

In the summer, increases in the scaled vertically-integrated and 2-m specific humidity fields are sub-CC throughout the domain with the exception of the Northeast (Figs. 22c and d). Regions with sub-CC increases in the moisture fields are associated with negative and sub-CC differences in precipitation (Figs. 20c and d). In most regions to the east of the Rockies, increases of specific humidity variables are mostly sub-CC, where

reductions of up to -2%/K in relative humidity occur in the summer (Fig. 21c and d). Specific humidity variables increase roughly by about 12% in the central Midwest, as shown by Figs. 19 and 21. These imply that if the relative humidity had remained constant, for the simulated changes in temperature, specific humidity would have increased by about 14%. This indicates that the contribution of changes in relative humidity to specific humidity is much larger in the summer than in the spring. Associated with the reductions in relative humidity, 2-m specific humidity increases are lower than the Clausius-Clapeyron predictions in most regions of the U.S. 2-m specific humidity and tropospheric moisture increases follow the Clausius-Clapeyron relation in the Northeast, where differences in the relative humidity are small.

Tropospheric moisture increases most closely follow the Clausius-Clapeyron relation in the fall (Fig. 22e). Over Louisiana, increases in both moisture variables and precipitation exceed the Clausius-Clapeyron predictions (Figs. 22e, f, and 20f). Increases in the moisture terms differ in the central U.S., where 2-m specific humidity increases are smaller than both the vertically-integrated specific humidity and the theoretical predictions. Differences between the vertically-integrated and 2-m specific humidity also occur in the Northeast. Here, the 2-m specific humidity increases follow the Clausius-Clapeyron relation, while the lower tropospheric moisture increases are super-CC, meaning that the moisture is greater in the vertical column of the troposphere than near the surface. Figures 22e and f also indicate that the scaled vertically-integrated specific humidity increases are more consistent with the Clausius-Clapeyron scaling argument than the 2-m specific humidity increases in the northern Midwest, where the modeled precipitation matches the

theoretical prediction (Figs. 20e and f). Vertically-integrated specific humidity and 2-m specific humidity increases up to 10%/K in the southern central U.S. and the central Gulf coast, where relative humidity increases by about 3%/K. Implying that about one-third of changes in the specific humidity are associated with changes in relative humidity.

In summary, increases in 2-m specific humidity are in better agreement with the Clausius-Clapeyron scaling argument than the vertically-integrated specific humidity in the region to the east of the Rockies, where differences in relative humidity are small, up to ± 1%/K. Increases in 2-m specific humidity closely follow the Clausius-Clapeyron scaling argument in the analysis region, where increases in the convective component follows the theoretical prediction from the Clausius-Clapeyron relation (Figs. 22a, b and 7b). In contrast, specific humidity increases fall below the Clausius-Clapeyron prediction in the summer (Figs. 22c and d). In the fall, vertically-integrated specific humidity increases match better with the Clausius-Clapeyron scaling argument than the 2-m specific humidity, and increases in the moisture fields range from CC through super-CC in the southern Midwest and the Gulf coast, where the convective precipitation increases also range from CC through super-CC (Figs. 22e, f and 20f). East of the Rockies, increases in the vertically-integrated specific humidity follow the Clausius-Clapeyron relation, where relative humidity differences are small, up to ± 1%/K.

Figures 20-22 suggest that there are regional and seasonal scale differences in the temperature scaled precipitation and moisture fields, simulated precipitation deviates from the theoretical prediction, and differences in relative humidity are not negligible. Modeled precipitation matches the Clausius-Clapeyron prediction in the spring, but precipitation

reduces and the prediction fails in the summer. These differences are in some part associated with relative humidity differences, as discussed above, and also the assumptions used in formulating the Clausius–Clapeyron relation. The relation assumes that the surface underlying the air is a plane of water, which is of course saturated, in a closed isothermal system. However, in this case, the system is neither closed nor isothermal, and the land surface is not generally saturated, too. In order to understand the role of soil moisture distributions on the surface condition, for example, surface temperature, and to understand the differences between the theoretical and modeled precipitation, soil moisture differences in the 21C and 20C simulations are evaluated.

Soil moisture differences between the 21C and 20C simulations are displayed in Figure 23 for the March-April-May (Fig. 23a), June-July-August (Fig. 23b), and September-October-November (Fig. 23c) means. Soil becomes wetter by about 15×10^{-3} m^3-H_2O/m^3-soil (15%) in the 21C than in 20C simulation over the Midwest and Northeast in the spring (Fig. 23a). Increased soil moisture, is associated with CC increases of 2-m specific humidity and precipitation (Figs. 20a, b and 22b).

In contrast to the spring, soil becomes drier by about 25×10^{-3} m^3-H_2O/m^3-soil (15%) in the analysis region in the summer (Fig. 23b). Region with the depleted soil moisture is associated with sub-CC increases of 2-m specific humidity (Fig. 22d). Decreased soil moisture is linked with reductions in relative humidity in the central U.S., where the surface warms by as much as 3 K in the future (Fig. 19d). Again in the fall, soil moisture increases, up to 15×10^{-3} m^3-H_2O/m^3-soil, in the Gulf coast and the southern central U.S., similar to the spring (Fig. 23c).

Overall, increases in soil moisture are associated with increases of convective precipitation in the spring and fall (e.g., Figs. 19a and 23a). Consistent with this, observations have shown increases of convective precipitation with the soil moisture (Eltahir 1998, 2001). On the contrary, reductions of soil moisture are associated with decreases convective precipitation (e.g., Figs. 19b and 23b).

Moist static energy (MSE) profiles are analyzed to explore the association between soil moisture and precipitation differences in the 21C and 20C simulations. MSE is a linear combination of sensible, latent and geopotential energy, expressed as:

$$\text{MSE} = c_p T + L q + g z, \quad (1)$$

where c_p *(J kg^{-1} K^{-1})*is the specific heat of air at constant pressure, *T (K)* is air temperature, *L (J kg^{-1})* is the latent heat of vaporization, *q (kg kg^{-1})* is specific humidity, *g (m s^{-2})* is the acceleration due to gravity and *z (gpm)* is geopotential height. A stable atmosphere will have MSE increasing with elevation, and a high value of MSE at low levels destabilizes the atmospheric column.

MSE profile differences in the 21C and 20C simulations are displayed in Figure 24 for the March-April-May (Fig. 24a), June-July-August (Fig. 24b), and September-October-November (Fig. 24c) means. The MSE profiles for the spring are averaged over the region, as indicated in Figs. 23a, where increases in soil moisture occur, and the summer MSE profile is averaged over the region where striking reduction in soil moisture occurs in the future simulation, as indicated in Fig. 23b. Reason for selecting averaging region for the fall is similar to the spring (Fig. 23c). In the spring, the anomalous MSE profile (solid line) has a negative slope in the low-level below 800 hPa indicating that the lower troposphere

is more unstable in the 21C than in the 20C simulation (Fig. 24a). The troposphere is warmer and the temperature component is more stable (c_pT; dashed line). The tropospheric instability in large part is due to the moisture profile (Lq; dotted line), which has a negative slope. Associated with this unstable moisture profile, convective precipitation enhances (Fig. 19a). Change in geopotential energy (gz; light dashed line) is small, and it tends to stabilize the troposphere.

Anomalous MSE (solid line) profile has a negative slope, meaning that the troposphere is unstable in the summer (Fig. 24b). This instability is largely due to temperature profile. The anomalous moisture profile remains stable in the low-level below 750 hPa, with a small region of instability below 950 hPa. The moisture profile is stable. Associated with the unstable temperature profile, the convection is dry and reduction of precipitation occurs (Fig. 19b).

Similar to the spring, the tropospheric instability is due to the moisture profile, while the temperature profile remains stable in the fall (Fig. 24c). Associated with this unstable moisture profile, precipitation increases in the future in the southern central U.S. (Fig. 19c).

In summary, increases of convective precipitation are associated with increases of soil moisture in the spring and fall. In contrast, reduction of precipitation is associated with reduction of soil moisture in the summer.

3.7. CONCLUSIONS

Climate models predict that precipitation becomes more intense due to global warming in the future. This understanding is founded on the Clausius–Clapeyron relation, which relates a 7% increase in saturation mixing ratio for each 1 K surface warming, and the fact that the relative humidity remains constant under global warming. Here, theoretical precipitation predicted from the Clausius–Clapeyron equation is compared with the model simulations for the mid–21st century, and the physics of the departure of the model from the theory is explored. This study builds on the simulations performed by Patricola and Cook (2013a, 2013b).

The total (convective + non-convective + snow + graupel) annual precipitation in the region to the east of the Rockies, in the analysis region, is up to 0.3 mm/day larger in the 21C simulation than in the 20C simulation, and most increases are due to the convective component. For this reason, convective precipitation differences are used to compare with the theoretical predictions from the Clausius-Clapeyron relation on regional and seasonal scales.

In the analysis region, convective precipitation enhances, up to 0.5 mm/day, in the spring and fall, while reductions, up to -0.5 mm/day, occur in the summer in the 21C simulation. Surface temperature is always greater in the future, and the distribution of precipitation differences do not follow the distribution of surface temperature warming. For example, up to 20% precipitation increases are located over the analysis region, where smallest increases, up to 1 K, in surface temperature occur in the spring. In contrast, precipitation lowers, up to -15%, in the summer in the analysis region, where the largest

warming, up to 3 K, of the surface occurs. Again in the fall, precipitation enhancement of up to 30% is shown by the region to the east of the Rockies, where the largest warming, up to 2.4 K, occurs. This deviation of precipitation changes from surface temperature differences is explored further.

Precipitation is scaled by surface temperature to compare the simulated values with the theoretical predictions from the Clausius-Clapeyron scaling argument, which predicts that precipitation increases by 7% for every 1 K temperature increase (7%/K). Based upon this, differences in the 21C and 20C simulations are categorized into four ranges: (1) negative %/K, (2) sub-CC for 0 - 6%/K, (3) CC for 6 - 8%/K, and (4) super-CC for values greater than 8%/K. In the spring, precipitation increases range from CC through super-CC in the central Midwest. In contrast, negative precipitation differences dominate, and predictions from the Clausius-Clapeyron relation completely fail in the summer. In the fall, convective rainfall increases, and the increases follow the theoretical predictions. To connect precipitation with the tropospheric moisture, and to compare the molded moisture changes with the Clausius-Clapeyron scaling argument, tropospheric moisture fields are analyzed next.

In the spring and fall, vertically-integrated specific humidity increases are super-CC, while increases in the 2-m specific humidity closely follow the Clausius-Clapeyron relation in the analysis region, where the modeled convective precipitation matches the theoretical prediction. In general, vertically-integrated and 2-m specific humidity increases closely follow the Clausius-Clapeyron relation in the analysis region, where relative humidity differences in the 21C and 20C simulations are small. In contrast, increases in the

moisture fields are sub-CC accompanied by much larger differences in relative humidity in the summer. The smallest increases, up to 4%/K, in specific humidity are located over the central Midwest, where largest reduction, about -2%/K, in relative humidity occurs.

Modeled precipitation follows the theoretical prediction in the spring, but precipitation lowers and the prediction fails in the summer. Besides relative humidity changes, as discussed above, these differences are associated with the assumptions used in the Clausius–Clapeyron relation, which assumes that the surface underlying the air is a plane of water and is saturated. For this reason, soil moisture differences are explored.

Soil becomes wetter, up to 15%, in the 21C than in 20C simulation in the analysis region, where the specific humidity increases follow the Clausius-Clapeyron relation, and the simulated precipitation matches the theoretical prediction in the spring and fall. In contrast, soil becomes drier, up to - 15%, in the summer. Associated with the depleted soil moisture, theoretical prediction fails.

Moist static energy profiles are explored to understand the association between soil moisture and precipitation changes. In the spring and fall, the tropospheric moisture profile is unstable, and associated with the moist convection, increases of precipitation occur. In contrast, associated with the reduction in soil moisture, there is dry convection and precipitation reduction occurs in the summer.

In conclusion, modeled tropospheric moisture fields and precipitation follow the theoretical predictions from the Clausius-Clapeyron relation in the region to the east of the Rockies, and this is associated with increases of soil moisture, in the spring and fall, for

example. In contrast, simulated precipitation and moisture values fall below the theoretical predictions in the summer and this is associated with reduction of soil moisture.

3.8. ACKNOWLEDGEMENTS

Department of Energy (Award DE-FG02-10ER65092) is gratefully acknowledged. This study builds upon the simulations performed by Patricols and Cook (2013a and b). The authors acknowledge Dr. Christina M. Patricola, and Dr. Kerry H. Cook for providing the simulations. The Texas Advanced Computing Center (TACC) at the University of Texas at Austin provided the high-performance computing and database resources. The authors also acknowledge Dr. Edward K. Vizy for his helpful discussions and suggestions.

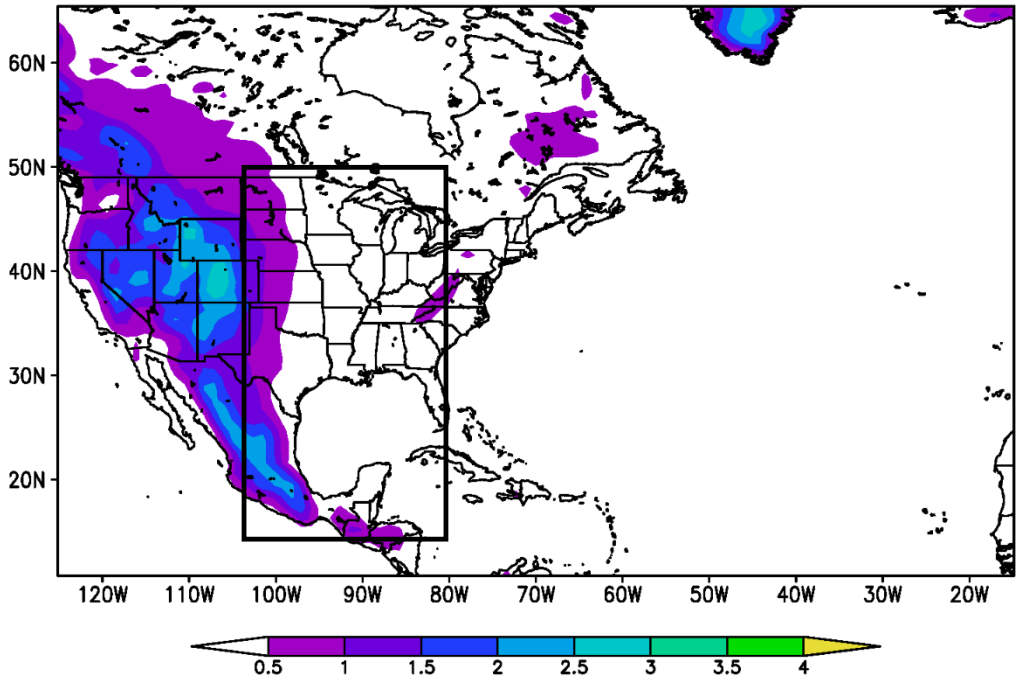

Figure 14. Topography (shaded, km) at 90 (30) km resolution on the parent (nested) domain.

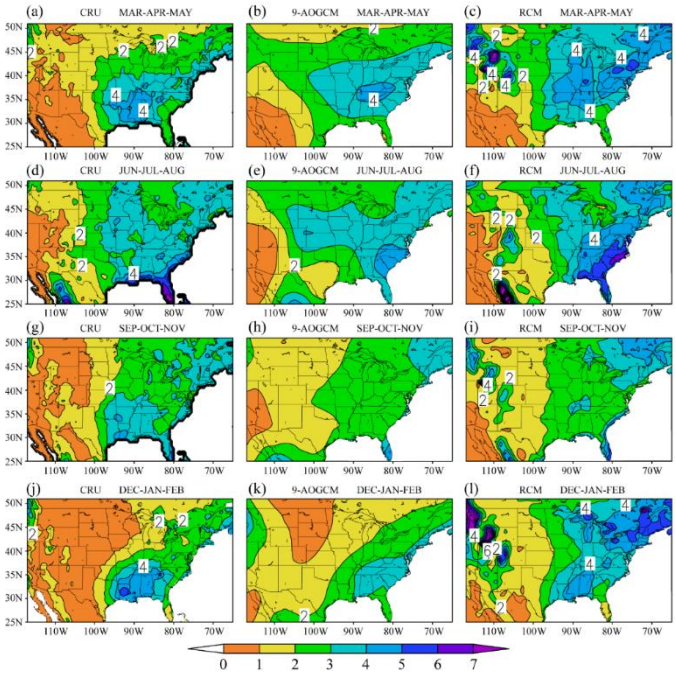

Figure 15. Precipitation rate (mm/day) averaged **a, b, c** March-April-May, **d, e, f** June-July-August, **g, h, i** September-October-November, and **j, k, l** December-January-February of 1981-2000 from the CRU TS3.0 at 0.5° resolution, the average of nine atmosphere–ocean GCMs (Canadian Centre for Climate Modeling and Analysis CGCM3.1(T47), Météo-France/Centre de Recherches Météorologiques CNRM-CM3, Max Plank Institute for Meteorology ECHAM5/MPI-OM, NOAA Geophysical Fluid Dynamics Laboratory GFDL-CM2.0, Center for Climate Research MIROC3.2 (medres), Meteorological Research Institute MRI-CGCM2.3.2, National Center for Atmospheric Research CCSM3, National Center for Atmospheric Research PCM, and the Hadley Centre for Climate Prediction and Research/ Met Office UKMO-HadCM3) interpolated at 2.5° resolution, and RCM at 90 km resolution, respectively. Values over the ocean are masked.

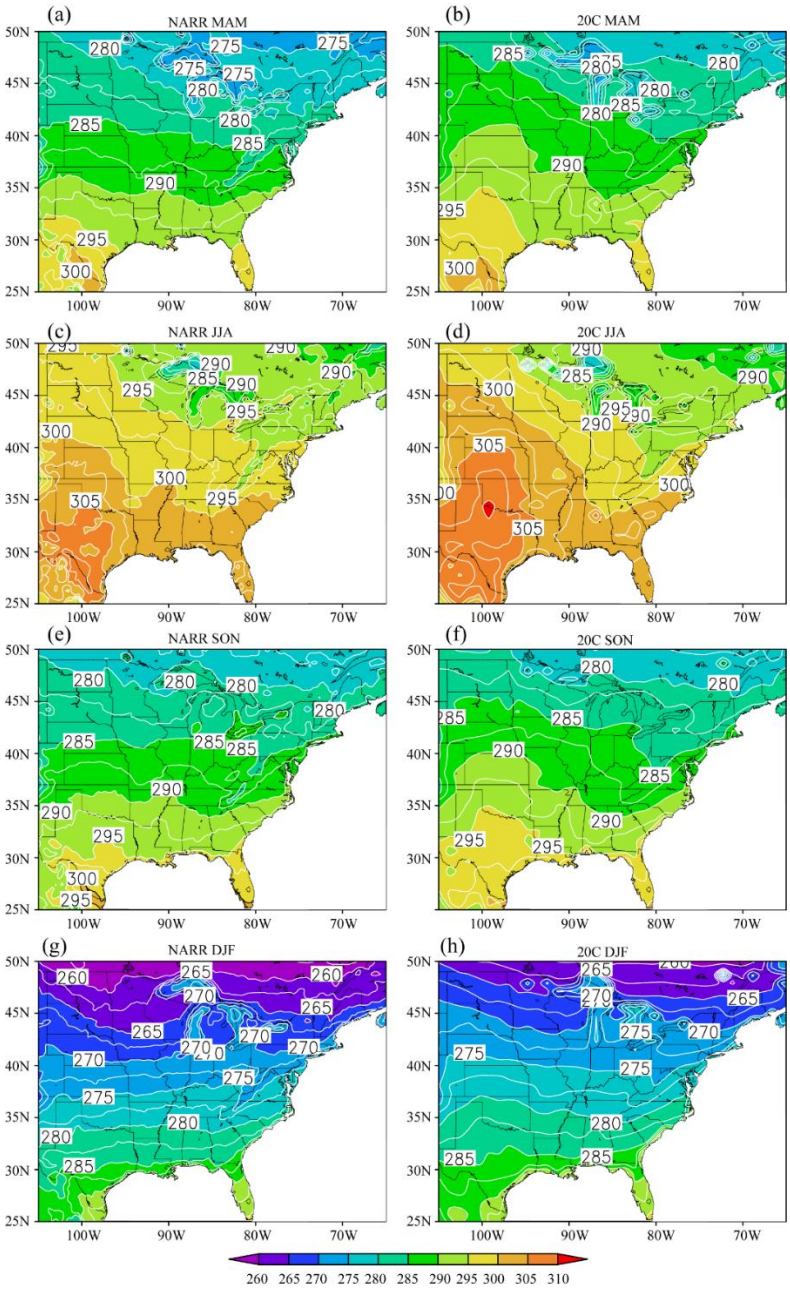

Figure 16. (a)-(h) Surface skin temperatures (K) over land for the traditional seasons from the 1981-2000 NARR climatology (left) and 20C simulation ensemble mean (right). The CI is 2.5 K.

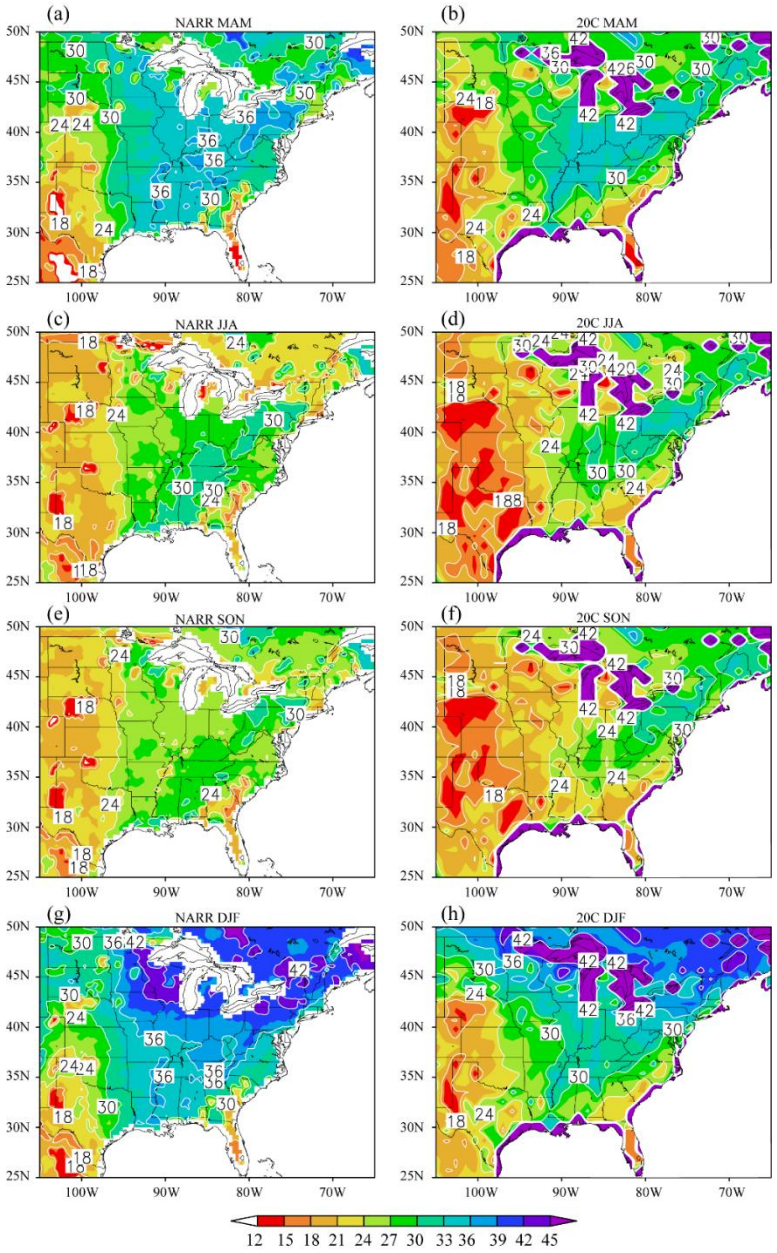

Figure 17. (a)-(h) Top 10 cm soil moisture fraction ($\times 10^{-2}$ m^3/m^3) for the traditional seasons from the 1981-2000 NARR climatology (left) and 20C simulation ensemble mean (right). The CI is 6×10^{-2} m^3/m^3.

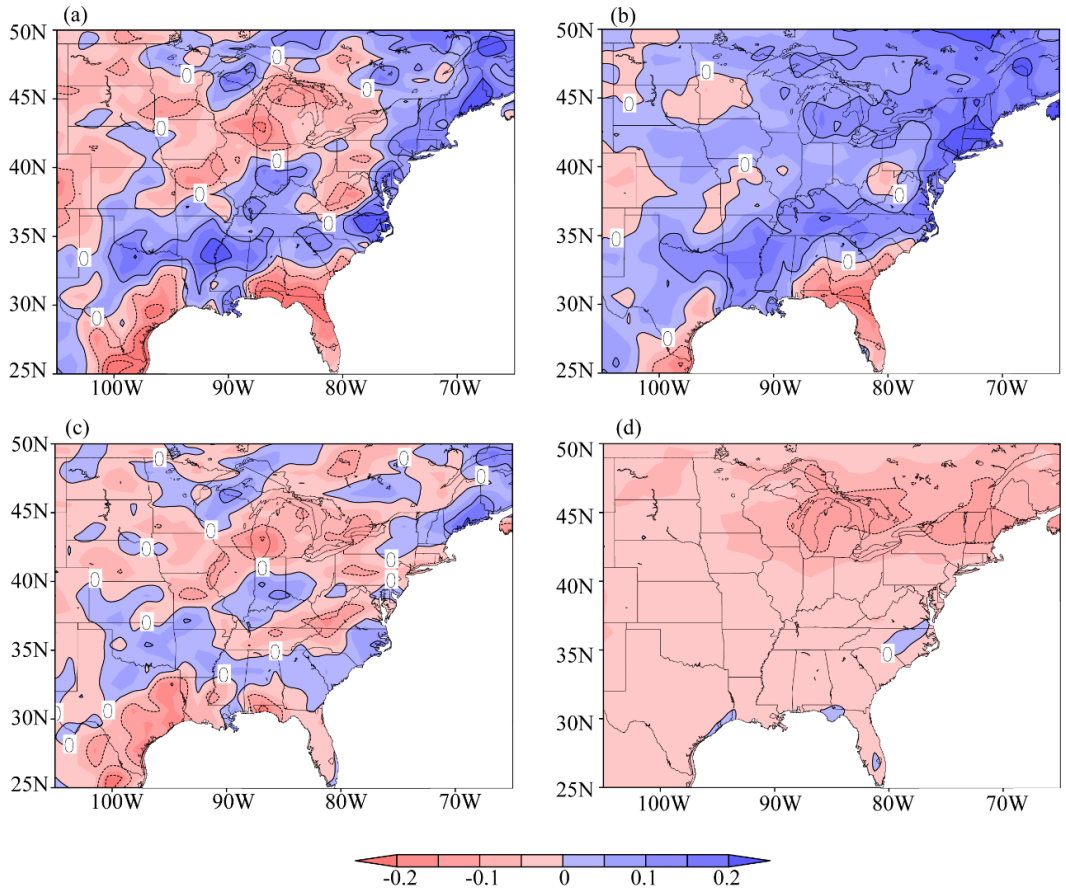

FIG. 18. Differences between the 21C and 20C simulations for annual mean (a) total (convective+non–convective+snow+graupel), (b) convective, (c) non–convective, and (d) snow and graupel precipitation (mm/day). Contour interval is 0.1 mm/day. Values over the ocean are masked.

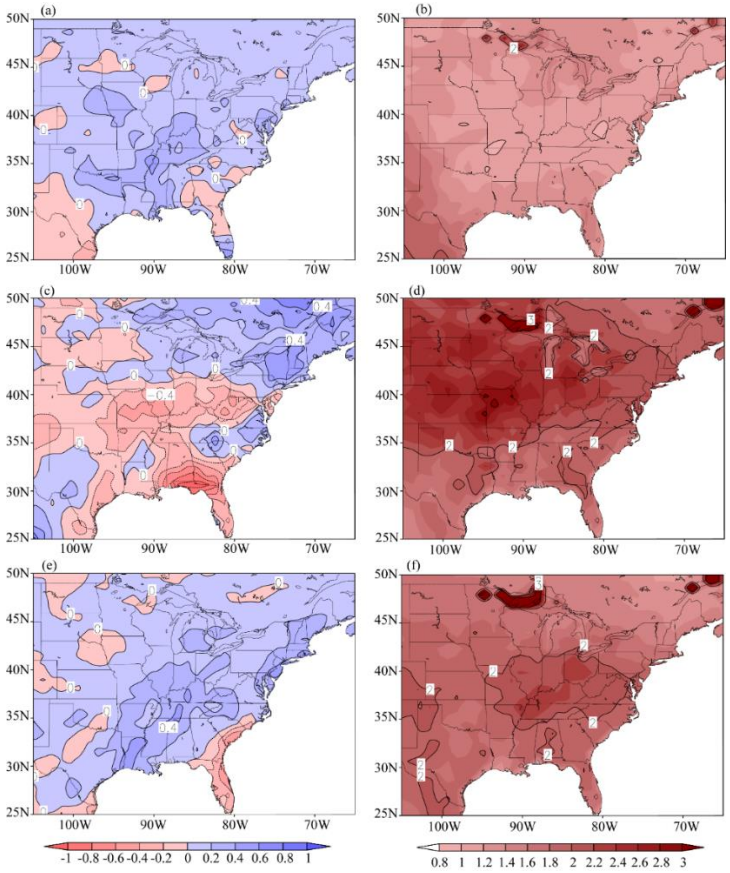

FIG. 19. Differences between the 21C and 20C simulations for (a) convective precipitation (mm/day) and (b) surface temperature (K) for the March-April-May mean. Differences between the 21C and 20C simulations for (c) convective precipitation (mm/day) and (d) surface temperature (K) for the June-July-August mean. Differences between the 21C and 20C simulations for (e) convective precipitation (mm/day) and (f) surface temperature (K) for the September-October-November mean. Contour interval is 0.2 mm/day for the precipitation difference. Surface temperature differences of 1K, 2K, and 3K are contoured. Values over the ocean are masked.

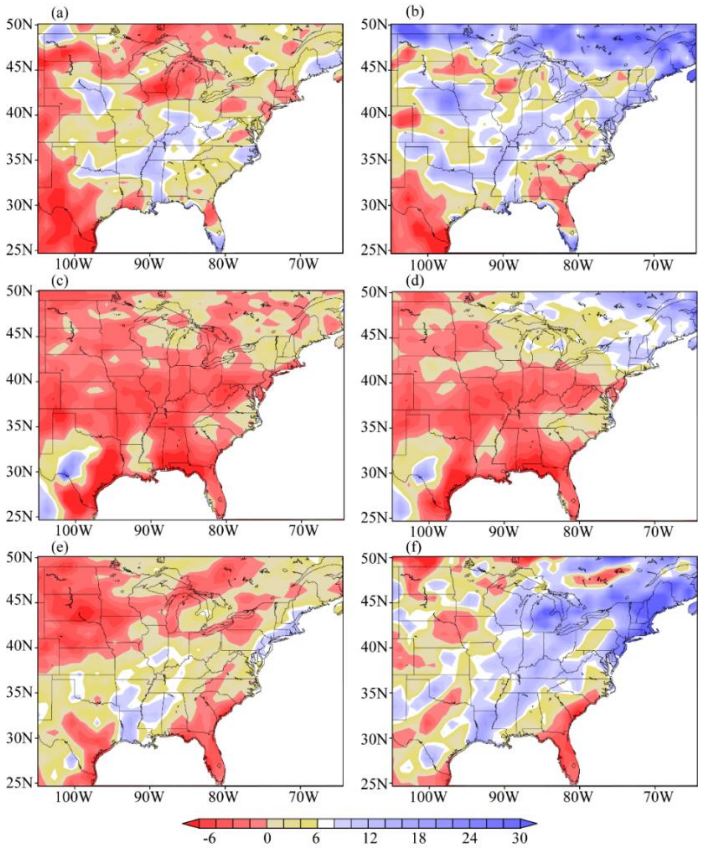

FIG. 20. Percentage differences in the (a) total and (b) convective precipitation rates for each 1 K of surface warming between the 21C and 20C simulations for the March-April-May mean. Percentage differences in the (c) total and (d) convective precipitation rates for each 1 K of surface warming between the 21C and 20C simulations for the June-July-August mean. Also, percentage differences in the (e) total and (f) convective precipitation rates for each 1 K of surface warming between the 21C and 20C simulations for the September-October-November mean. Negative values are shaded red, 0 - 6%/K (sub-CC) are shaded yellow, 6 – 8%/K (CC) are shaded white, and values above 8%/K (super-CC) are shaded blue. Values over the ocean are masked.

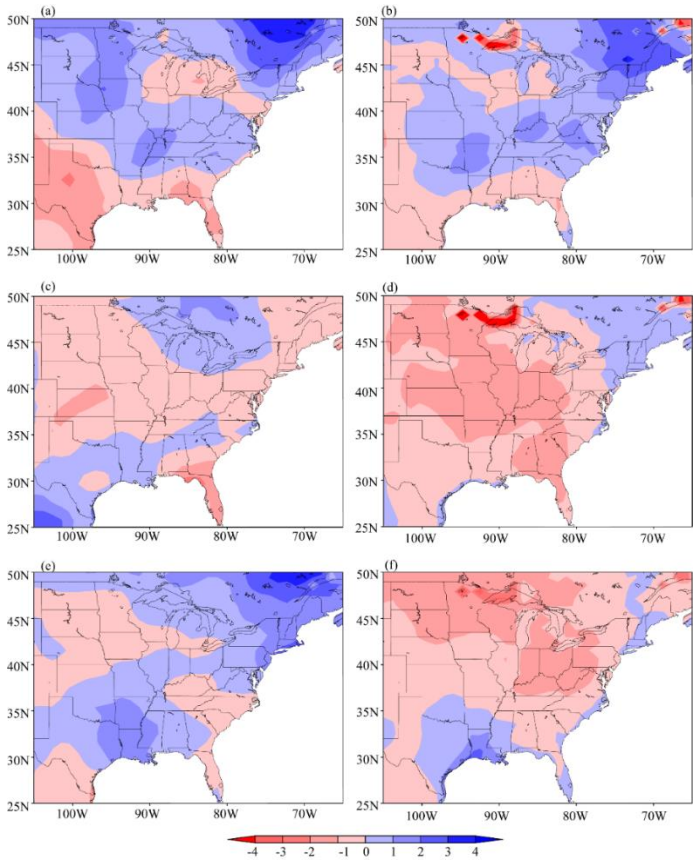

FIG. 21. Percentage differences in the (a) tropospheric average relative humidity and (b) 2-m relative humidity for each 1 K of surface warming between the 21C and 20C simulations for the March-April-May mean. Percentage differences in the (c) tropospheric average relative humidity and (d) 2-m relative humidity for each 1 K of surface warming between the 21C and 20C simulations for the June-July-August mean. Also, Percentage differences in the (e) tropospheric average relative humidity and (f) 2-m relative humidity for each 1 K of surface warming between the 21C and 20C simulations for the September-October-November mean. Values over the ocean are masked.

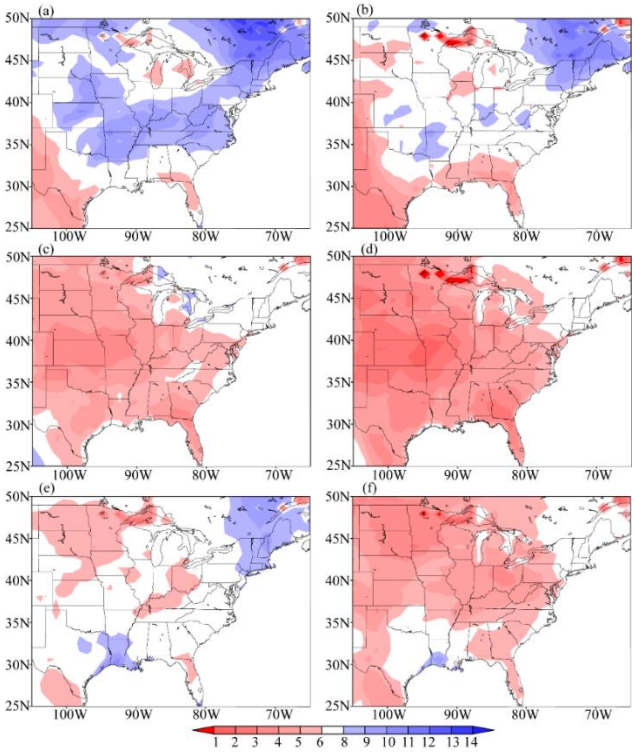

FIG. 22. Percentage differences in the (a) tropospheric specific humidity and (b) 2-m specific humidity for each 1 K of surface warming between the 21C and 20C simulations for the March-April-May mean. Percentage differences in the (c) tropospheric specific humidity and (d) 2-m specific humidity for each 1 K of surface warming between the 21C and 20C simulations for the June-July-August mean. Also, percentage differences in the (e) tropospheric specific humidity and (f) 2-m specific humidity for each 1 K of surface warming between the 21C and 20C simulations for the September-October-November mean. 0 - 6%/K (sub-CC) are shaded red, 6 – 8%/K (CC) are shaded white, and values above 8%/K (super-CC) are shaded blue. Values over the ocean are masked.

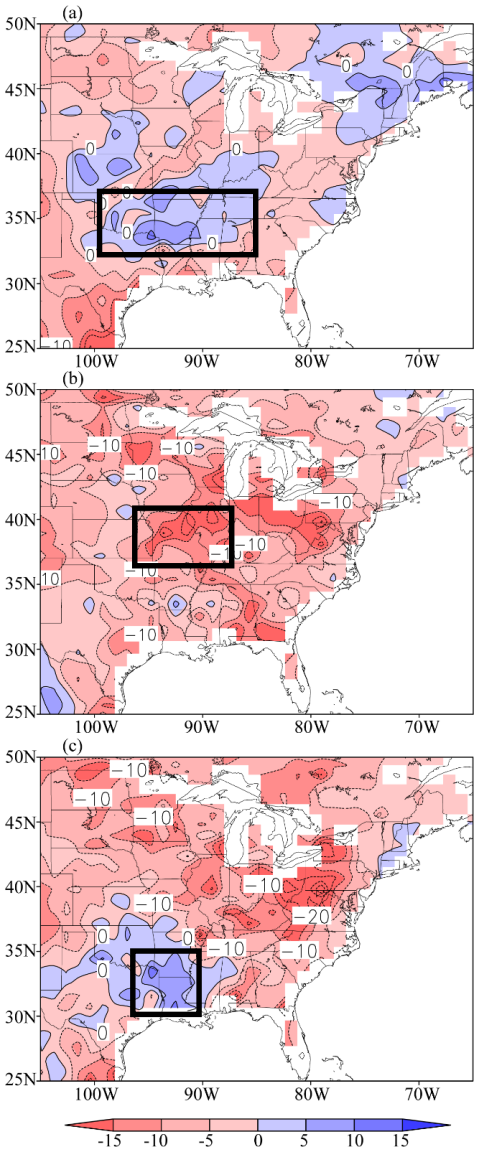

FIG. 23. Differences between the 21C and 20C simulations for the top 10 cm volumetric soil moisture [$\times 10^{-3}(m^3/m^3)$] for the (a) March-April-May, (b) June-July-August, and (c) September-October-November means, with boxes in (a) 100°W–84°W; 32°N–36°N, (b) 97°W–88°W; 37°N–42°N, and (c) 95°W–90°W; 30°N–35°N, to indicate regions for averaging. Contour interval is $5\times 10^{-3} m^3/m^3$. Values over the ocean are masked.

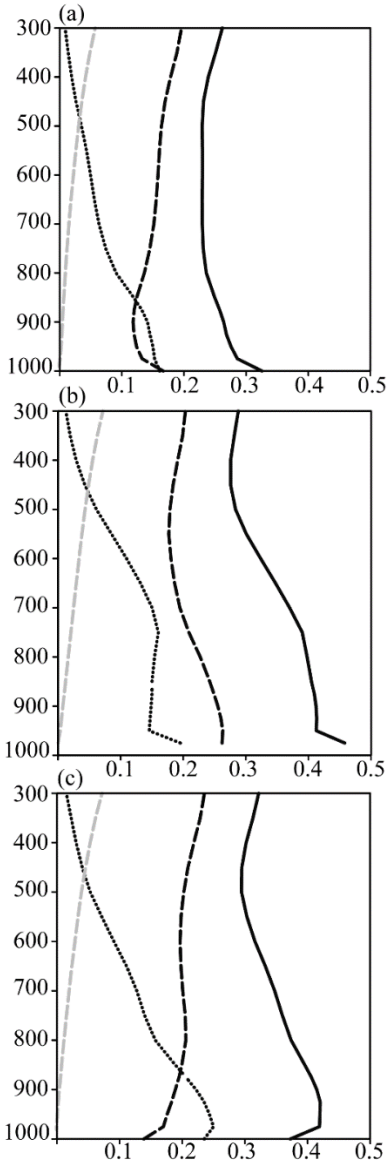

FIG. 24. Differences between the 21C and 20C simulations for MSE and its components ($\times 10^4$ j/kg) for the (a) March-April-May, (b) June-July-August, and (c) September-October-November averages over the region where soil moisture enhances in (a) and (c) and reduces in (b). Dashed (dotted) lines are the temperature (moisture) terms, faint dashed lines are the geopotential terms, and solid lines are the total MSE terms.

Chapter 4: Identification of a Congo basin Walker circulation [3]

4.1 ABSTRACT

The Gulf of Guinea in the equatorial Atlantic is characterized by the presence of strong subsidence at certain times of the year. This subsidence, which suppresses convection over the region, appears in June and is well established from July to September. Since much of the West African monsoon flow originates over the Gulf of Guinea, this subsidence is important for determining the moisture sources for the West African monsoon. Using reanalyses products here we contribute to a physical understanding of what causes this seasonal subsidence, and how it relates to precipitation distributions across West Africa.

We identify a seasonal Walker circulation above the Congo basin and the Gulf of Guinea in the ERA Interim, ERA40, NCEP2, and MERRA reanalyses. Up-branch is located in the Congo basin around 20°E. 600 hPa easterly flows constitute the returning-branch and sinking over the Gulf of Guinea forms the down-branch. The subsiding branch diverges at 2°W near the surface, with winds to the east flowing to the Congo basin to complete the overturning circulation. This Walker circulation is driven and maintained by

[3] Idea of this project was suggested by Kerry H. Cook. The project was completed under her careful guidance and supervision. Naresh Neupane wrote this chapter, and this was revised by Dr. Edward K. Vizy.

surface temperature differences between the eastern Gulf of Guinea and the Congo basin. Land temperatures remain almost uniform, around 298 K, throughout a year, but the Gulf of Guinea sea surface temperatures have pronounced seasonality characterized by rapid cooling, up to 4 K, from 294 K in May to about 290 K in August, in association with the formation of the Atlantic cold tongue. These temperature changes increase the ocean/land temperature contrast, up to 8 K, and drive the Congo basin Walker circulation in the boreal summer.

We hypothesize that when the Walker circulation is anomalously strong, the Gulf of Guinea subsidence, the monsoon flow, and moisture transport across West Africa are also strong. This hypothesis is supported by the ERAI reanalysis. However, the effects on precipitation are not clear in the TRMM data.

4.2. INTRODUCTION

Past studies (Trenberth et al. 2000; Wang 2002a, b, 2005; Nicholson and Webster 2007) indicate that atmospheric subsidence exists over the equatorial Atlantic with the strongest sinking occurring over the central and eastern equatorial Atlantic (i.e., over the Gulf of Guinea). However, the relationship between the Gulf of Guinea subsidence and local and regional climate variability over continental Africa is not yet well understood. For example, the Gulf of Guinea is known to be a primary moisture source for West African monsoon system (Vizy and Cook 2001; Grist and Nicholson 2001; Fontaine et al. 2003; Cook and Vizy 2006), hence fluctuations in subsidence may affect rainfall patterns over the adjacent African continent by altering the low–level circulation and moisture

convergence. Given Africa's strong reliance on rainfall for agricultural needs, it is important to improve our understanding of any mechanism(s) that influence rainfall variations over equatorial and West Africa.

The purpose of this study is to use available observational and reanalysis data products to document a seasonal scale subsidence in the Gulf of Guinea, physically understand the relationship between the seasonal Gulf of Guinea subsidence and large–scale regional circulation and rainfall patterns over Africa.

Section 2 provides background regarding our current state of understanding about subsidence over the Gulf of Guinea, including mechanisms that influence its strength. Section 3 describes the reanalyses and observational data used by this study. Results are presented in section 4, and conclusions are summarized in section 5.

4.3. BACKGROUND

There is an atmospheric subsidence in the low–level over the Gulf of Guinea at a certain time of the year. This subsidence is present in the Gulf during the boreal summer season (Hastenrath et al. 2001; Cook and Vizy 2006; Hastenrath and Polzin 2011). Relationship between the Gulf of Guinea subsidence and rainfall over the African continent has been discussed in the past. Using reanalyses and satellite observations, Leduc–Leballeur et al. (2012) show that the increases in the Guinean subsidence are related with the increases in convection over the northern Gulf of Guinea. In an observational study, Segele et al. (2009) suggest that the intensification of the Guinean surface pressure is associated with abundant rainfall in the northern Africa. Similarly, Nicholson and Webster

(2007) observed precipitation enhancement over the Sahel when the Guinean subsidence was strengthened in the NCEP reanalysis. Studies also indicated that the presence of this subsidence inhibits deep vertical transport of moisture over the Gulf and supports poleward moisture transport by the monsoon flow (Vizy and Cook 2001; Neupane and Cook 2013). These studies agree that the Guinean subsidence is important in influencing precipitation across West Africa, but causes of this subsidence and its seasonal variation remain still unclear.

It is interesting to note that there are a few studies that have explored this subsidence, but have drawn some slightly misleading conclusions. For example, some studies show the presence of a deep atmospheric meridional overturning circulation over the Atlantic, often referred to as "the Atlantic Hadley circulation", and relate the Guinean subsidence with the descending branch of the circulation, whose up–branch is located over the Sahel. Low–level flows from the equator toward the Sahel form the lower–branch, while the equatorward flows above 600 hPa form the returning-branch of the circulation. This circulation becomes most active during the boreal summer (Wang 2005; Wang et al. 2004; Trenberth et. al. 2000). An example can be found in Wang (2002a), who used 1950–1999 NCEP reanalysis climatology and averaged tropospheric circulation profiles from 10°W–10°E to show the subsiding branch of the Atlantic Hadley circulation. In addition, some other studies relate this subsidence with the descending branch of a shallow meridional overturning circulation that is embedded within the deep meridional overturning circulation. The shallow circulation comprises of surface southerly inflows from the Guinean Gulf and the northerly returning outflows between 700 and 500 hPa from

the Sahel as well (Thorncroft and Blackburn 1999; Nolan et al. 2007; Hagos and Zhang 2009; Zhang et al. 2006; Thorncroft et al. 2011).

Existence of the deep and shallow meridional overturning circulations, as discussed above, is somewhat deceiving. This is because, as the onshore southerly winds flow northward onto the continent, they tend to deviate eastward because of the action of zonal Coriolis acceleration, which is a function of meridional wind speed and latitude, $d\mathbf{u}/dt = 2\Omega v \sin\phi$, where $\Omega = 7.3 \times 10^{-5}$ *rad/s* is the angular speed of rotation of the Earth, v (m s^{-1}) is the meridional velocity, and ϕ is the latitude. For example, let us consider southerly wind of about 10 m s^{-1} at 0°E/Equator. If it maintains the same velocity, it is deflected as far as 22°E when it reaches up to 15°N in the Sahel. As discussed in the literatures mentioned above, such local scale complete overturning circulations with low–level inflows from the Gulf of Guinea to Sahel, such as the Atlantic Hadley circulation, e.g., Fig. 2g in Wang (2002a), appears so because of the zonal averaging. Therefore, presence of such a complete overturning circulation on a regional scale is slightly misleading. Reason being, the Coriolis force, which appears as soon as an air parcel is deflected in a meridional direction, and imparts zonal acceleration to the parcel, making it impossible to maintain a purely meridional flow. Under these circumstances, our focus in this study is on the Walker circulation that may be associated with the Guinean subsidence.

The zonal circulations along the equator, e.g., Walker circulation, remain unaffected by the Coriolis acceleration because $\phi = 0$ at the equator. A Walker circulation centered at 30°W along the equatorial Atlantic exists in the observations. Up-branch of the circulation is over the western Atlantic at 45°W, and down-branch is around the central Atlantic at

15°W. It varies on monthly timescales, with the subsiding branch reaching its maximum intensity in the boreal summer (Losada et al. 2010; Wang 2006; Gastineau et al. 2009). Though this circulation is along the equatorial Atlantic, here we are interested in Guinean subsidence, e.g., around 5°E, which is almost 20 degrees of longitude to the east of the down-branch of the Atlantic Walker circulation.

We envision a regional scale complete zonal circulation, which rises over the Congo basin and subsides over the Gulf of Guinea. This type of a regional scale zonal circulation, i.e., the Congo basin Walker circulation, has been discussed feebly in the past. Vizy and Cook (2001) hypothesized that a Walker circulation exists above the Congo basin and the Gulf of Guinea. In an attempt to understanding the mechanisms by which the Guinean and the eastern North Atlantic sea surface temperatures, SSTs, affect the summer rainfall across West Africa, they used an atmospheric general circulation model and performed a series of idealized simulations (e.g., nine perpetual–July simulations), forced with warm SST anomalies in the Guinean Gulf. Rainfall increased along the coast and decreased over the Congo basin when the SSTs were anomalously high, and it was found to be associated with a weakening of the Walker circulation. This Walker circulation can also be seen in a zonal and vertical wind streamlines along the equator in Fig. 2c of Lau and Yang (2002). They used 1949–1999 NCEP climatology for July to show the equatorial Walker circulations around the globe. In addition, sketches indicating the presence of this Walker circulation can be seen in Hastenrath (2006) and the references there in. They, however, do not discuss features, variability and physical basis for the existence of the Congo basin Walker circulation.

Here, first we report the existence of subsidence in the Gulf of Guinea in the boreal summer. Second, we identify a Congo basin Walker circulation, which is associated with the Guinean subsidence, and finally explore the circulation's variability.

4.4. DATA AND METHODOLOGY

Since there is some degree of uncertainty in the observations, various observational and reanalysis datasets are analyzed and compared to each other to build confidence in the findings. Each dataset is discussed briefly below.

Four reanalysis datasets are utilized to provide monthly mean information regarding the circulation, temperature, and geopotential height fields. They include the 1.125°–resolution ECMWF 40–year reanalysis (ERA40; Uppala et al. 2005), the 1.5°–resolution ERA–Interim (ERAI; Dee et al. 2011), the 2.5°–resolution National Centre for Environmental Prediction–Department of Energy Atmospheric Model Intercomparison Project II (NCEP2; Kanamitsu et al. 2002), and the 1.25°–resolution NASA Modern Era Retrospective analysis for Research and Application (MERRA; Rienecker et al. 2011). ERAI, MERRA, and NCEP2 cover the same 1979 – 2013 period, while ERA40 has data available from 1958 – 2002. The analysis will be conducted over the full available period to maximize the number of datasets to analyze over. The number of vertical levels differs between reanalyses, ranging from 17 levels in NCEP2, 23 levels in ERA40, 37 levels in ERAI, and 42 levels in MERRA. Analysis will focus on comparing standard levels among the different reanalyses.

To provide monthly surface information two observational datasets are also utilized. The first is the 0.25°-resolution NASA Tropical Rainfall Measuring Mission (TRMM 3B42V7; Kummerow et al. 1998) satellite–derived monthly rainfall product. This dataset provided high resolution rainfall estimates from 1998 – 2013. The second dataset is the 0.5°–resolution Climate Research Unit gridded monthly dataset (CRU; CRUTS3.21; Mitchell and Jones 2005). This dataset provides land–based monthly rainfall and surface temperature estimates from 1901 – 2012.

4.5. RESULTS

4.5.1 Identification of the Congo basin Walker circulation

ERAI 1979–2013 climatological vertical p–velocity [i.e., omega, $\omega \times 10^{-2}$ (Pa s^{-1})] at 900 hPa shown in figures 25a–l are for January–December, respectively. In January (Fig. 25a) there is rising motion along the equatorial Atlantic. Generally, this rising motion persists from February through April (Figs. 25b–d), with the replacement by sinking motion in some regions of the eastern Atlantic to the north of the equator. In May (Fig. 25e), the region to the north of the equator shows rising motion, while sinking motion prevails clearly to the south of the equator. In June (Fig. 25f) subsidence is strongest at this level over the equatorial Atlantic with maxima of 4–6 Pa s^{-1} over the central equatorial Atlantic (7°W–25°W) and the Gulf of Guinea near 8°E, clearly distinguished from the central Atlantic maxima. In July (Fig. 25g), both the central equatorial Atlantic and Gulf of Guinea subsidence maxima expand in spatial extent, with the latter extending from 4°E–10°E between 5°S–3°N. By August (Fig. 25h) the Gulf of Guinea subsidence maximum

reaches its peak strength of approximately 8 Pa s^{-1}, e.g., near 1°S and 8°E, while subsidence near 0°E extends northward up to 5°N. The maximum over the central equatorial Atlantic remains robust in size, but aloof from the Guinean maximum, for example, at Equator, 8°E. In September (Fig. 25i), this subsidence begins to weaken, decreasing by about 2 Pa s^{-1} compared to August over the Gulf of Guinea, while contracting meridionally back towards the equator over the central equatorial Atlantic. By October (Fig. 25j) the strongest subsidence has shifted south of the equator with rising motions occurring over the Atlantic north of 1°N. The rising motion extends southward in November and December (Figs. 25k, l). Over land rising vertical motions occur year round.

It is clear from Fig. 25 that the boreal summer is associated with subsidence over the equatorial Atlantic between 5°S–3°N with two centers of maximum intensity, one over the central Atlantic (Wang et al. 2004) and the other over Gulf of Guinea in the eastern Atlantic. Sinking motion maximizes over both the regions around June (Fig. 25f) and disappear around October (Fig. 25j). As stated in section 1 the focus of this paper is on the latter, namely to better understand the cause of subsidence over the Gulf of Guinea.

Fig. 25 also indicates that the Gulf of Guinea subsidence exhibits a distinct seasonal cycle. The subsidence in primarily located to the south of the equator from January through May. In June, it appears over the Gulf of Guinea and starts its northward progression. It becomes maximum and reaches its north most location around 5°N from July to September, then weakens and retreats primarily south of the equator by October. Other reanalyses (i.e., ERA40, NCEP2, and MERRA) exhibit a similar seasonal cycle in subsidence over the equatorial Atlantic (not shown).

Vertical cross sections of atmospheric circulations are analyzed next to help understand the cause of the Gulf of Guinea subsidence. Longitude–height cross section of zonal and vertical p–velocity wind components [u (m s^{-1}); $\omega \times 10^{-2}$ (Pa s^{-1})] averaged between 5°S–3°N from the ERAI reanalysis climatology (1979–2013) shown in figures 26a–l are for January–December, respectively. In January (Fig. 26a), there is rising motion around the Greenwich meridian in the Gulf of Guinea. This rising motion persists over the region from February through May, as indicated by the upward pointing streamlines (Figs. 26b–e). In June (Fig. 26f), there is a circulation near the surface between 0°E–20°E, with rising motions from the surface to 800 hPa over the Congo basin from 12°E–25°E, westward flow around 800 hPa from 15°E–0°E, and subsidence in the equatorial West African coast at 3°E. Westerly onshore flow from the Gulf of Guinea into the Congo basin is shallow, generally confined between the surface and 900 hPa extending inland to about 12°E. The vertical extent of the circulation appears to be predominantly confined to the boundary layer (i.e., the surface–800 hPa) with evidence of some mid–tropospheric (i.e., 700–400 hPa) rising (sinking) motion east (west) of 10°E. This circulation is identified as the Congo basin Walker circulation.

The Congo basin Walker circulation expands longitudinally and becomes vertically deeper in July (Fig. 26g). For example, the July rising branch is located near 15°E with easterly return flow now extending up to 650 hPa, and the down-branch (i.e., subsidence associated with the Walker circulation) centered at 0°E over the equatorial Atlantic. The longitudinal width of the Congo basin Walker circulation continues to expand in August (Fig. 26h) and September (Fig. 26i) with the rising branch centered near 20°E and the

sinking branch centered near 2°W by September. The Walker circulation begins to contract in size in October (Fig. 26j), though rising branch remains strong over the Congo during this time, and the Walker circulation disappears in November and December (Figs. 26k, l). This seasonality of the Walker circulation is also depicted in the ERA40, NCEP2, and MERRA reanalyses (not shown).

A comparison of Figs. 25 and 26 indicates that seasonality of the Guinean subsidence east of 2°W and the Congo Walker basin circulation behave in a similar manner, especially during the boreal summer months of June–October with the subsidence and Walker circulation strength being strongest between July–September. Thus, the rest of the analysis presented below will focus on physically understanding the maintenance of the Congo basin Walker circulation and its relationship to subsidence over the Gulf of Guinea for the July–September period. Figures 27a–d show climatological July–September vertical cross sections of the zonal–omega wind components (vectors), and the meridional wind component (contours) averaged between for the ERAI, ERA40, NCEP2, and MERRA reanalyses. All of the reanalyses show the Congo basin Walker circulation with rising motions over the Congo basin centered at 20°E and extending from near the surface to the upper troposphere, easterly around 650 hPa between 0E–20°E, subsidence over the Gulf of Guinea that diverges at 2°W near the surface. Below 800 hPa from 2°W–25°E flow is predominantly westerly constituting the lower onshore branch of the Congo basin Walker circulation. Note near the surface over this region there is also a southerly component to the flow, but it is generally weaker in magnitude (e.g., up to 3 m s^{-1} in ERAI). The circulation is embedded within a large–scale incomplete circulation that rises over the

Congo basin, flows westward above 600 hPa, subsides over the Atlantic, but lacks the lower branch to complete the circulation.

While the basic structure of the Congo basin Walker circulation is captured by all of the reanalyses, there are still some differences among the datasets. For instance, the rising-branch is stronger in ERAI and ERA40 than in NCEP2 and MERRA. At 15°E and 700 hPa, the upward p-velocity is around 4×10^{-2} Pa s^{-1} in ERAI, ERA40, and NCEP2, while it is replaced with a downward p-velocity of about -1 Pa s^{-1} in the MERRA reanalysis.

Based upon Figs. 26 and 27 the boundaries of the Walker circulation during July–September can be defined. The up-branch is located between 15°E–25°E and 5°S–3°N over the Congo basin, while down-branch is between 2°W–8°E and 5°S–3°N over the Gulf of Guinea. Therefore unless mentioned, the Gulf of Guinea and Congo basin regions in this paper include 2°W–8°E; 5°S–3°N and 15°E–25°E; 5°S–3°N. The 650 hPa easterly and the surface westerly constitute the upper-branch and lower-branch (Figs. 27a–d).

The idea of there being a Walker circulation is not a new concept, as previous studies have suggested the possibilities of such a circulation (Vizy and Cook 2001; Lau and Yang 2002; Hastenrath 2006). This type of a zonal overturning circulation is only possible along the equator, because the Coriolis force is zero at the equator, and a purely zonal flow remains undeflected, as discussed in section 2.

In order to understand the cause of the westerly flow from the Guinean Gulf to Congo basin, which constitutes the lower-branch of the Congo basin Walker circulation, low-level geopotential heights and winds are examined. Figures 28a–d display the July–September climatological 925 hPa geopotential heights and winds from ERAI, ERA40,

NCEP2 and MERRA reanalyses, respectively. In all reanalyses geopotential heights are high over the equatorial Atlantic and low over the Congo basin, associated with zonal height gradient between the Gulf of Guinea and the Congo basin (e.g., heights approximately 20 gpm lower over the Congo basin than Gulf of Guinea). Associated with this zonal gradient is predominantly westerly flow in the vicinity of the equator from about 10°E–25°E.

To understand the maintenance of the Walker circulation, geopotential height gradient and its relationship with the low–level circulation, horizontal momentum equations are analyzed. The zonal (i.e., u–) and meridional (i.e., v–) components of the equation are as follows:

$$\frac{du}{dt} = -\frac{\partial \Phi}{\partial x} + fv + R_x \quad (1)$$

and

$$\frac{dv}{dt} = -\frac{\partial \Phi}{\partial y} - fu + R_y \ , \quad (2)$$

where u is the zonal wind and v is the meridional wind. In Eq. 1 (2), the total zonal (meridional) acceleration is balanced on the right–hand side by the acceleration due to the zonal (meridional) pressure gradient, the Coriolis acceleration component, where $f \equiv 2\,\Omega \sin\phi$ is the Coriolis parameter, Ω is the angular speed of rotation of the earth = 7.3×10^{-5} *rad/s* and ϕ is latitude, and the zonal (meridional) frictional acceleration, and the frictional acceleration terms R_x and R_y. Note R_x and R_y are calculated as residuals in the analysis, and therefore may contain errors due to the estimation of derivatives by finite differencing.

Figure 29 shows the 925 hPa July–September climatological value of each term in the horizontal momentum equations (Eqs. 1 and 2) from ERAI, ERA40, NCEP2, and MERRA reanalyses. Close to the equator, the total acceleration (top row) is small. Likewise at the equator the acceleration associated with the Coriolis force (3rd row) is small as *f* becomes zero at the equator. Thus, the primary balance occurs between the acceleration associated with the pressure gradient (2nd row) and the acceleration associated with the residual/friction term (4th row). The acceleration associated with the pressure gradient force is primarily eastward over Equatorial Africa with the strongest magnitudes occurring between 12°E and 18°E in the Congo basin. In contrast over the equatorial Atlantic the acceleration associated with the pressure gradient is much weaker. Values are greater over coastal inland than over the ocean. For example, this acceleration is about 6×10^{-5} m s^{-2} over the equatorial Gulf of Guinea, while it is 18×10^{-5} m s^{-2} over the Congo basin in the ERAI reanalysis (Fig. 29b). For the most part, the acceleration associated with the residual/friction term opposes the wind direction (Fig. 28), and has larger magnitude over land with complex topography, such as over western equatorial Africa.

In general, the low–level 925 hPa winds are directed eastward because of the pressure gradient force (Fig. 28). The eastward directed pressure gradient force is balanced by the residual term, friction, due to the basin topography (Figs. 29a–p). Analysis in Figs. 28 and 29 indicate the importance of the low–level pressure gradient force for maintaining the low–level westerly flow near the surface. To understand this pressure gradient, and the cause of the Congo basin rising motion, the underlying surface temperature is analyzed. Figure 30 shows the climatological July–September surface temperatures are for ERAI

(Fig. 30a), ERA40 (Fig. 30b), NCEP2 (Fig. 30c), and MERRA (Fig. 30d) reanalyses, and the CRUTS.3.21 1901–2012 observational dataset (Fig. 30e). Over the tropical eastern Atlantic a cold tongue of relatively cooler SSTs forms beginning in the late spring and reaching a minimum by late summer (Weingartner and Weisberg 1991; Hastenrath and Lamb 2004). This feature is represented in all of the reanalyses shown in Fig. 30 by the area of relatively cooler temperatures of 296 K between 5°S and the equator spanning from 10°W to the African coast. North of the equator, Atlantic SSTs are slightly warmer (i.e., up to 298–299 K). Generally, all of the reanalyses exhibit similar SST distributions over the Atlantic, which is not surprising since the reanalyses are typically forced with the observed SSTs. Over continental Africa surface temperatures vary among the different datasets, as they are predicted by the different land surface models included in reanalyses. For example, compared with the observed CRUTS3.21 surface temperatures, Congo basin temperatures are about 2 K cooler in the ERAI, ERA40, and NCEP2 reanalyses, while around 4 K warmer in the MERRA reanalysis (Fig. 30e). Despite these differences, the reanalyses generally indicate the existence of a surface temperature difference near the equator between the relatively cooler Gulf of Guinea and the relatively warmer Congo basin.

To better understand this Gulf of Guinea/ Congo basin low-level temperature difference, climatological monthly 925 hPa temperatures are area-averaged over the Gulf of Guinea (2°W–8°E; 5°S–3°N) and the Congo basin (15°E–25°E, 5°S–3°N) and compared to one another for each reanalysis. Figure 31a shows the monthly Congo basin (long–dashed) and the Gulf of Guinea (short dashed) surface temperatures and the

differences in the Congo basin and the Gulf of Guinea temperatures are shown in Fig. 31b. Note we choose to conduct this evaluation at 925 hPa to reduce the impact that differences in surface elevation may have on the comparison.

The results in Fig. 31a indicate that all reanalyses generally agree that the Congo basin 925 hPa temperatures are warmer than the Gulf of Guinea 925 hPa temperatures for all months. Furthermore, the seasonal variability over the annual cycle is much less over the Congo basin compared to over the Gulf of Guinea, as temperatures generally fluctuate by 2 K or less for the former compared to around 5–6 K for the latter .

In terms of the Congo basin and Gulf of Guinea temperature difference, it is positive year round, but relatively small (i.e., 3 K or less) from November – April for 3 of the 4 reanalyses (Fig. 31b). The exception, MERRA, has differences between 4 and 5.5 K during November–April. During the boreal summer months, the differences increase in May and June, peaking in July and August around 5 K in ERAI and NCEP2, 7.3 K in ERA40, and above 8 K in MERRA, after August the temperature difference begins to decrease as the cold upwelling weakens in the Gulf of Guinea. It is this low-level temperature difference that drives the Congo basin Walker circulation. The circulation appears when the temperature difference starts increasing in June, becomes well developed from July to September when the Congo basin/Gulf of Guinea temperature difference is largest, and as the eastern equatorial Atlantic cold tongue weakens, the Walker circulation starts weakening and disappears in the fall (Figs. 26, 31).

These results suggest that it is important to have an accurate representation of the Congo basin/ Gulf of Guinea low–level temperature difference/gradient because it drives

the Congo basin Walker circulation. Guinean temperatures are similar in the reanalyses, therefore, gradient differences are in large part determined by the Congo basin temperatures. Many potential factors can influence the low–level temperatures over land that can result in the inter–reanalysis spread shown in Fig. 31. One of the important factors is how each reanalysis treats the prediction of land surface conditions, however, understanding this is better left to the individual reanalysis groups that better understand the intricacies in the reanalysis modeling algorithm. A more basic factor is to evaluate the precipitation in the different reanalyses, since temperature and precipitation are tightly related. For this reason reanalyses precipitation are examined.

Climatological July–September precipitation rates are shown in Figure 32 for TRMM satellite rainfall estimates (Fig. 32a), and ERAI (Fig. 32b), ERA40 (Fig. 32c), NCEP2 (Fig. 32d), and MERRA (Fig. 32e) reanalyses. TRMM indicates a zonally oriented band of precipitation across Africa during July–September with maxima centered at 2°N; 18°W and 5°N; 8°E over the Cameroon highlands (Fig. 32a). Rainfall rates over the northern Democratic Republic of Congo (DRC) are over 7 mm day^{-1} and gradually decrease to about 3 mm day^{-1} around 5°S.

The zonally elongated band of rainfall with the two maxima is represented in each reanalysis (Figs. 32b–e), though the magnitudes of the maxima vary among the different resolution reanalyses. Over the DRC there are differences in the rainfall distributions among the reanalyses with MERRA, ERA40, and NCEP2 considerably drier than TRMM. Out of the four reanalyses, ERAI most realistically captures the July–September distribution of rainfall over DRC. This is consistent with the findings of Simmons et al.

(2010), who also report that precipitation field is generally better represented in ERAI compared to ERA40. Lower summertime rainfall rates, for example, in the MERRA reanalysis, are likely associated with increased surface heating due to a lack of convection, warmer than observed surface temperatures predicted over the DRC (e.g., Fig. 30b), and hence a larger low–level Congo basin/Gulf of Guinea temperature contrast (Fig. 31b).

To understand the returning branch of the Congo basin Walker circulation, climatological 600 hPa winds and temperature are examined (Fig. 33). 600 hPa is selected for analysis based on the results shown in Fig. 27 that indicate the return flow occurring between approximately 800–400 hPa. Flow is primarily easterly from the Congo basin to the Gulf of Guinea near the equator, and this easterly flow constitutes the returning-branch of the Congo basin Walker circulation. Magnitude of the easterly winds varies among the reanalyses (Figs. 33 a–d). For example, easterly wind over the Congo basin is around 10 m s^{-1} in the ERAI, ERA40, and NCEP2 reanalyses, but up to 16 m s^{-1} in the MERRA reanalysis. Similar to the lower-branch, the upper-returning-branch is driven by temperature gradient, but 600 hPa Gulf of Guinea is warmer than the Congo basin. The difference is positive, up to 0.06 K, in the ERAI, 0.27 K in the ERA40, 0.3 K in the NCEP2, and 0.35 K in the MERRA reanalyses.

Easterlies from the Congo basin to Gulf of Guinea at 600 hPa (Figs. 33 a–d), comprising the upper-returning-branch of the Walker circulation, subside around 2°W over the equatorial Atlantic. This subsiding motion, forming the down-branch of the circulation, diverges in the low-levels at 2°W, with flow to the east directed eastward completing the Congo basin Walker circulation (Figs. 27 a–d).

4.5.2 Variability of the Congo basin Walker circulation and its relationship with the West African precipitation

ERAI is utilized to examine the interannual variability of the Congo basin Walker circulation and its relationship with African rainfall. ERAI is selected because this reanalysis provided the most realistic representation of climatological July–September surface temperature and precipitation fields, as shown in section 4.1 (Figs. 30, 32).

To better understand the interannual variability of the Walker circulation in ERAI, the monthly vertical p-velocity anomalies (i.e., omega) are examined. Omega anomalies for July, August and September from 1979–2013 are calculated by subtracting the 1979–2013 climatological July, August and September omega at each level. This gives fields of omega anomalies for July, August and September from 1979–2013. Doing so removes the seasonal cycle from the time series to foster a better comparison over different months. Longer term trends in the reanalysis, such as those associated with global warming, are not removed, since our focus here is on understanding the mechanisms of the variability in the Walker circulation, and not on its cause.

To evaluate the relationship between the up-branch and down-branch of the Congo basin Walker circulation, an area-averaged 800 hPa vertical p-velocity index is created from the omega anomalies fields, as discussed in the preceding paragraph, for July, August, and September only. The averaging region utilized is 15°E–25°E, 5°S–3°N. This area corresponds to the rising-branch of the Walker circulation discussed earlier in section 4.1 (Fig. 26), while 800 hPa is chosen to be sufficiently above the topography of the region. The appropriate month of this index is correlated to the corresponding July, August, and

September 850 hPa vertical p-velocity. 850 hPa is selected because the Guinean subsidence is much larger in this level (see Fig. 27a).

Figure 34 shows the correlation between the Congo basin index and July, August, and September p–velocity field at 850 hPa for ERAI. Correlations are negative, up to 50% (significant at 95% level), in the equatorial Atlantic (5°S–3°N; 25°W–7°E), including the Gulf of Guinea. This implies that, when the rising motions over the Congo basin become stronger, subsidence over the Gulf of Guinea becomes strong, and vice versa. Correlations are positive and significant in the continental interior from 5°N-15°N centered around 10°N in the Sahel, while small negative correlations persist in the region to the north of 15°N, with a small region of significant correlations in the central Sahel over Chad. This suggests that a stronger rising motion over the Congo basin is associated with a stronger rising motion in the Sahel from 10°N-15°N, while it is associated with a stronger sinking motion in the region to the north of 15°N. Figure 35a shows the time series of the 800 hPa vertical p–velocity index for July, August, and September only from ERAI. This is used to explore the physics of the interannual variability. A negative value indicates a stronger rising motion. The index is mainly negative from 1979–1994. In 1995, there is an abrupt shift and the index is found to be primarily positive after 1994. For example, from 1979–1994, of 37 of the total 48 July, August, and September months are negative, while from 1995–2013, of 49 of the total 57 July, August, and September months are positive. This discontinuity is likely associated with various adjustments made to ERAI algorithm (e.g., new bias correction schemes, new moisture analysis and model physics schemes were used

to maintain consistency in observing systems) and data input (Simmons et al. 2007, Uppala et al. 2008; Dee and Uppala 2009; Kobayashi et al. 2009).

To remove this shift, the time series is divided into two parts, namely 1979–1994 and 1995–2013, and each part of the time series is scaled with its own climatology. For example, 1979–1994 July climatology is subtracted from 16 Julys from 1979–1994 to obtain the deseasonalised value for July, while and August and September are created in the like manner. Likewise the 1995–2013 July, August, and September months in a similar manner, but with utilizing the 1995–2013 climatology for the appropriate month.

Figure 35b shows the adjusted Congo basin index. The dashed lines correspond to ± 1 standard deviation. Positive and negative index values are now more evenly distributed over the time series and there is no evidence of a discontinuity in 1995. The index shown in Fig. 35b is used to detect individual months when the Congo basin vertical p-velocity index is strong and weak for the months of July, August, and September, hence identify particular months when the Congo basin Walker circulation is strong or weak. A strong Walker circulation month is defined as when the index value is less than -0.6 Pa s^{-1}, which corresponds to -1 standard deviation from the mean, while a weak Walker circulation month is defined as when the index is greater than +0.6 Pa s^{-1}, which corresponds to +1 standard deviation from the mean. Table 1 shows the months identified for each case. These months are then averaged together for each case to formulate composites when the Congo basin Walker circulation is particularly strong and weak. Figure 36a–c show July – September vertical cross–sections of the zonal and vertical components of the wind (streamlines) and vertical winds (shaded) averaged from 5°S–3°N for the reanalysis

climatology (Fig. 36a), as well as the weak (Fig. 36b), and strong (Fig. 36c) Congo basin Walker circulation composites. In the climatology, the Walker circulation extends from the surface to 700 hPa, where the upward p–velocity is about 5×10^{-2} Pa s^{-1} (Fig. 36a). In the weak composite, the rising-branch weakens, for example, the rising motion at 15°E/ 800 hPa is about 2×10^{-2} Pa s^{-1} weaker than in the climatology (Fig. 36b). In contrast, upward vertical motions are stronger than in the climatology by up to 2×10^{-2} Pa s^{-1} in the strong Walker circulation composite case (Fig. 36c). Up-branch in strong is significantly different from the weak composite at 95 % confidence level (not shown), meaning that a strong is different from a weak Walker circulation composite.

In order to understand the relationship between the Walker circulation and the West African precipitation, low-level circulation and moisture fields are analyzed in Figs. 36 d–f. Figure 36d shows climatological 800 hPa geopotential heights and moisture transport vectors for the July–September climatology. 800 hPa is selected to be consistent with the level used to create the two composite cases, as discussed earlier in Fig. 35. Associated with the North Atlantic sub-tropical high (Li et al. 2011), the largest heights are located off the coast of West Africa. The smallest height is located over the continent, east of 15°E. Moisture transport is predominantly westerly and southwesterly over the Guinean coast and the coastal inland over 0°E-15°E, 0°N-7°N. Transport vectors are primarily easterly to the south of the equator.

Figure 36e displays 800 hPa geopotential heights and moisture transport differences in the weak composite and the climatology, and differences in the strong composite and

climatology are shown in Fig. 36f. Geopotential heights are larger, up to 20 gpm, in the weak composite than in the climatology in the Sahel (25°W-20°E, 10°N-20°N), and the heights are up to -15 gpm lower over the Gulf and the Congo basin (Fig. 36e). Associated with these differences in the geopotential heights, easterly and northeasterly moisture transport anomalies develop over the Congo basin and the Sahel. Also, with the weakening of the west African Westerly jet (Pu and Cook, 2010), westerly moisture transport from the West African coast to the central Sahel lowers in the weak composite, as shown by the easterly moisture transport anomalies around 11°N. Associated with these, moisture level in the central Sahel becomes lower in the weak composite than in the climatology (not shown). In contrast to the weak, there is a general reduction, up to -25 gpm, of geopotential height over the Sahel and the Congo basin (~18°E, 5°S) in the strong composite. With these lowering of the heights, moisture transport to the Congo basin and the Sahel increases, as indicated by the westerly and southwesterly moisture transport anomalies over the western coast of West Africa and the Gulf (Fig. 36f), and in connection with these moisture transport anomalies, low-level, surface-800hPa, moisture in the central Sahel become greater than in the climatology (not shown). Though subsidence in the two composites were comparable and the differences were not visibly striking in the streamlines fields, the low-level flow fields show clear distinctions between the two composite cases (Figs. 36b, c, e, f). Fig. 36 indicates that moisture transport differ in the weak and strong cases, and the geopotential height anomalies are positive in the central Sahel in the weak composite, while they are negative in the strong composite. To understand these variations, the underlying

surface temperature differences, which are comparable to surface to 800 hPa mean temperature differences (not shown), are analyzed.

Figure 37a shows the surface temperature differences between the weak Walker circulation composite and climatology, and difference in the strong composite is shown in Fig. 37b. In both cases the Gulf of Guinea surface temperatures are warmer than the climatology by 0.05 – 0.30 K. Sahelian temperatures are generally warmer, up to 1.8 K, in the weak composite than in the climatology. These warmer temperature anomalies are associated with positive geopotential height differences in the weak composite in Fig. 36e. In the strong composite, Sahelian temperatures are up to -1.6 K cooler than in the climatology, and these are associated with negative differences in the heights (Fig. 36f). Over the Congo basin, temperatures are warmer (~ 0.2 K) in the weak composite anomaly. In contrast, surface is cooler (~ -0.4 K) in the strong composite anomaly. This is counterintuitive to Fig. 31, which concludes that the Walker circulation is driven by temperature gradient between the Gulf and the Congo basin and a strong composite anomaly is expected to be associated with positive temperature differences over the Congo basin. To understand these temperature anomalies, surface heat budget is analyzed. The net surface heating can be estimated as follows:

$$Q_{net} = Q_{sw} + Q_{lw} + Q_{sh} + Q_{lh} \quad (3)$$

where Q_{net} is the net surface heating, Q_{sw} is the net downward shortwave heating, Q_{lw} is the net upward longwave heating, Q_{sh} is the sensible heat flux, and Q_{lh} is the upward latent heat flux. A positive value denotes heat into the surface.

Figures 38 shows the individual terms of the July–September climatological surface heat budget [Eq. (3)] for ERAI. Solar (Fig. 38a) and longwave downward heating (Fig. 38b) contribute to warm the surface, while the longwave upward (Fig. 38c), latent heat flux (Fig. 38d) and sensible heat flux (Fig. 37e) terms act to cool the surface. Over the equatorial Gulf of Guinea, there is a net heat surplus of 60–110 W m^{-2} (Fig. 38f). This is because the cooler temperatures in the equatorial Atlantic cold tongue (e.g., 3°N–5°S, 10°W–10°E in Fig. 30a) are associated with relatively lower latent and sensible heat loss to the atmosphere, enabling ocean surface to warm due to the incoming solar radiation (Merle 1980; Houghton and Colin 1986; Hastenrath and Lamb 2004). In contrast, over the Congo basin, there is a net heat balance, and the balance is maintained by solar (~160 W m^{-2}), longwave downward (400 W m^{-2}) and upward (440 W m^{-2}) heating terms. Latent and sensible heating terms are relatively smaller. Similar to the Congo basin, there is a net balance of heat in the Sahel, and the magnitudes of the heating terms in the Sahel are comparable to that in the Congo basin.

Figure 39 shows the net solar heat flux (Fig. 39a), downward longwave (Fig. 39b), upward longwave (Fig. 39c), latent (Fig. 39d), sensible (Fig. 39e), and the net total surface (Fig. 39f) heating differences for the weak Walker circulation composite. Figures 39g–l are similar to Figs. 39a–f, but for the strong Walker circulation composite.

For the weak composite, net solar flux is larger than in the climatology by up to 6 W m^{-2} over the Congo basin and increases of 2 W m^{-2} occur along the coastal upwelling region, east of 5°E (Fig. 39a), where surface is warmer than in the climatology (Fig. 37a). These increases in the solar fluxes are largely compensated by lowering of the latent heat

flux (Fig. 39d). Solar flux is lower, up to 8 W m^{-2}, over the Guinean coast centered near 4°N. In general, solar flux constitutes the most changes in the net total surface heating (Fig. 39f). Sensible and longwave heating differences are small (Figs. 39b, c, and e). In the Sahel, there is a net increase, up to 14 W m^{-2}, in downward solar radiation. Also, the net latent heating term increases, up to 16 W m^{-2}, in the Sahel north of 15°N, and this term reduces, up to -4 W m^{-2}, in the southern Sahel from 10°N-15°N. This pattern is consistent with Fig. 34, which shows that in association with the weakening of the Congo basin rising, reduction in upward p-velocity occur over 10°N-15°N, while increases in upward p-velocity occur in the region to the north of 15°N, central Chad, for example. North of 15°N in the Sahel, increases of solar and latent heating are compensated by reduction in the longwave and sensible heating terms, and in the southern Sahel, from 10°N-15°N, reductions of latent, sensible and longwave terms act to balance increases of the net downward solar radiation.

In contrast to weak, solar flux lowers, up to 16 W m^{-2}, in the strong composite, and net changes in solar radiation constitutes most differences in the net total heating of the surface in the Congo basin and Sahel (Fig. 39g, l). Lower solar fluxes collocate with cooler temperatures in the basin and the Sahel (Fig. 37d). Reduction in solar heating is compensated by increases in the longwave, latent, and sensible heating (Fig. 39h, i, j, k). Latent heating increases, up to 6 Wm^{-2} in the southern Sahel, while reductions of up to -12 W m^{-2} occur in the northern Sahel. These reductions are compensated by increases in the upward longwave and sensible heating. In the Guinean Gulf, solar flux increases in most

regions except around equator, 5°E, where it lowers and the decrease is compensated by increases in the longwave downward radiation (Figs. 39g, h). Differences in the longwave upward and sensible heating are small (Figs. 39i, k). Latent heating decreases, up to 4 W m^{-2}, over the Gulf, and most decreases in the net total surface heating is associated with the latent heating term in the strong composite (Figs. 39j, l). In contrast to the weak, downward solar radiation reduces up to 10 W m^{-2} in the Sahel centered around 12°N. This reduction, is compensated by increases in the upward longwave, latent and sensible heating term.

In brief, most changes in the net total surface heat balance is associated with the solar heating. Net surface solar flux increases in the weak composite while decreases in the strong case in the Congo basin and the Sahel, especially the eastern parts of Sahel. There is lowering of the net total surface heating over the Gulf, and this is associated with the lowering of latent heating in the strong composite and combined latent and solar heating in the weak composite (Figs. 39a–l).

An investigation of cloud distributions helps relate surface heating patterns to surface temperature distributions. Most cloud is low–cloud (~ 80%, below 800 hPa) over the analysis region. Changes in the low–cloud cover are examined. The July–September mean low–cloud cover differences displayed in Fig. 40a is for the weak composite and climatology and Fig. 39b is for the strong composite and climatology. Cloud over land, including the Sahel and the Congo basin, and along the coastal upwelling region to the south of the equator reduces, up to -6%, in the weak composite (Fig. 40a), allowing relatively larger amounts of solar radiation to heat up the surface (Figs. 37a and 39a). Cloud cover increases up to 4% over the northern Guinean Gulf enabling lower amounts of solar

flux to the surface (Fig. 39a). Contrast to weak, cloud amounts increase generally over land, while decrease over ocean in the strong composite (Fig. 40b). Enhancement, up to 12 %, occur over the Congo basin and Sahel, permitting relatively smaller amounts of solar radiation and associated with this, the surface cools (Figs. 37b and 39g). Over the Gulf of Guinea, cloud amounts lower, up to -8%, allowing more incoming solar radiation to heat up the surface (Figs. 39d and 37b).

Difference between the weak and strong composites is in large part due to land surface heating. Associated with weak rising motion over the Congo basin, cloud cover reduces, allowing larger amounts of incoming solar radiation to increase the surface temperature in the weak composite. In contrast, cloud amounts increase generally over land, reducing the amount of incoming solar heat flux, and this cools the surface in the strong composite.

In summary, the Congo basin Walker circulation has a potential to modulate moisture distributions across West Africa. For example, a strong circulation is associated with larger moisture transport to Sahel and the Congo basin (Fig. 36c, f). Motivated by this, relationship, for example, the correlation, between the Walker circulation and rainfall across West Africa was explored. However, the Walker circulation does not show significant correlations with the observed precipitation. For instance, the Congo basin vertical p–velocity index from the ERAI (1.5° resolution) reanalysis, as created above (Fig. 35), does not correlate with precipitation from the TRMM (0.25° resolution) and GPCP (2.5° resolution) observations (not shown). Probable reasons include: differences in the spatial resolutions and methodology used in calculating the products, for example, the

ERAI reanalysis product is model dependent, and precipitation is satellite based, which depends upon methods used in the rainfall intensity calibration (Dee 2005; Huffman et al. 2009; Huffman and Bolvin 2013).

4.6. CONCLUSIONS

In this study, we properly document the Gulf of Guinea subsidence and identify a Congo basin Walker circulation, whose down-branch is associated with the presence of this subsidence. Inter–annual variability of the Walker circulation and its relationship with moisture and precipitation distributions across West Africa are explored.

The Guinean subsidence, develops in the low–level at the beginning of June, attains a maximum intensity of 6×10^{-2} Pa s^{-1} reaching as far as 5°N during the boreal summer (July to September), and dissipates in October. This subsidence is found to be associated with a complete zonal circulation, which has the same seasonality as that of the Guinean subsidence in the ERAI, ERA40, NCEP2 and MERRA reanalyses. The circulation is identified as a Congo basin Walker circulation. The Walker circulation comprises of: (1) a low–level westerly flow from the Gulf to the Congo basin, lower–branch, (2) rising of winds over the basin around 20°E, up-branch (3) easterly return flow from the basin to the Gulf of Guinea at 600 hPa, upper-branch, and (4) subsiding winds over the Gulf centered around 2°W, down-branch, with winds to the east flowing eastward to complete the circulation. This circulation reaches its maximum intensity in the summer from July to September, and Guinean subsidence is associated with the down-branch of the Walker circulation.

Analysis of momentum budget shows that the low-level flow is strongly ageostrophic, with small acceleration term and Coriolis term, which is zero at the equator, and large pressure gradient and friction terms. The eastward directed pressure gradient force drives the flow from the Gulf of Guinea toward the Congo basin, constituting the lower-branch of the Walker circulation. Pressure gradient term is larger over the Congo basin than Gulf of Guinea. Over the basin, it is comparable to the residual term, which opposes the wind direction. Residual is interpreted as friction, and is expected to be much larger over land with complex topography. Associated with this friction, winds converge and rise over the Congo basin forming the up–branch of the Walker circulation. Causes of the pressure gradient force are explored.

Analysis of surface temperature explains the eastward decreasing pressure gradient force that drives the Walker circulation and much of its seasonal variation. Temperature is up to -5 K lower in the Gulf of Guinea than in the Congo basin, in the ERAI reanalysis, for example, associated with this gradient, surface pressure is smaller in land than ocean.

Differences in the Gulf of Guinea/ Congo basin temperatures are primarily caused by differences in the land temperatures, which is model dependent, in the reanalyses. Land temperature and precipitation in the ERA40, NCEP2, and MERRA reanalyses are much warmer and drier than in the observations. The ERAI reanalysis is selected to understand variability of the Walker circulation based on its realistic representation of temperature and precipitation.

Correlation between Congo basin p–velocity index and the low–level vertical velocity field on inter–annual timescales, reveal that the Congo basin rising motion is significantly correlated, up to –0.5, with the Guinean subsidence in the ERAI reanalysis.

Based upon the strength of the up-branch, two composites are created to explore the Walker circulation's variability. Compared with the climatology, in strong composite, upward motion is up to 2×10^{-2} Pa s^{-1} greater, while it is about 1×10^{-2} Pa s^{-1} smaller in the weak composite. Underlying surface temperature differences in the composite cases and the climatology are explored to understand the variability. Congo basin is warmer, up to 0.2 K, in weak, while cooler, up to -0.4 K, in the strong composite, and in the Sahel, temperature is warmer, up to 1.8 K, in the weak composite, while cooler, up to -1.6 K, in the strong composite. This suggested that the differences in the two composite cases are primarily associated with the land temperature.

Analysis of the surface heat budget explains the above differences in surface temperature patterns. In the weak composite, warmer temperature anomalies in the Congo basin and Sahel are associated with increases in solar heating (~ 14 W m^{-2}), enabled by lowering of cloud amount (-8%) associated with the decreased convection, which is expected because the rising motion is weaker than in the climatology. On the contrary, in the strong composite, cooler surface temperature anomalies in the Congo basin and Sahel are associated with the decreased solar radiation flux (~ -10 W m^{-2}), supported by the increased cloud amount (~10%), and linked with increased convection due to stronger vertical velocity.

Examination of the low–level flows shows that the Walker circulation variability is related with moisture distributions across West Africa and the Congo basin. Along with the weakening of the circulation, Guinean subsidence becomes weak. This supports development of convection over the Gulf of Guinea, and moisture transport to the Sahel and Congo basin reduces, as discussed in Vizy and Cook (2001). In contrast, when the circulation is stronger, Guinean subsidence becomes stronger, and this inhibits convection over the Gulf of Guinea supporting northward and eastward moisture transport. Variability in the Walker circulation from the ERAI reanalysis, however, does not correlate significantly with TRMM and GPCP precipitation. The reason being differences in the data, which are from different sources. This highlights the importance of model output.

Realizing the important role of the Congo basin Walker circulation in moisture transport across West Africa and the Congo basin, further investigation of how the Walker circulation is related to the low–level moisture and precipitation distributions across the Congo basin on seasonal timescales in the state–of–the–art– regional and global climate models will be addressed in a subsequent paper.

4.7. ACKNOWLEDGEMENTS

Department of Energy (Award DE-FG02-10ER65092) is gratefully acknowledged for the financial support. The authors also acknowledge Dr. Edward K. Vizy, Dr. Julien Cretat, and Mr. Gang Zhang for their helpful discussions and suggestions.

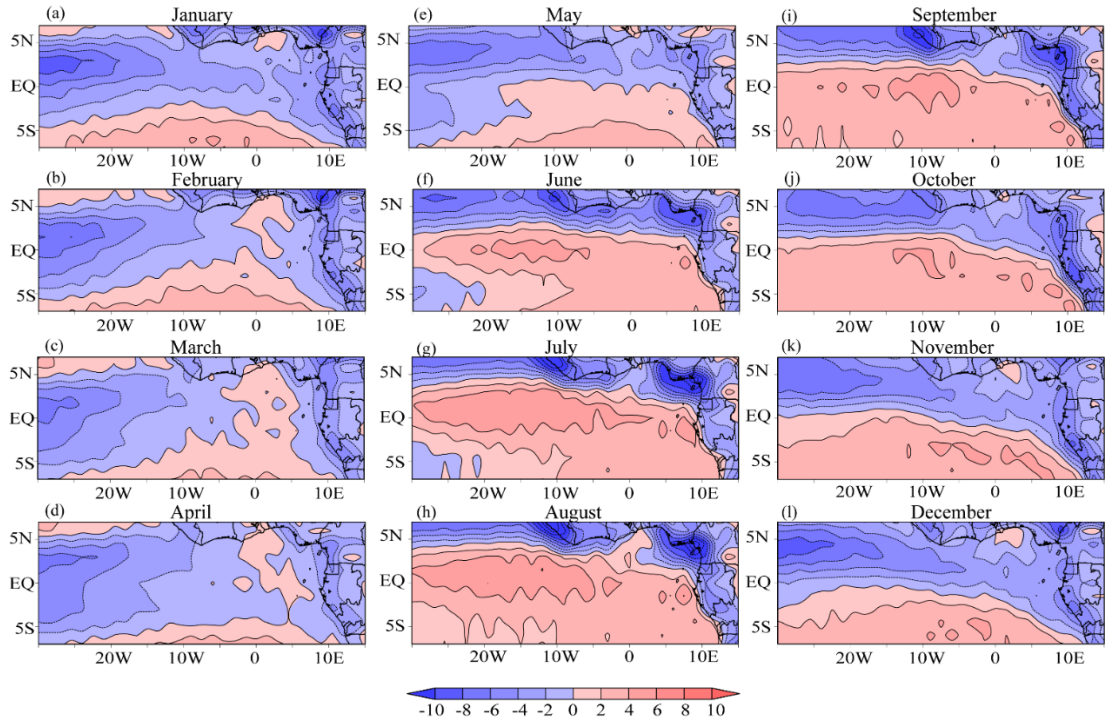

FIG. 25. ERAI climatological monthly 900 hPa p-velocity (omega; $\times 10^{2}$ Pa s^{-1}) for (a) January, (b) February, (c) March, (d) April, (e) May, (f) June, (g) July, (h) August, (i) September, (j) October, (k) November, and (l) December. Positive value indicates sinking motion.

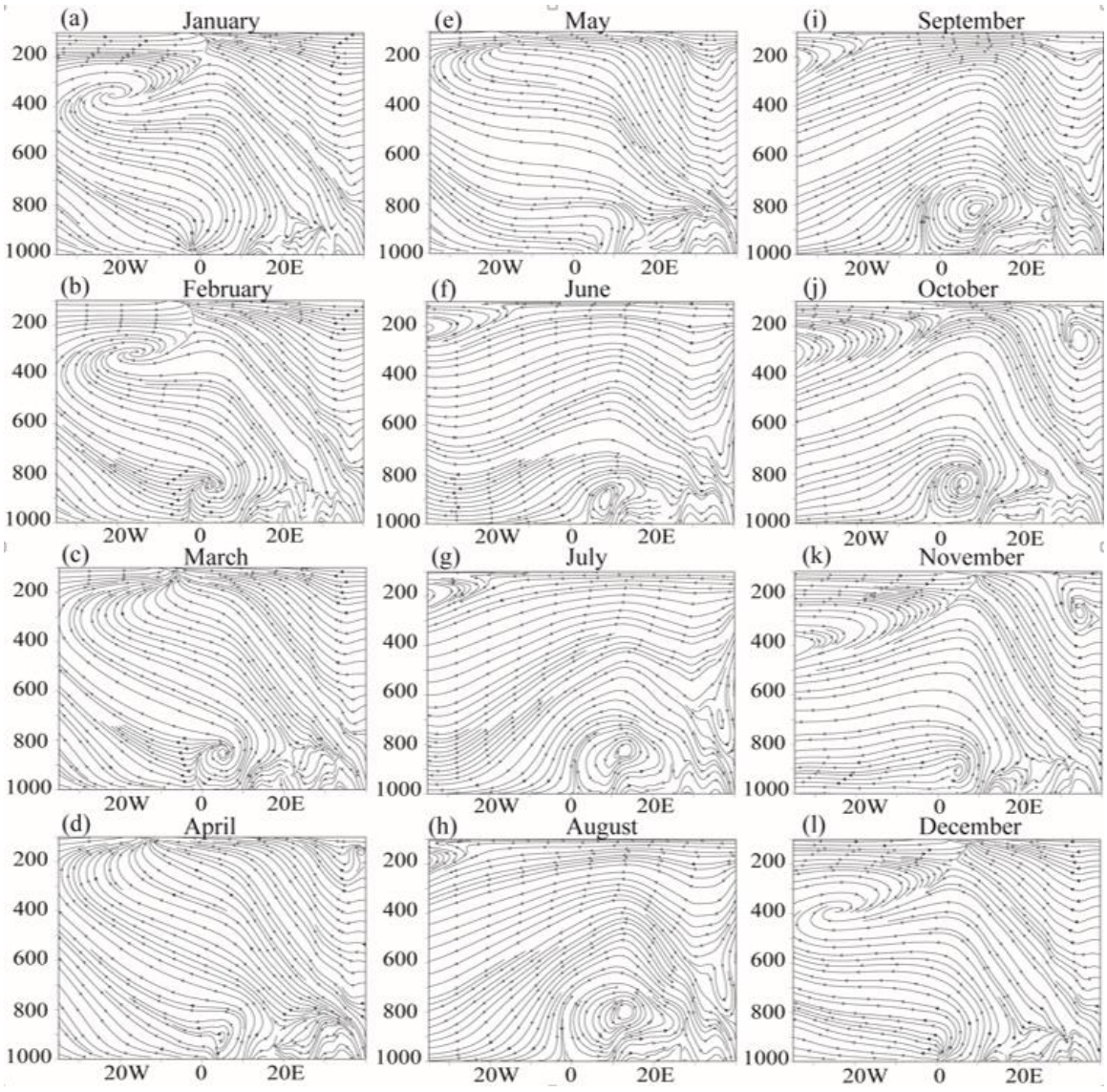

FIG. 26. ERAI climatological monthly longitude-height cross section of streamlines [u (m s^{-1}); - $\omega \times 10^{2}$ (Pa s^{-1})] averaged over 5°S-3°N for (a) January, (b) February, (c) March, (d) April, (e) May, (f) June, (g) July, (h) August, (i) September, (j) October, (k) November, and (l) December.

.

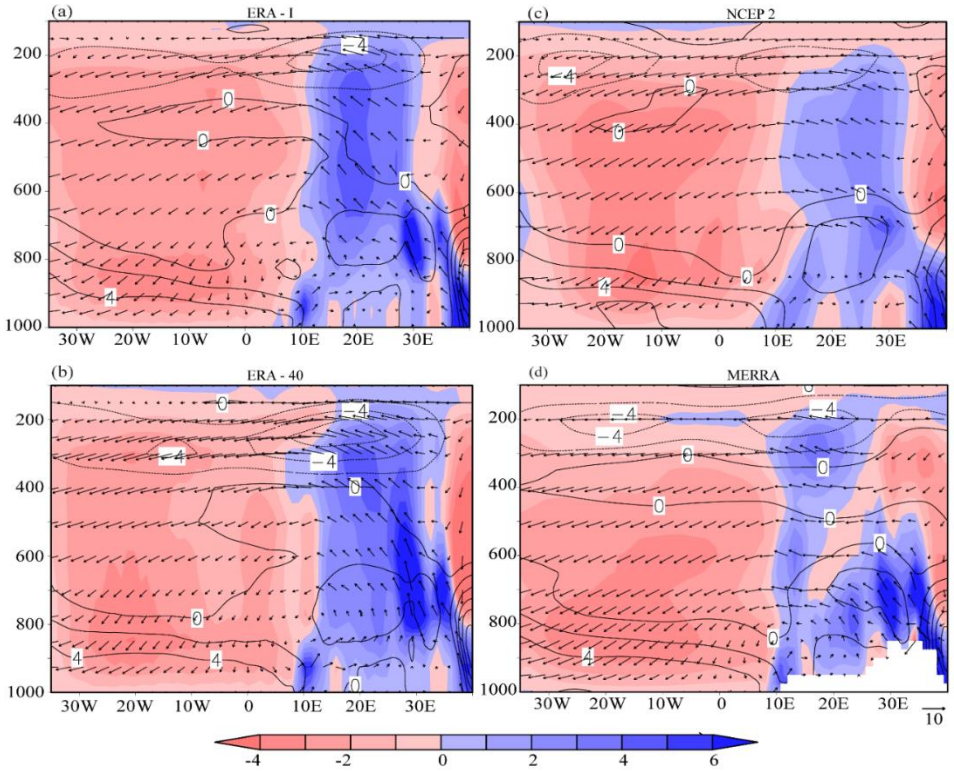

FIG. 27. Vertical cross section of zonal; vertical p-velocity [u (m s^{-1}); - $\omega \times 10^{2}$ (Pa s^{-1}), vectors], vertical p-velocity (-$\omega \times 10^{2}$, Pa s^{-1}, shading), and meridional winds (v, m s^{-1}, contour) averaged over 5°S-3°N for the July-September mean from the (a) ERAI, (b) ERA-40, (c) NCEP2, and (d) MERRA reanalyses climatologies. Positive shade indicates upward motion.

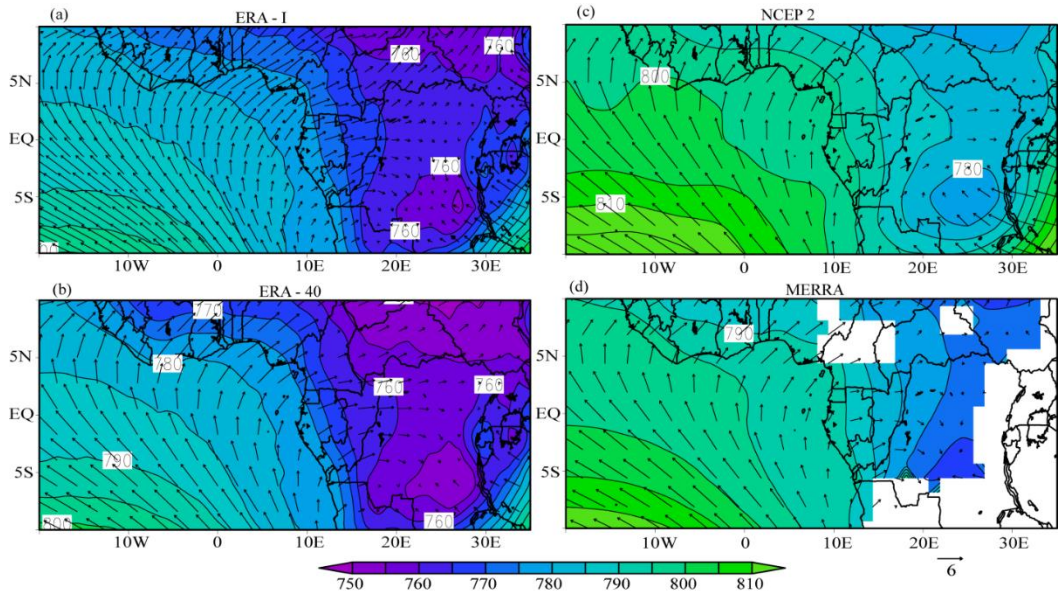

FIG. 28. July-September climatological 925-hPa geopotential heights (gpm) and winds (m s^{-1}) from the (a) ERAI, (b) ERA-40, (c) NCEP2, and (d) MERRA reanalyses.

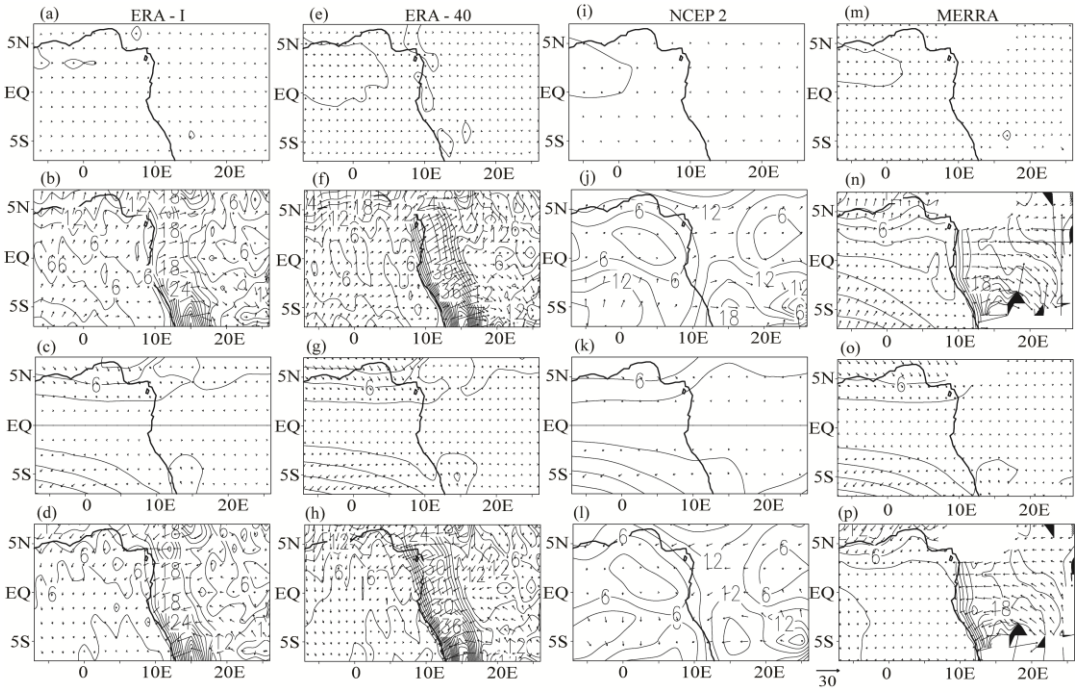

FIG. 29. Vectors showing combination of terms in equations (1) and (2), with contours displaying magnitudes (10^{-5} m s^{-2}) at 925-hPa for the July-September mean, as follows: (first-row) total acceleration, (second-row) acceleration associated with the geopotential height gradient, (third-row) acceleration associated with the Coriolis force, and (fourth-row) residual terms.

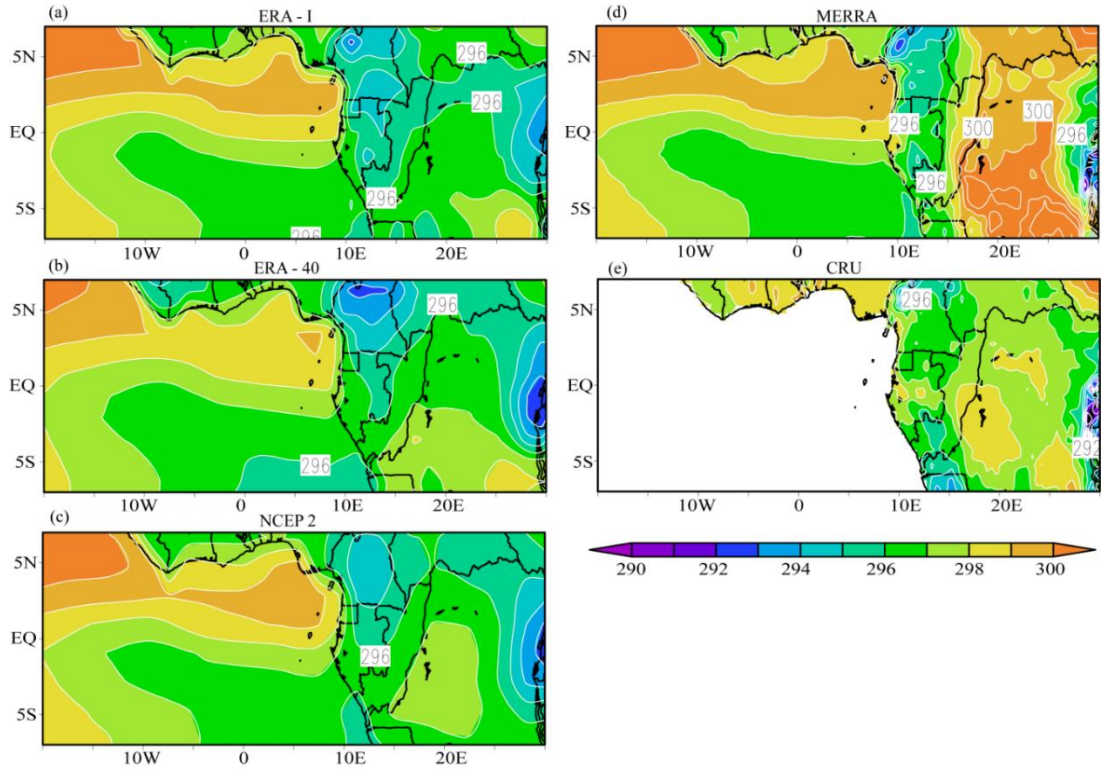

FIG. 30. Climatological July-September surface temperatures (K) from (a) ERAI, (b) ERA-40, (c) NCEP2, and (d) MERRA reanalyses and (e) CRUTS3.21 observations dataset. Contour interval is 1 K.

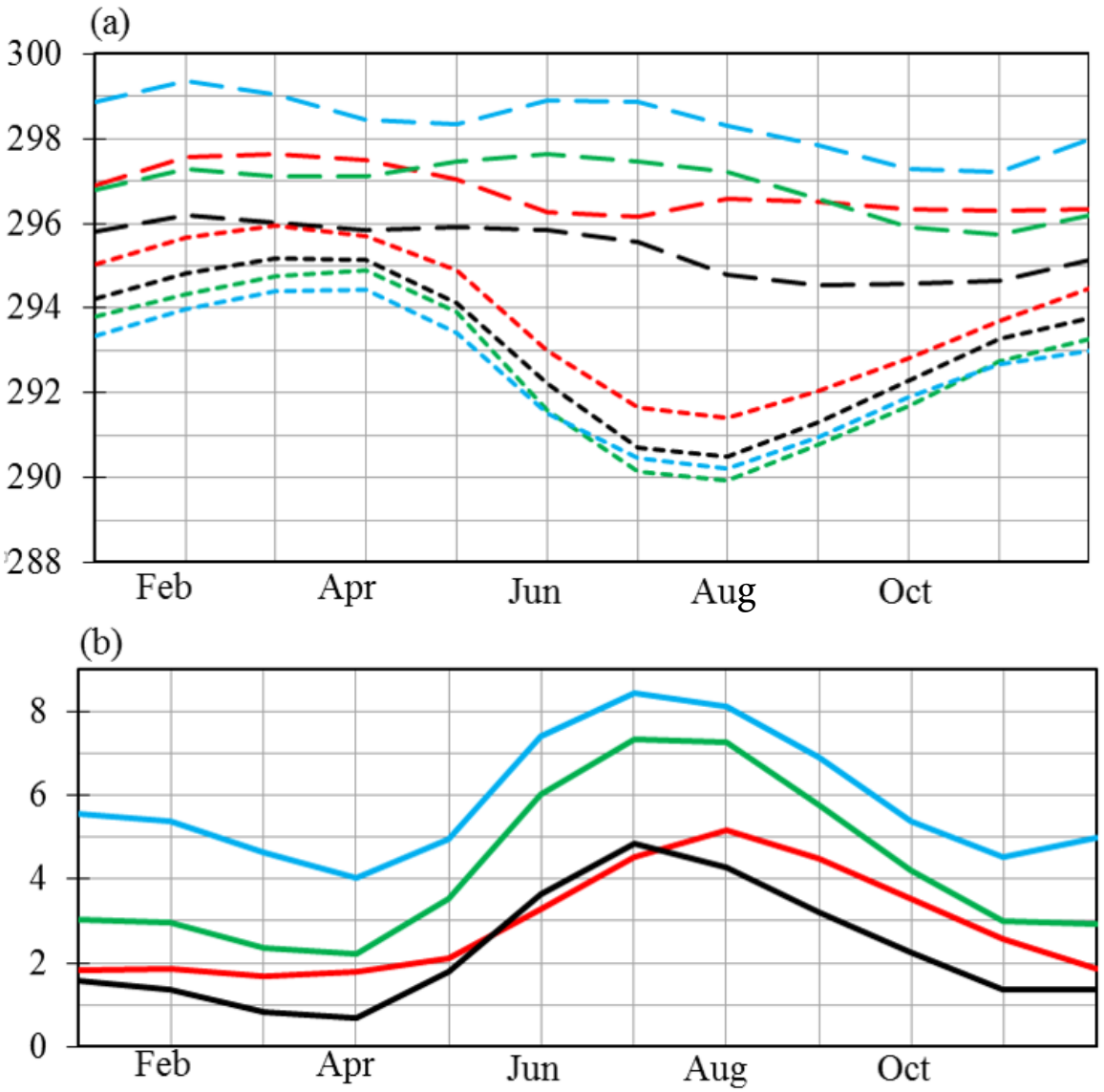

FIG. 31. (a) 925 hPa climatological monthly mean temperatures (K) in the Congo basin (15°E-25°E, 5°S-3°N, dashed), the Gulf of Guinea (2°W-8°E, 5°S-3°N, dotted), and their differences (solid) from the ERAI (black), ERA-40 (green), NCEP2 (red), and MERRA (blue) reanalyses. (b) 925 hPa climatological monthly mean temperature differences (K)

between the Congo basin and the Gulf of Guinea from the ERAI (black), ERA-40 (green), NCEP2 (red), and MERRA (blue) reanalyses.

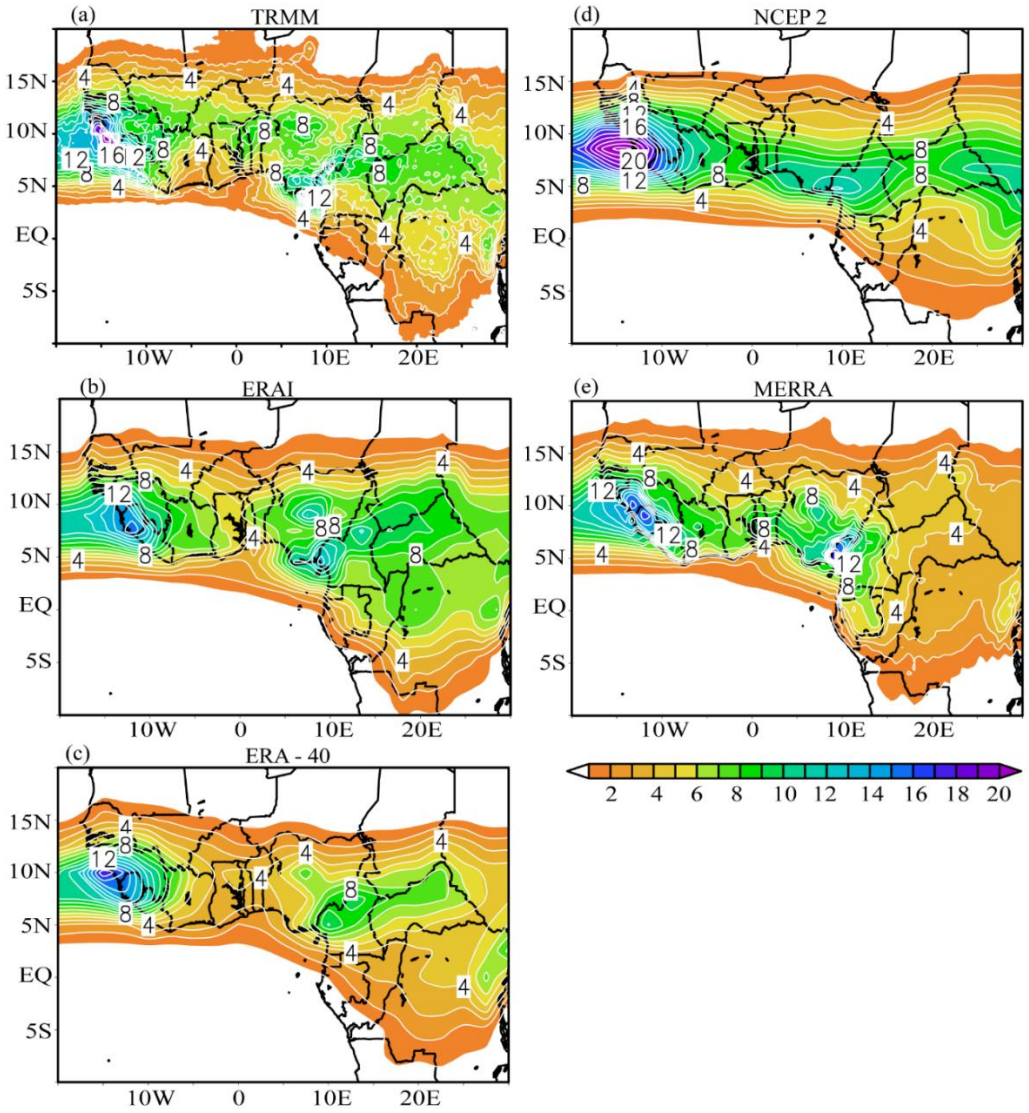

FIG. 32. Climatological July-September precipitation rates (mm day^{-1}) from the (a) TRMM 3B42V7 satellite derived rainfall estimates and the (b) ERAI, (c) ERA-40, (d) NCEP2, and (e) MERRA reanalyses.

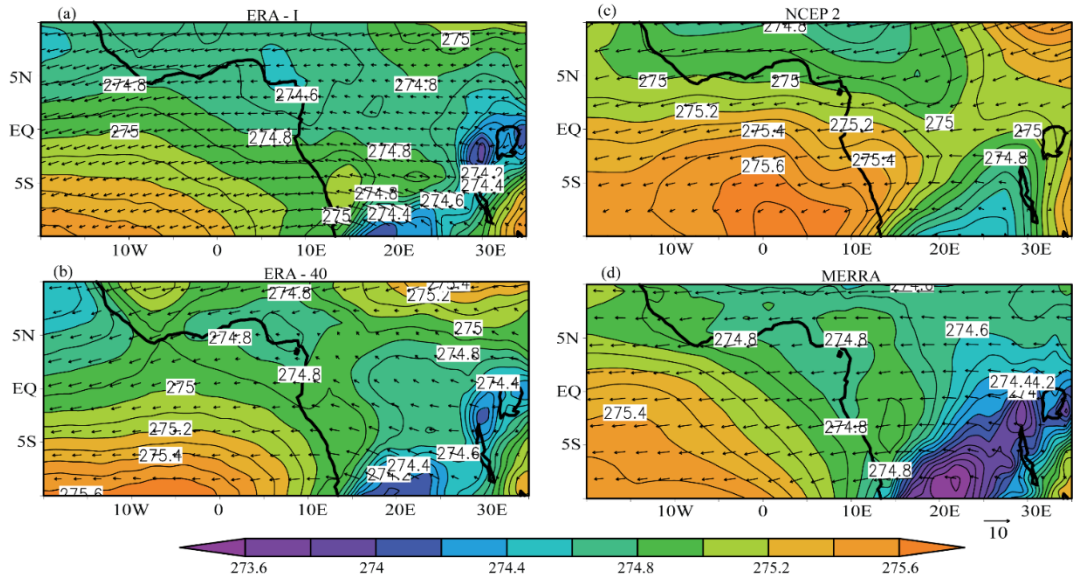

FIG. 33. Climatological July-September 600-hPa temperature (K, shaded) and horizontal wind (m s^{-1}, vectors) for the (a) ERAI, (b) ERA-40, (c) NCEP2, and (d) MERRA reanalyses. Contour interval is 1 gpm.

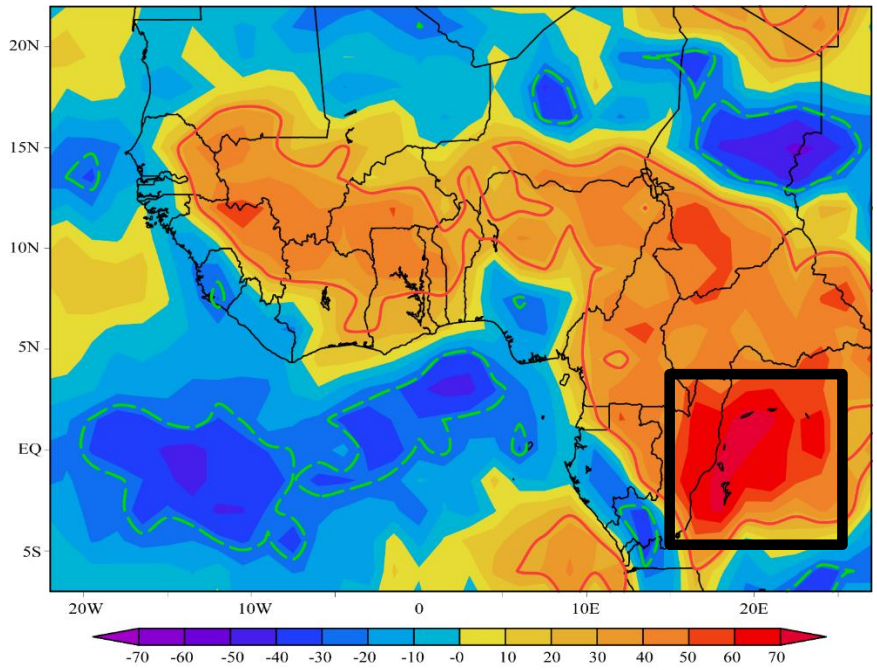

FIG. 34. Correlation between the ERA-I 800 hPa Congo basin Walker circulation index from 800 hPa and vertical p-velocity for July, August, and September. Correlation coefficients exceeding 95% confidence level are enclosed within red and green-dashed lines. Black polygon indicates the averaging region, 15°E-25°E,5°S-3°N.

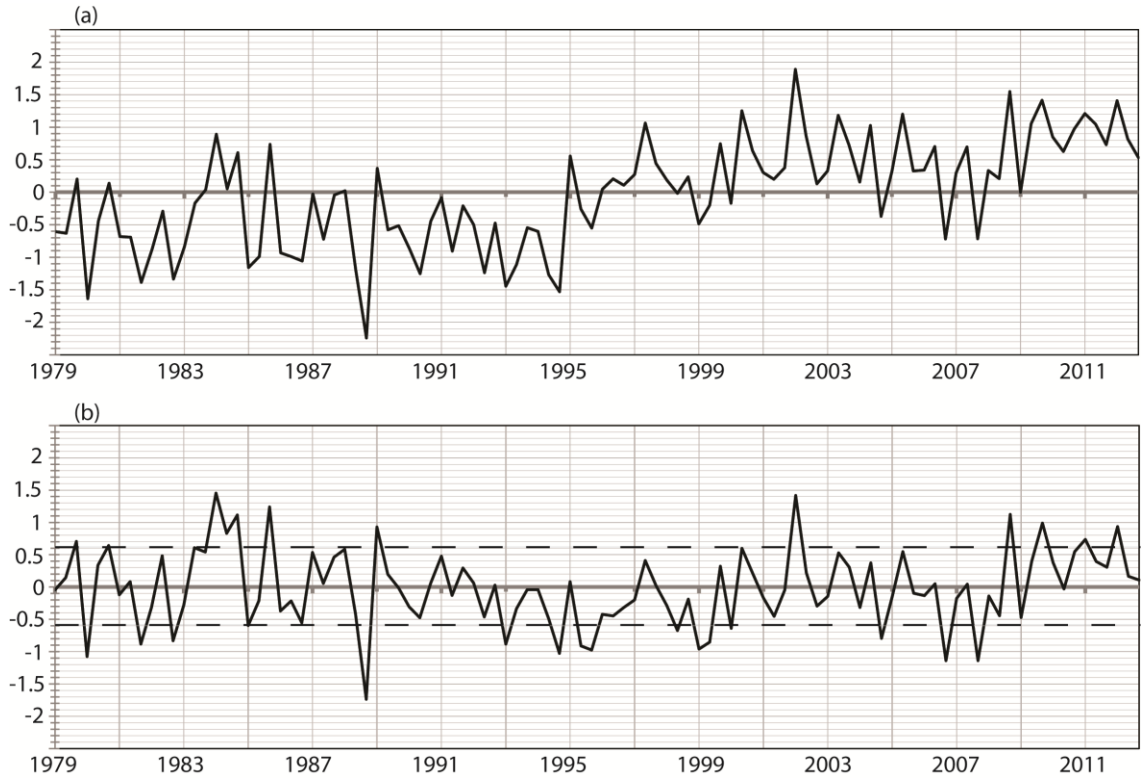

FIG. 35. (a) 800 hPa average 15°E-25°E and 5°S-3°N vertical p-velocity ($\times 10^2$ Pa/s) differences in July, August, and September and their climatologies from the 1979-2013 ERAI reanalysis. (b) Same as in (a), but the vertical p-velocity values before 1994 are differenced from 1979-1994 mean, and the values after 1995 are differenced from 1995-2013 mean. The dashed lines in (b) indicate ±1 S.D.

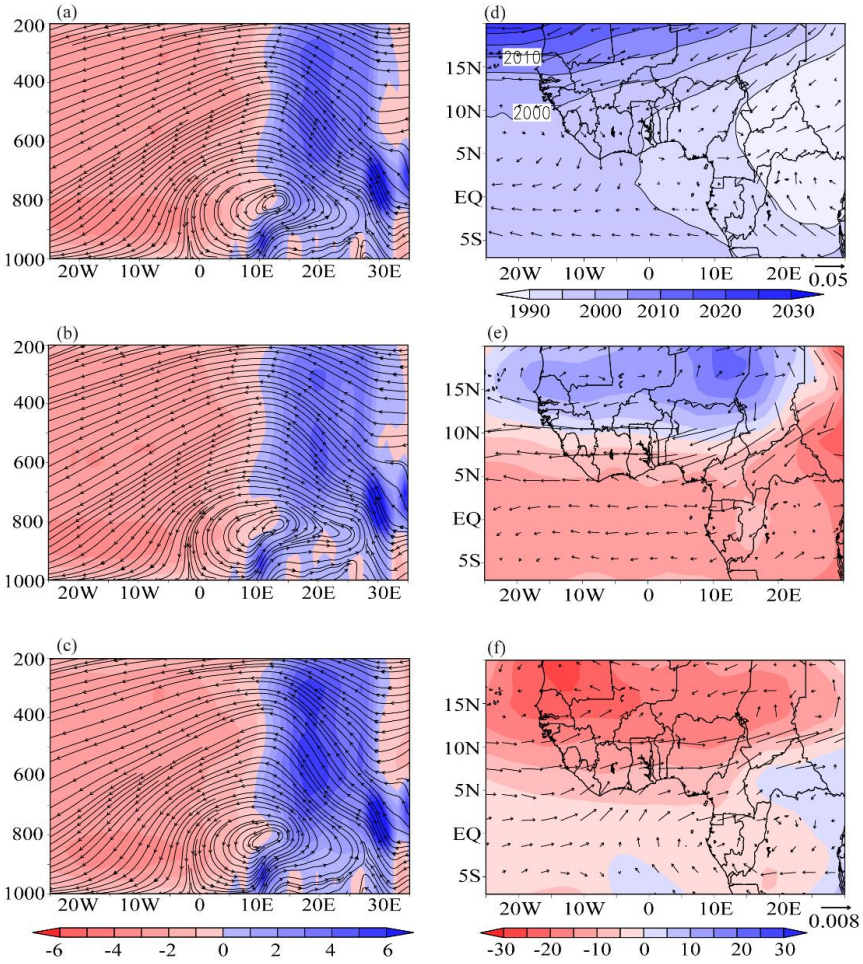

FIG. 36. ERAI longitude-height cross section of streamlines [u (m s^{-1}); - ω × 10^{2} (Pa s^{-1})] and vertical winds (× 10^{2} Pa s^{--1}, shaded), averaged over 5°S-3°N from the (a) July – September climatology, and the (b) weak and (c) strong Congo basin Walker circulation composites. Positive shading (i.e., blue colors) indicate upward vertical motion. Also, (d) ERAI July-September climatological 800 hPa moisture transport ($q.\boldsymbol{u}$, vector) and geopotential heights (shaded). (e) Moisture transport and geopotential height differences in the weak composite and the climatology. (f) is same as in (e), but for the strong composite. Geopotential height is in gpm, and moisture transport is in kg-m/kg-s.

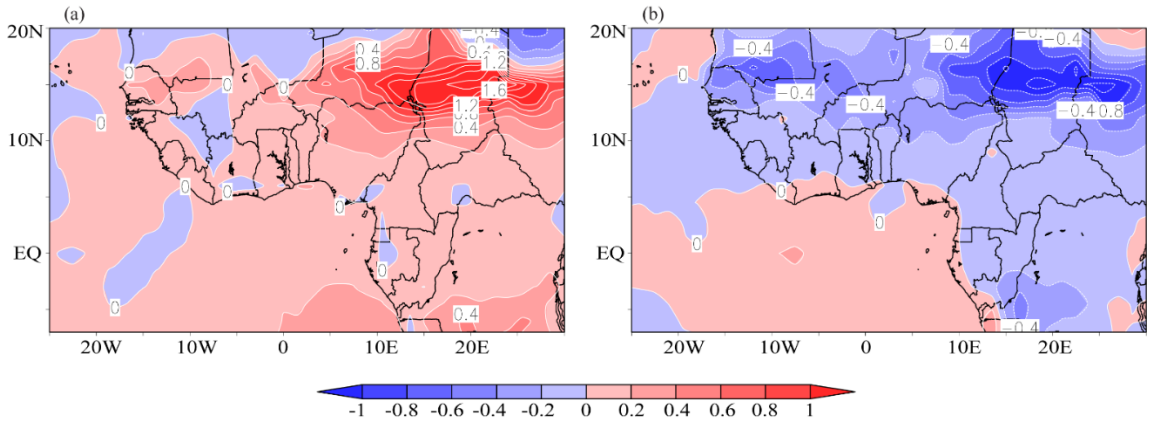

FIG. 37. Surface temperature difference (K) between the (a) weak Congo basin Walker circulation composite and climatology-, and (b) strong Congo basin Walker circulation composite and climatology. Contour interval is 0.2 K.

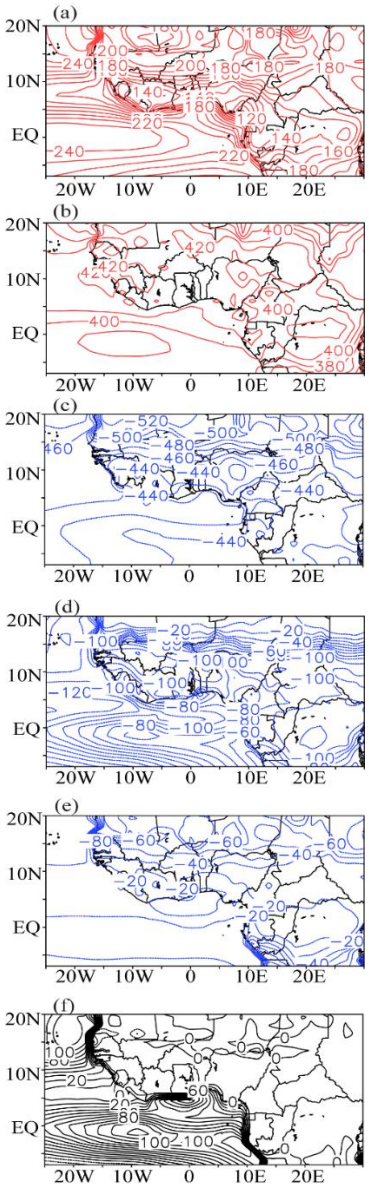

FIG. 38. ERAI July-September climatological surface (a) net solar radiation, (b) downward long-wave radiation, (c) upward long-wave radiation, (d) net latent, (e) net sensible heat flux, and (f) the net total surface radiation. Red contour, positive value, indicates heat into the surface, while blue contour, negative value, indicates heat out of the surface. Units are W m^{-2}.

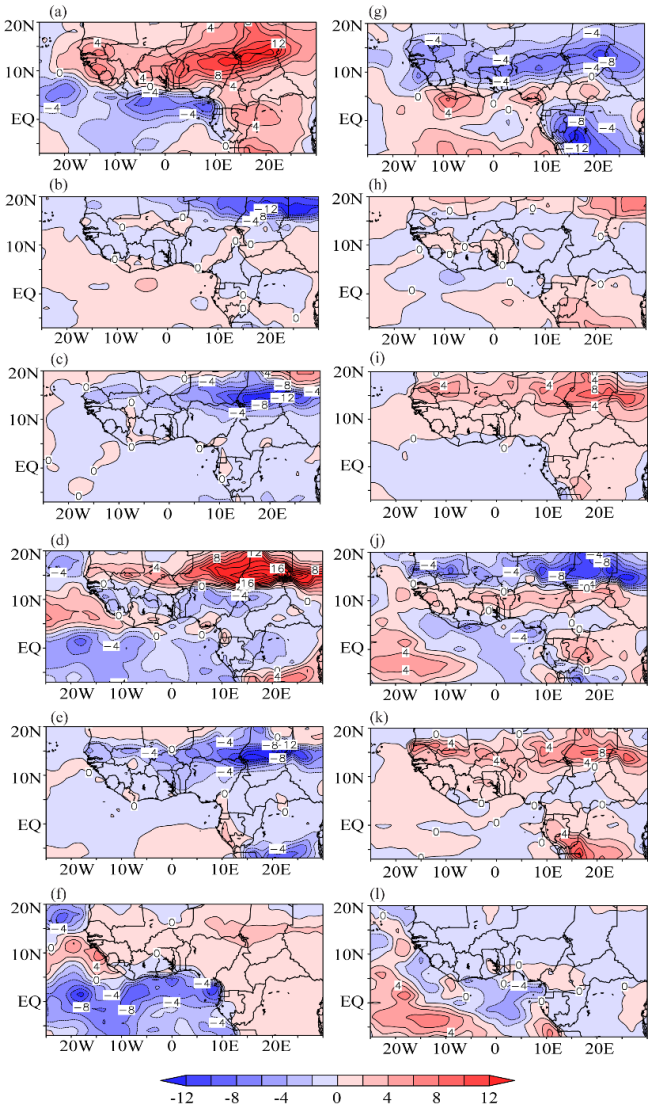

FIG. 39. (a) Net solar radiation on the surface, (b) downward long-wave radiation, (c) upward long-wave radiation, (d) net latent, (e) net sensible heat flux, and (f) the net total surface radiation differences in the weak composite and the July-September mean from the ERAI climatology. (g) is same as in (a), (h) is same as in (b), and (i) is same as in (c), (j) is same as in (d), (k) is same as in (e), and (l) is same as in (f), but for the strong composite. Units are W m^{-2}.

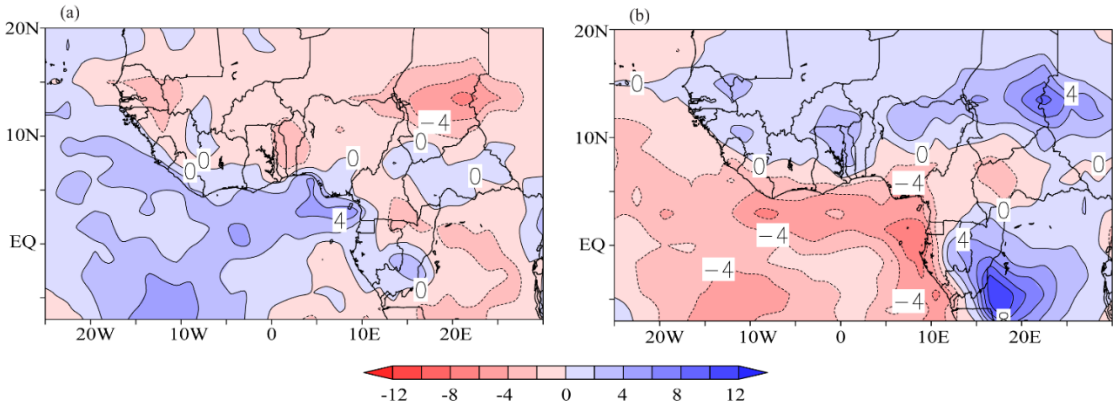

FIG. 40. (a) Low cloud cover (%) differences in the weak composite and the July-September mean from the ERAI (1979-2012) climatology. (b) is same as in (a), but for the strong composite. Contour interval is 2%.

Table 1. Summary of weak and strong Congo basin Walker circulation months

S. N.	Weak	Strong
1.	September, 1979	July, 1980
2.	September, 1980	September, 1981
3.	August, 1983	September, 1982
4.	July, 1984	September, 1988
5.	August, 1984	July, 1993
6.	September, 1984	September, 1994
7.	September, 1985	August, 1995
8.	July, 1989	September, 1995
9.	August, 2000	August, 1998
10.	July, 2002	July, 1999
11.	September, 2008	August, 1999
12.	September, 2009	July, 2000
13.	September, 2010	July, 2001
14.	July, 2011	September, 2004
15.	July, 2012	September, 2006
16.		September, 2007

Chapter 5: General Conclusions

This dissertation primarily focuses on understanding the impacts of global warming to rainfall changes over West Africa and the United States. Also, understanding of the presence of a seasonal scale subsidence in the Gulf of Guinea in the eastern equatorial Atlantic is another focus. For understanding the impact s of global warming on rainfall across West Africa and the United States, I use a regional climate model, WRF (Weather Research and Forecasting, version 3.1.1) simulations, whereas only the observations (TRMM, GPCP, and CRU) and reanalyses (NCEP2, ERAI, ERA40, and MERRA) were used to understand the presence of subsidence in the eastern equatorial Atlantic.

In addition to the first and the fifth chapters on general introduction and conclusions, this dissertation comprises of three main chapters: (1) understanding the nonlinear response of Sahelian rainfall to Atlantic warming, this constitutes the second chapter, (2) understanding projections of increased precipitation intensity in the U.S. east of the Rockies, which is the third chapter, and (3) identification of a Congo basin Walker circulation, and this forms the fourth chapter. These three main chapters correspond to three independent manuscripts. Conclusions from those chapters are summarized below.

In the second chapter, a regional climate model forced with uniform Atlantic warming ranging from 1 K to 4 K is used to contribute to our physical understanding of how the West African monsoon will respond under global warming. Atlantic Ocean is selected because of the known sensitivity of the West African monsoon to Atlantic SSTAs.

With 1 K and 1.5 K warming of the Atlantic, rainfall rates increase by 30-50% over most of West Africa. With warming of 2 K, Sahel rainfall reduces by about 18%. This nonlinear response of the Sahelian rainfall to Atlantic warming is explored in the second chapter.

Warming less than 2 K in the Atlantic Ocean is associated with decreases in low-level geopotential heights in the Gulf of Guinea causing reductions in the large-scale meridional geopotential height gradients across West Africa. Easterly wind anomalies develop in the Sahel and the southerly monsoon flow onto the Guinean coast is not diverted strongly to the east. The Guinean moisture penetrate farther north and leads to precipitation increases. In contrast, above 2 K warming, the large-scale meridional height gradient decreases further, and the easterly wind anomalies become stronger and these easterly anomalies reverse the westerly flow over Sahel. Moist static energy analysis reveals that the atmosphere is unstable in 1 K and 1.5 K due to moisture profile, while the atmospheric moisture decreases and the moisture profiles become stable above 2 K warming simulations.

Direct applications of these results to global warming study is limited. This is because the impact of various other factors, for example, rising CO_2 levels, Indian and Pacific Ocean warming to rainfall distributions across West Africa are not taken into consideration. However, it is important to understand how changes in one physical element, for example, Atlantic SST, which is an integral part of the West African climate, could affect the monsoon system under global warming. Since the goal of this study is to

contribute to understanding the process by which the Atlantic warming affects rainfall distributions across West Africa, this study contributes to that goal.

Climate models predict increases in precipitation under global warming. This understanding is founded on the Clausius–Clapeyron relation, which shows that the saturation mixing ratio increases at the rate of 7% for every 1 K rise in the surface temperature, and the fact that the relative humidity remains constant under global warming. Observations and modelling studies have shown that precipitation and atmospheric moisture often follow the theoretical prediction from the Clausius–Clapeyron relation on a global scale. In the third chapter of this dissertation, predicted precipitation from the Clausius–Clapeyron relation is compared with the modeled precipitation for the mid-21st century on the regional and seasonal space scales. The reason for departure of the model from the theory is explored. This study uses regional model simulations from Patricola and Cook (2013), and the study area is North America.

Since most increases in precipitation in the analysis region, east of the Rockies, are associated with the convective precipitation, focus is laid on understanding changes in this component of precipitation. Modeled convective precipitation increases up to 30%/K in the future and the increases follow the theoretical predictions in the central Midwest in the spring and fall, while reductions of about -8%/K occur in the summer and the theoretical predictions fail. Similar to the convective precipitation in the central Midwest, vertically-integrated specific humidity and 2-m specific humidity increases follow the Clausius-Clapeyron relation (7%/K) in the spring and fall, while the increases fall below the theoretical predictions in the summer. These differences between the theory and model are

associated with the soil moisture distributions. Soil moisture increases up to 15% in the spring and fall, while reductions of about -15% occur in the summer. Associated with soil moisture increases, increases in convective rainfall intensities agree roughly with the theoretical predictions in the spring and fall. In contrast, associated with the decreases in soil moisture, surface becomes warmer, and the warming leads to enhanced dry convection but there is no precipitation increase, and the theoretical prediction based on the Clausius–Clapeyron equation fails.

In the fourth chapter, a Walker circulation is identified over the Gulf of Guinea and the Congo basin. There is a seasonal-scale subsidence over the Gulf of Guinea. In investigating the cause of this subsidence, a Walker circulation over the Gulf of Guinea and the Congo basin is identified in the reanalyses (ERAI, ERA40, NCEP2, and MERRA). The physics of the Walker circulation and its relationship with moisture and rainfall distribution across West Africa are explored.

There is atmospheric upward motion over the Gulf from January through May. The upward p-velocity in May is replaced with downward p-velocity in June. The downward wind attains maximum velocity of about 6×10^{-2} Pa s^{-1} from July-September and becomes weak in October. This subsidence is associated with a Walker circulation. The circulation has up-branch over the Congo basin around 20°E and upper returning branch around 600 hPa. The subsiding winds over the Gulf of Guinea forms the down-branch, and the subsiding winds to the east of 2°W flow eastward forming the lower-branch to complete the circulation. Analysis of surface temperature reveals that the Walker circulation is driven by surface temperature difference between the Gulf of Guinea and the Congo basin.

Associated with the formation of Atlantic cold tongue, temperature is up to 4 K lower in the Gulf than in the Congo basin during the boreal summer season.

Based upon its realistic representation of surface temperature and precipitation, ERAI is selected for exploring the variability of the Walker circulation and its relationship with rainfall and moisture distributions across West Africa. As the Walker circulation becomes strong, subsidence over the Gulf increases and this supports increased northward transport of moisture. In contrast, with the weakening of the Walker circulation, northward moisture transport reduces supporting development of convection over the Gulf, as discussed in Vizy and Cook (2001).

The Walker circulation in the ERAI reanalysis does not correlate significantly with the precipitation in the TRMM observations. The reason being differences in the data, which are from different sources. For this reason and realizing the important role of the Walker circulation in West African moisture transport, further investigation of how the Walker circulation is related with West African precipitation will be addressed in a subsequent paper by using climate model simulations.

References

Adler, R. F., G. Gu, J.-J. Wang, G. J. Huffman, S. Curtis, and D. T. Bolvin, 2008: Relationships between global precipitation and surface temperature on inter-annual and longer time scales (1979 – 2006), *J. Geophys. Res.,* **113,** D22104, doi:10.1029/2008JD010536.

Adler, R. F., G. J. Huffman, A. Chang, R. Ferraro, P. Xie, J. Janowiak, B. Rudolf, U. Schneider, S. Curtis, D. Bolvin, A. Gruber, J. Susskind, P. Arkin, and E. Nelkin, 2003: The Version–2 Global Precipitation Climatology Project (GPCP) monthly precipitation analysis (1979–present). *J. Hydrometeorol.,* **4,** 1147–1167.

Allan, R. P., and B. G. Liepert, 2010: Anticipated changes in the global atmospheric water cycle. *Environ. Res. Lett.,* **5,** 025201, doi:10.1088/1748-9326/5/2/025201.

Alley, R. B., 2000: The Younger-Dryas cold interval as viewed from central Greenland. *Quat. Sci. Rev.*, **19,** 213–226.

Biasutti, M., I. M. Held, A. H. Sobel, and A. Giannini, 2008: SST forcings and Sahel rainfall variability in simulations of the twentieth and twenty–first centuries. *J. Climate*, **21**, 3471–3486.

Biasutti, M., and A. Giannini, 2006: Robust Sahel drying in response to late 20th century forcings. *Geophys. Res. Lett.,* **33,** L11706, doi: 10.1029/2006GL026067.

Caesar J. and J. A. Lowe, 2012: Comparing the impacts of mitigation versus non-intervention scenarios on future temperature and precipitation extremes in the HadGEM2 climate model. *J Geophys Res* **117:** D15109. doi:10.1029/2012JD017.

Camberlin, P., S. Janicot, and I. Poccard, 2001: Seasonality and atmospheric dynamics of the teleconnections between African rainfall and tropical ocean surface temperature: Atlantic vs. ENSO. *Int. J. Climatol.,* **21,** 973–1005.

Chen X. F., X. M. Chuai, L. Y. Yang, and H. Y. Zhao, 2012: Climatic warming and overgrazing induced the high concentration of organic matter in Lake Hulun, a large shallow eutrophic steppe lake in northern China. *Sci. Total Environ,* **431**, 332–338.

Chen, F., and J. Dudhia, 2001: Coupling an advanced land surface – hydrology model with the Penn State–NCAR MM5 modeling system. Part I: Model implementation and sensitivity. *Mon. Wea. Rev.,* **129,** 569–585.

Chou, C., J. D. Neelin, C. -A. Chen, and J.-Y. Tu, 2009: Evaluating the ‘‘rich get-richer’’ mechanism in tropical precipitation change under global warming. *J. Climate,* **22,** 1982–2005.

Collins, W. D., and Coauthors, 2004: Description of the NCAR Community Atmosphere Model (CAM3). Tech. Rep. NCAR/TN- 464STR, National Center for Atmospheric Research, Boulder, CO, 226 pp.

Cook, K. H., G. A. Meehl, and J. M. Arblaster, 2012: Monsoon regimes and processes in CCSM4, Part 2: African and American monsoon systems. *J. Climate,* **25**, 2609-2621.

Cook, K. H., and E. K. Vizy 2008: Effects of twenty-first-century climate change on the Amazon rain forest. *J. Climate,* **21,** 542-560.

Cook, K. H., 2008: Climate science: The mysteries of Sahel droughts. *Nat. Geosci.,* **1,** 647–648.

Cook, K. H., and E. K. Vizy, 2006: Coupled model simulations of the West African Monsoon System: Twentieth– and twenty–first century simulations. *J. Climate,* **19,** 3681–3703.

Cook, K. H., 1999: Generation of the African easterly jet and its role in determining West African precipitation. *J. Climate,* **12,** 1165–1184.

Cook, K. H., 1997: Large–scale atmospheric dynamics and Sahelian precipitation. *J. Climate,* **10,** 1137–1152.

Cubasch, U., G. A. Meehl, G. J. Boer, R. J. Stouffer,M. Dix, A. Noda, C. A. Senior, S. Raper, and K. S. Yap, 2001: Projections of future climate change, in Climate Change 2001: The Scientific Basis, edited by J. T. Houghton et al., pp. 525–582, Cambridge Univ. Press, New York.

Dai, A., 2006: Recent climatology, variability, and trends in global surface humidity. *J. Climate,* **19,** 3589–3606.

Dee, D., and Coauthors, 2011: The ERA-Interim reanalysis: Configuration and performance of the data assimilation system. *Quart. J. Roy. Meteor. Soc.,* **137,** 553–597.

Dee, D., and S. Uppala, 2009: Variational bias correction of satellite radiance data in the ERA–Interim reanalysis. *Quart. J. Roy. Meteor. Soc.,* **135,** 1830–1841.

Dee, D., 2005: Bias and data assimilation. *Quart. J. Roy. Meteor. Soc.,* **131,** 3323–3343.

deMenocal, P., J. Ortiz, T. Guilderson, J. Adkins, M. Sarnthein, L. Baker, and M. Yarusinsky, 2000: Abrupt onset and termination of the African Humid Period:

Rapid climate responses to gradual insolation forcing. *Quat. Sci. Rev*., **19,** 347–361.

Diem, J. E., and D. P. Brown, 2003: Anthropogenic impacts on summer precipitation in central Arizona, U.S.A. *Prof. Geogr.*, **55** (3), 343–355.

Dominguez, F., E. Rivera, D. P. Lettenmaier, and C. L. Castro, 2012: Changes in winter precipitation extremes for the western United States under a warmer climate as simulated by regional climate models, *Geophys. Res. Lett.,* **39,** L05803, doi:10.1029/2011GL050762.

Dudhia, J., 1989: Numerical study of convection observed during winter monsoon experiment using a mesoscale two–dimensional model. *J. Atmos. Sci*., **46,** 3077–3107.

Durack, P. J., S. E. Wijffels, and R. J. Matear, 2012: Ocean salinities reveal strong global water cycle intensification during 1950 to 2000. *Science,* **336,** 455–458.

Easterling, D. R., T. R. Karl, K. P. Gallo, D. A. Robinson, K. E. Trenberth, and A. Dai, 2000a: Observed climate variability and change of relevance to the biosphere. *J. Geophys. Res.,* **105,** 101–114.

Eltahir E. A. B., and J. S. Pall, 1996: Relationship between surface conditions and subsequent rainfall in convective storms. *J. Geophys. Res.,* **101,** 26237–26245.

Emori, S., and S. J. Brown, 2005: Dynamic and thermodynamic changes in mean and extreme precipitation under changed climate. *Geophys. Res. Lett.,* **32,** L17706, doi:10.1029/ 2005GL023272.

Emori, S., A. Hasegawa, T. Suzuki, and K. Dairaku, 2005: Validation, parameterization dependence, and future projection of daily precipitation simulated with a high-resolution atmospheric GCM, *Geophys. Res. Lett.,* **32,** L06708, doi:10.1029/2004GL022306.

European Centre for Medium-Range Weather Forecasts, 2002: The ERA-40 archive. Reading, ECMWF, **40**.

Field, C. B., et al. Eds., 2012: Summary for policymakers, in: Managing the Risks of Extreme Events and Disasters to Advance Climate Change Adaptation. A Special Report of Working Groups I and II of the Intergovernmental Panel on Climate Change, pp. 1–19, Cambridge Univ. Press, Cambridge, U. K.

Folland, K. C., T. N. Palmer, and D. E. Parker, 1986: Sahel rainfall and worldwide sea temperatures. *Nature*, **320,** 602–607.

Fontaine, B., P. Roucou, and S. Trzaska, 2003: Atmospheric water cycle and moisture fluxes in the West African monsoon: Mean annual cycles and relationship using NCEP/NCAR reanalysis. *Geophys. Res. Lett.,* **30,** 1117, doi:10.1029/2002GL015834.

Fontaine, B., and S. Bigot, 1993: West African rainfall deficits and sea surface temperatures. *Int. J. Climatol.,* **13,** 271–285.

Fritsch, J. M., R. J. Kane, and C. R. Chelius, 1986: The contribution of mesoscale convective weather systems to the warm season precipitation in the United States. *J. Climate Appl. Meteor.*, **25,** 1333–1345.

Gasse, F., and E. Van Campo, 1994: Abrupt postglacial climate events in West Asia and North– Africa monsoon domains. *Earth Planet Sci. Lett.,* **126,** 435–456.

Gastineau, G., L. Li, and H. Le Trent, 2009: The Hadley and Walker circulation changes in global warming conditions described by idealized atmospheric simulations. *J. Climate,* **22,** 3993–4013.

Gordon, H. B., P. H. Whetton, A. B. Pittock, A. M. Fowler, and M. R.Haylock, 1992: Simulated changes in daily rainfall intensity due to the enhanced greenhouse effect: Implications for extreme rainfall events. *Climate Dyn.,* **8,** 83–102.

Grist, J. P., and S. E. Nicholson, 2001: A study of the dynamic factors influencing the rainfall variability in the west African Sahel. *J. Climate*, **14,** 1337–1359.

Grodsky, S. A., J. A. Carton, and S. Nigam, 2003: Near surface westerly wind jet in the Atlantic ITCZ. *Geophys. Res. Lett.*, **30,** 2009, doi: 10.1029/2003GL017867.

Groisman, P., R. Knight, D. Easterling, T. Karl, G. Hegerl, and V. Razuvaev, 2005: Trends in Intense Precipitation in the Climate Record, *Journal of Climate,* **18,** 1326-1350.

Gu, Y., K. N. Liou, J. H. Jiang, H. Su, and X. Liu, 2012: Dust aerosol impact on North Africa climate: a GCM investigation of aerosol-cloud-radiation interactions using A-Train satellite data. *Atmos. Chem. Phys.*, **12,** 1667–1679.

Hagos, S., and C. Zhang, 2010: Diabatic heating, divergent circulation and moisture transport in the African Monsoon System. *Quart. J. Roy. Meteor. Soc.,* **136,** 411–425.

Hagos, S. M., and K. H. Cook, 2008: Ocean warming and late–twentieth century Sahel drought and recovery. *J. Climate*, **21,** 3797–3814.

Hagos, S. M., and K. H. Cook, 2007: Dynamics of the West African monsoon jump. *J. Climate,* **20,** 5264–5284.

Hastenrath, S., and D. Polzin, 2011: Long–term variations of circulation in the tropical Atlantic sector and Sahel rainfall. *Int. J. Climatol.,* **31,** 649–655.

Hastenrath, S., and P. J. Lamb, 2004: Climate dynamics of atmo sphere and ocean in the equatorial zone: A synthesis. *Int. J Climatol.,* **24,** 1601–1612.

Hastenrath, S., 2001: In search of zonal circulations in the equatorial Atlantic sector from the NCEP–NCAR reanalysis. *Int. J. Climatol.,* **21,** 37–47.

Hegerl, G. C., F. W. Zwiers, and P. A. Stott, and V. V. Kharin, 2004: Detectability of anthropogenic changes in temperature and precipitation extremes. *J. Climate,* **17**, 3683–3700.

Held, I. M., and B. J. Soden, 2006: Robust responses of the hydrological cycle to global warming. *J. Climate,* **19,** 5686–5699.

Held, I. M., T. L. Delworth, J. Lu, K. L. Findell, and T. R. Knutson, 2005: Simulation of Sahel drought in the 20th and 21st centuries. *Proc. Natl. Acad. Sci.,* **102,** 17,891–17,896.

Held, I. M., and B. J. Soden, 2000: Water vapor feedback and global warming. *Annu. Rev. Energy Environ.,* **25,** 441–475.

Hong, S.-Y., Y. Noh, and J. Dudhia, 2006: A new vertical diffusion package with explicit treatment of entrainment processes. *Mon. Wea. Rev.,* **134,** 2318–2341.

Hong, S., and E. Kalnay, 2000: Role of sea surface temperature and soil-moisture feedback in the 1998 Oklahoma–Texas drought. *Nature,* **408,** 842–844.

Houghton R. W., and C. Colin, 1986: Thermal structure along 4°W in the Gulf of Guinea during 1983–1984, *J. Geophys. Res.,* **91,** CIO, 11727–11739.

Huffman G. J., and D. T. Bolvin, 2013: TRMM and other data precipitation data set documentation. ftp://rsd.gsfc.nasa.gov/pub/trmmdocs/ 3B42_3B43_doc.pdf.

Huffman G. J., R. F. Adler, D. T. Bolvin, and G. Gu, 2009: Improving the global precipitation record: GPCP Version 2.1. *Geophys Res Lett* 36:L17808. doi:10.1029/2009GL040000.

IPCC, 2000: Emissions Scenarios, Nakicenovic N, Swart R Eds., Cambridge University Press, Cambridge, UK: 570pp.

Janjic, Z. I., 2002: Nonsingular implementation of the Mellor–Yamada Level 2.5 Scheme in the NCEP Meso model. NCEP Office Note No. 437, 61.

Janjic, Z. I., 1996: The surface layer in the NCEP eta model in the eleventh conference on numerical weather prediction, Norfolk, VA, 19–23 August 1996. *Amer. Meteor. Soc.,* Boston, MA, 354–355.

Janjic, Z. I., 1994: The step–mountain eta coordinate model: Further developments of the convection, viscous sub–layer and turbulence closure schemes. *Mon Weather Rev.,* **122,** 927–945.

Janjic, Z. I., 1990: The step–mountain coordinate–physical package. *Mon Weather Rev.,* **118,** 1429–1443.

Joseph, R., and N. Zeng, 2011: Seasonally modulated tropical drought induced by volcanic aerosol. *J. Climate,* **24,** 2045–2060.

Kain, J. S., and J. M. Fritsch, 1993: Convective parameterization for mesoscale models: The Kain–Fritsch scheme, in The Representation of Cumulus Convection in Numerical Models, edited by K. A. Emanuel and D. J. Raymond. *Meteorol. Monogr. Ser.,* **24,** 165–170.

Kain, J. S., and J. M. Fritsch, 1990: A one–dimensional entraining/ detraining plume model and its application in convective parameterization. *J. Atmos. Sci.,* **47,** 2784–2802.

Kalnay, E., et al., 1996: The NCEP/NCAR 40–year reanalysis project. *Bull. Amer. Meteoro. Soc.*, **77,** 437– 471.

Kanamitsu M., W. Ebisuzaki, J. Woollen, S-K. Yang, J.J. Hnilo, M. Fiorino, and G. L. Potter, 2002: NCEP-DOE AMIP-II reanalysis (R-2). *Bull. Am. Meteorol. Soc.,* **83**, 1631–1643.

Kharin, V. V., and F. W. Zwiers, 2000: Changes in the extremes in an ensemble of transient climate simulations with a coupled atmosphere–ocean GCM. *J. Climate,* **13,** 3760–3788.

Kitoh, A., M. Hosaka, Y. Adachi, and K. Kamiguchi, 2005: Future projections of precipitation characteristics in East Asia simulated by the MRI CGCM2. *Adv. Atmos. Sci.,* **22,** 467–478.

Knaff, J. A., 1997: Implications of summertime sea level pressure anomalies in the tropical Atlantic region. *J. Climate,* **10,** 789–804.

Kobayashi, S., M. Matricardi, D. Dee, and S. Uppala, 2009: Toward a consistent reanalysis of the upper stratosphere based on radiance measurements from SSU and AMSU–A. Quart. *J. Roy. Meteor. Soc.*, **135,** 2086–2099.

Kummerow, C ., W. Barnes, T . Kozu, J. Shiue, and J. Simpson, 1998: The Tropical Rainfall Measuring Mission (TRMM) sensor package. *J . Atmos. Ocean. Tech.*, **15,** 809–817.

Lau, K.–M., and S. Yang, 2003: Walker circulation. Encyclopedia of Atmospheric Sciences, J. R.

Leduc-Leballeur, M., G. de Coëtlogon, and L. Eymard, 2013: Air– sea interaction in the Gulf of Guinea at intraseasonal timescales: Wind bursts and coastal precipitation in boreal spring. Quart. J. Roy. Meteor. Soc., 139, 387–400, doi:10.1002/qj.1981.

Holton, J. A. Pyle, and J. A. Curry, Eds., Academic Press, 2505–2510.

Li, K. Y., M. T. Coe, N. Ramankutty, and R. DeJong, 2007: Modeling the hydrological impact of land–use change in West Africa. *J. Hydrology,* **337,** 258–268.

Liang, X.-Z., L. Li, K. Kunkel, M. Ting, and J. X. L. Wang, 2004: Regional climate simulations of U.S. precipitation during 1982–2002. Part I: Annual cycle. *J. Climate,* **17,** 3510–3529.

Lin, J. C., T. Matsui, R. A. Pielke Sr., and C. Kummerow, 2006: Effects of biomass-burning-derived aerosols on precipitation and clouds in the Amazon Basin: A satellite-based empirical study. *J. Geophys. Res.,* **111,** D19204, doi:10.1029/2005JD006884.

Lin, Y. L., R. D. Farley, and H. D. Orville, 1983: Bulk parametrization of the snow field in a cloud model. *J. Appl. Meteorol.,* **22,** 1065–1092.

Liu, Y., and J. C. H. Chiang, 2012: Coordinated abrupt weakening of the Eurasian and North African monsoons in the 1960s and links to extratropical North Atlantic cooling. *J. Climate, **25,** 3532-3548.*

Losada, T., B. Rodriguez–Fonseca, S. Janicot, S. Gervois, F. Chauvin, and P. Ruti, 2010: A multi–model approach to the Atlantic Equatorial mode. Impact on the West African monsoon. *Climate Dyn.,* **35,** 29–43.

Lowell, T., and Coauthors, 2005: Testing the Lake Agassiz meltwater trigger for the Younger Dryas. *Eos, Trans. Amer. Geophys. Union,* **86,** doi:10.1029/2005EO400001.

Manabe, S., and R. T. Wetherald, 1975: The effect of doubling CO2 concentration on the climate of the general circulation model. *J. Atmos. Sci.,* **32,** 3–15.

Manabe, S., and R. T. Wetherald, 1967: Thermal equilibrium of the atmosphere with a given distribution of relative humidity. *J. Atmos. Sci.,* **24,** 241–259.

Maynard, K., J. Royer, and F. Chauvin, 2002: Impact of greenhouse warming on the West African summer monsoon. *Climate Dyn.,* **19,** 499–514.

McManus, J. F., R. Francois, J.-M. Gherardi, L. D. Keigwin, and S. Brown-Leger, 2004: Collapse and rapid resumption of Atlantic meridional circulation linked to deglacial climate changes. *Nature*, **428,** 834–837.

Meehl, G. A., C. Covey, T. Delworth, M. Latif, B. McAvaney, J. F. B. Mitchell, R. J. Stouffer, and K. E. Taylor, 2007: The WCRP CMIP3 multi-model dataset: A new era in climate change research. *Bull. Amer. Meteor. Soc.*, **88**, 1383-1394. doi:10.1175/BAMS-88-9-1383.

Meehl, G. A., F. Zwiers, J. Evans, T. Knutson, L. Mearns, and P. Whetton, 2000: Trends in extreme weather and climate events: Issues related to modeling extremes in projections of future climate change. *Bull. Amer. Meteor. Soc.*, **81,** 427–436.

Mellor, G. L., and T. Yamada, 1982: Development of a turbulence closure model for geophysical fluid problems. *Rev. Geophysics and Space Phys.*, **20,** 851–875.

Mesinger F. et. al., 2006: North American regional reanalysis. *Bull. Am. Meteorol. Soc.* **87**, 343–360.

Merle, J., 1980: Seasonal heat budget in the equatorial Atlantic ocean. *J. Phys. Oceanogr.*, **10,** 464–469.

Mitas, C. M., and A. Clement, 2005: Has the Hadley cell been strengthening in recent decades? *Geophys. Res. Lett.*, **32,** L03809, doi:10.1029/2004GL021765.

Mitchell, T. D., and P. D. Jones, 2005: An improved method of constructing a database of monthly climate observations and associated high–resolution grids. *Int. J. Climatol.*, **25,** 693– 712.

Mitchell, J. F. B., T. C. Johns, J. M. Gregory, and S. F. B. Tell, 1995: Climate response to increasing levels of greenhouse gases and sulfate aerosols. *Nature,* **376,** 501–504.

Mlawer, E. J., S. J. Taubman, P. D. Brown, M. J. Iacono, and S. A. Clough, 1997: Radiative transfer for inhomogeneous atmosphere: RRTM, a validated correlated–k model for the longwave. *J. Geophys.Res.*, **102,** 16,663–16,682.

Mo, K., G. D. Bell, and W. M. Thiaw, 2001: Impact of sea surface temperature anomalies on the Atlantic tropical storm activity and West African rainfall. *J. Atmos. Sci.,* **58,** 3477–3496.

Mohino, E., S. Janicot, and J. Bader, 2011a: Sahel rainfall and decadal to multi-decadal sea surface temperature variability. *Climate Dyn.,* **37,** 419–440.

Mohino, E., B. Rodríguez-Fonseca, C. R. Mechoso, S. Gervois, P. Ruti, and F. Chauvin, 2011b: Impacts of the tropical Pacific/Indian oceans on the seasonal cycle of the West African monsoon. *J. Climate,* **24,** 3878–3891.

Monin, A. S., and A. M. Obukhov, 1954: Basic laws of turbulent mixing in the surface layer of the atmosphere. *Contrib. Geophys. Inst. Acad. Sci. USSR.,* **151,**163–187.

Monnin, E., A. Indermühle, A. Dällenbach, J. Flückiger, B. Stauffer, T. F. Stocker, D. Raynaud, and J.-M. Barnola, 2001: Atmospheric CO2 concentrations over the last glacial termination. *Science,* **291,** 112–114.

Neupane, N., and K. H. Cook, 2013: A nonlinear response of Sahel rainfall to Atlantic warming. *J. Climate,* **26,** 7080–7096, doi:10.1175/JCLI–D–12–00475.1.

Nicholson, S. E., 2009: A revised picture of the structure of the ‘‘monsoon’’ and land ITCZ over West Africa. *Climate Dyn.,* **32,** 1155–1171.

Nicholson, S. E., and P. Webster, 2007: A physical basis for the interannual variability of rainfall in the Sahel. Quart. J. Roy. Meteor. Soc., **133,** 2065–2084.

Nicholson, S. E., and J. P. Grist, 2001: A conceptual model for understanding rainfall variability in the West African Sahel on interannual and interdecadal timescales. *Int. J. Climatol.,* **21,** 1733–1757.

Nicholson, S. E., 2000: Land surface processes and Sahel climate. *Rev. Geophys.,* **38,** 117–139.

Noda, A., and T. Tokioka, 1989: The effect of doubling the CO2 concentration on convective and non-convective precipitation in a general circulation model coupled with a simple mixed layer ocean model. *J. Meteor. Soc. Japan,* **67,** 1057–1069.

Nolan, D. S., C. Zhang, and S. H. Chen, 2007: Dynamics of the shallow meridional circulation around intertropical convergence zones. *J. Atmos. Sci.,* **64,** 2262–2285.

O'Gorman, P. A., and C. J. Muller, 2010: How closely do changes in surface and column water vapor follow Clausius-Clapeyron scaling in climate change simulations? *Environ. Res. Lett., **5,** 025207,doi:10.1088/1748-9326/5/2/025207.*

O'Gorman, P. A., and T. Schneider, 2009a: The physical basis for increases in precipitation extremes in simulations of 21st-century climate change. *Proc. Natl. Acad. Sci.* USA, **106,** 14773–14777.

Paeth, H., and P. Friederichs, 2004: Seasonality and time scales in the relationship between global SST and African rainfall. *Climate Dyn.,* **23,** 815–837.

Pal, J. S., and E. A. B. Eltahir, 2001: Pathways relating soil moisture conditions to future summer rainfall within a model of the land–atmosphere system. *J. Climate,* **14,** 1227–1242.

Pall, P., M. R. Allen, and D. A. Stone, 2007: Testing the Clausius- Clapeyron constraint on changes in extreme precipitation under CO2 warming. *Climate Dyn.,* **28**, 351–363.

Patricola C. M. and K. H. Cook, 2013a: Mid-twenty-first century warm season climate change in the central United States. Part I: Regional and global model predictions. *Climate Dyn.,* **40,** 551–568.

Patricola C. M. and K. H. Cook, 2013b: Mid-twenty-first century warm season cli mate change in the central United States. Part II: Climate change processes. *Climate Dyn.,* **40,** 569–83.

Patricola, C. M., and K. H. Cook, 2011: Sub–Saharan Northern African climate at the end of the twenty–first century: Forcing factors and climate change processes. *Climate Dyn.,* **37,** 1165–1188.

Patricola, C. M., and K. H. Cook, 2010: Northern African climate at the end of the twenty–first century: An integrated application of regional and global climate models. *Climate Dyn.*, ***35,*** 193–212.

Patricola, C. M., and K. H. Cook, 2008: Atmosphere/vegetation feedbacks: A mechanism for abrupt climate change over northern Africa. *J. Geophys. Res.*, **113,** D18102, doi: 10.1029/2007JD009608.

Peck, J. A., R. R. Green, T. Shanahan, J. W. King, J. T. Overpeck, and C. A. Scholz, 2004: A magnetic mineral record of Late Quaternary tropical climate variability from Lake Bosumtwi, Ghana. *Palaeogeogr. Palaeoclimatol. Palaeoecol.*, **215,** 37–57.

Petit–Maire, N., and Z. Guo, 1996: Miseen evidence de variations climatiques holocenes rapides, en phase dans les deserts actuels de Chine et du Nord de lAfrique. *Sciences de la Terre et des Planetes*, **322,** 847–851.

Peixoto, J. P., and A. H. Oort, 1996: The climatology of relative humidity in the atmosphere. *J. Climate*, **9,** 3443–3463.

Pu, B., E. K. Vizy, and K. H. Cook, 2012: Warm season response over North America to a shutdown of the Atlantic meridional overturning circulation and CO_2 increases. *J. Climate,* **25,** 6701-6720.

Pu, B., and K.H. Cook, 2011: Role of the West African westerly jet in Sahel rainfall variations. *J. Climate*, **25**, 2880–2896.

Pu, B., and K.H. Cook, 2010: Dynamics of the West African westerly jet. *J. Climate,* **23,** 6263-6276.

Rangwala I. and J. R. Miller, 2012: Climate change in mountains: a review of elevation-dependent warming and its possible causes. *Clim Chang*, **114**, 527–547.

Richter, I., and S.-P. Xie, 2008: The muted precipitation increase in global warming simulations: A surface evaporation perspective. *J. Geophys. Res.,* **113,** D24118, doi:10.1029/2008JD010561.

Rienecker, M., and Coauthors, 2011: MERRA: NASA's Modern–Era Retrospective Analysis for Research and Applications. *J. Climate*, **24,** 3624–3648.

Royer, J.-F., F. Chauvin, B. Timbal, P. Araspin, and D. Grimal, 1998: A GCM study of the impact of greenhouse gas increase on the frequency of occurrence of tropical cyclones. *Climate Change,* **38,** 307–343.

Ross, R. J., and W. P. Elliott, 1996: Tropospheric water vapor climatology and trends over North America: 1973–93. *J. Climate,* **9,** 3561–3574.

Russell, J., M. Talbot, and B. Haskell, 2003: Mid-Holocene climate change in Lake Bosumtwi, Ghana. *Quat. Res.,* **60,** 133–141.

Rutledge, S. A., and P. V. Hobbs, 1984: The mesoscale and microscale structure and organization of clouds and precipitation in midlatitude cyclones. Part XII: A diagnostic modeling study of precipitation development in narrow cloud-frontal rainbands. *J. Atmos. Sci.,* **41,** 2949– 2972.

Seager, R., N. Naik, and G. A. Vecchi, 2010: Thermodynamic and dynamic mechanisms for large-scale changes in the hydrological cycle in response to global warming. *J. Climate,* **23,** 4651–4668.

Semenov, V. A., and L. Bengtsson, 2002: Secular trends in daily precipitation characteristics: Greenhouse gas simulation with a coupled AOGCM. *Clim. Dyn*., **19**, 123–140.

Sherwood, S. C., W. Ingram, Y. Tsushima, M. Satoh, M. Roberts, P. L. Vidale, and P. A. O'Gorman, 2010: Relative humidity changes in a warmer climate. *J. Geophys. Res.*, **115,** D09104, doi:10.1029/2009JD012585.

Simmonds, I., D. Bi, and P. Hope, 1999: Atmospheric water vapor flux and its association with rainfall over China in summer. *J. Climate,* **12,** 1353–1367.

Simmonds, I., and P. Hope, 1998: Seasonal and regional responses to changes in Australian soil moisture conditions. *Int. J. Climatol.,* **10,** 1105–1139.

Simmons, A., S. Uppala, D. Dee, and S. Kobayashi, 2007: ERA–Interim: New ECMWF reanalysis products from 1989 onwards. ECMWF Newsletter, No. 110, ECMWF, Reading, United Kingdom, 25–35.

Sillmann, J., V. V. Kharin, X. Zhang, F. W. Zwiers, and D. Bronaugh, 2013: Climate extreme indices in the CMIP5 multi-model ensemble: Part 1: Model evaluation in the present climate. *J. Geophys. Res. Atmos.,* **118,** 1716–1733, doi:10.1002/ jgrd.50203.

Singh, D., M. Tsiang, B. Rajaratnam, and N. Diffenbaugh, 2013: Precipitation extremes over the continental United States in a transient, high resolution, ensemble climate model experiment. *Journal of Geophysical Research: Atmospheres,* **118,** 7063-7086.

Skamarock, W. C., J. B. Klemp, J. Dudhia, D. O. Gill, D. M. Barker, M. G. Duda, X.-Y. Huang, W. Wang and J. G. Powers, 2008: A description of the advanced research WRF version . NCAR/TN-475+STR, National Center for Atmospheric Research, 112 pp.

Soden, B. J., D. L. Jackson, V. Ramaswamy, M. D. Schwarzkopf, and X. Huang, 2005: The radiative signature of upper tropospheric moistening. *Science,* **310,** 841–844.

Stager, J. C., D. B. Ryves, B. M. Chase, and F. S. R. Pausata, 2011: Catastrophic drought in the Afro-Asian monsoon region during Heinrich event 1. *Science,* **331,**1299-1302.

Stephens, G. L., and T. D. Ellis, 2008: Controls of global-mean precipitation increases in global warming GCM experiments. *J. Climate,* **21,** 6141–6155.

Lett., **5,** 025207, doi:10.1088/1748-9326/5/2/025207.

Thorncroft, C. D., N. Hanh, C. D. Zhang, and P. Peyrille, 2011: Annual cycle of the West African monsoon: Regional circulations and associated water vapour transport. *Quart. J. Roy. Meteor. Soc.,* **137,** 129–147.

Thorncroft CD, and M. Blackburn, 1999: Maintenance of the African easterly jet. *Q. J. R. Meteorol. Soc.* **125**: 763–786.

Timm, O., P. Kohler, A. Timmermann, and L. Menviel, 2010: Mechanisms for the onset of the African Humid Period and Sahara greening 14.5-11 ka BP. *J. Climate,* **23,** 2612-2633.

Trenberth, K.E., P.D. Jones, P. Ambenje, R. Bojariu, D. Easterling, A. Klein Tank, D. Parker, F. Rahimzadeh, J.A. Renwick, M. Rusticucci, B. Soden and P. Zhai, 2007: Observations: Surface and Atmospheric Climate Change. In: *Climate Change 2007: The Physical Science Basis*. Contribution of Working Group I to the Fourth Assessment Report of the Intergovernmental Panel on Climate Change [Solomon, S., D. Qin, M. Manning, Z. Chen, M. Marquis, K.B. Averyt, M. Tignor and H.L.

Miller (eds.)]. Cambridge University Press, Cambridge, United Kingdom and New York, NY, USA.

Trenberth, K. E., and D. P. Stepaniak, 2003: Seamless poleward atmospheric energy transports and implications for the Hadley circulation. *J. Climate,* **16,** 3706–3722.

Trenberth, K. E., and D. P. Stepaniak, and J. M. Caron, 2000: The global monsoon as seen through the divergent atmospheric circulation. *J. Climate,* **13,** 3969–3993.

Uppala, S. M., D. Dee, S. Kobayashi, P. Berrisford, and A. Simmons, 2008: Towards a climate data assimilation system: Status update of ERA–Interim. ECMWF Newsletter, No. 115, ECMWF, Reading, United Kingdom, 12–18.

Uppala, S. M., et al., 2005: The ERA–40 re–analysis. *Q. J. R. Meteorol. Soc*., **131,** 2961–3012.

Vecchi, G. A., and B. J. Soden, 2007: Increased tropical Atlantic wind shear in model projections of global warming. *Geophys. Res. Lett.,* **34,** L08702, doi:10.1029/2006GL028905.

Vizy, E. K., and K. H. Cook, 2014: Capturing the Atlantic cold tongue and coastal upwelling in an intermediate–level ocean model coupled to a regional climate model. *Clim. Dyn.*, doi:10.1007/s00382–013–1807–8.

Vizy, E. K., K.H. Cook, J. Crétat, and N. Neupane, 2012: 21st century climate prediction for West Africa and the Sahel. Accepted for *J. Climate.*

Vizy, E. K., and K. H. Cook, 2002: Development and application of a mesoscale climate model for the tropics: Influence of sea surface temperature anomalies on the West African monsoon. *J. Geophys. Res.,* **107,** 4023, doi: 10.1029/2001JD000686.

Vizy, E. K., and K. H. Cook, 2003: Connections between the summer east African and Indian rainfall regimes. *J. Geophys. Res.,* **108,** 4510, doi: 10.1029/2003JD003452.

Vizy, E. K., and K. H. Cook, 2001: Mechanisms by which Gulf of Guinea and eastern North Atlantic sea surface temperature anomalies can influence African rainfall. *J. Climate,* **14,** 795–821.

Wang, C., 2006: An overlooked feature of tropical climate: Inter– Pacific–Atlantic variability. *Geophys. Res. Lett.,* **33,** L12702 doi:10.1029/2006GL026324.

Wang, C., 2005: ENSO, Atlantic climate variability, and the Walker and Hadley circulations. *The Hadley Circulation: Past, Present, and Future,* H. F. Diaz and R. S. Bradley, Eds., Kluwer Academic, 173–202.

Wang, C., 2004: ENSO, Atlantic climate variability, and the Walker and Hadley circulations. The Hadley Circulation: Past, Present and Future, H. F. Diaz and R. S. Bradley, Eds.,Advances in Global Change Research, Vol. 21, Kluwer Academic Publishers, 85–120.

Wang, C., 2002a: Atlantic climate variability and its associated atmospheric circulation cells. *J. Climate,* **15,** 1516–1536.

Wang, C., 2002b: Atmospheric circulation cells associated with the El Niño–Southern Oscillation. *J. Climate,* **15,** 399–419.

Ward, M. N., 1998: Diagnosis and short–lead time prediction of summer rainfall in tropical North Africa at interannual and multidecadal timescales. *J. Climate,* **11,** 3167–3191.

Watterson, I. G., and M. R. Dix, 2003: Simulated changes due to global warming in daily precipitation means and extremes and their interpretation using the gamma distribution. *J. Geophys. Res*., **108** (D13), 4379, doi:10.1029/2002JD002928.

Watterson, I. G., 1998: An analysis of the global water cycle of present and doubled CO2 climates simulated by the CSIRO general circulation model, *J. Geophys. Res.,* **103,** 23,113– 23,129.

Wentz, F. J., L. Ricciardulli, K. Hilburn, and C. Mears, 2007: How much more rain will global warming bring? *Science,* **317,** 233–235.

White, J. W. C., P. Ciais, R. A. Figge, R. Kenny, and V. Markgraf , 1994: A high-resolution record of atmospheric CO2 content from carbon isotopes in peat. *Nature,* **367,** 153-156.

Wilby, R. L., and T. M. L. Wigley, 2002: Future changes in the distribution of daily precipitation totals across North America. *Geophys. Res. Lett.,* **29,** 1135, doi:10.1029/2001GL013048.

Wu Y., S. Liu, O. I. Abdul-Aziz, 2012: Hydrological effects of the increased CO2 and climate change in the Upper Mississippi River Basin using a modified SWAT. *Clim. Change* ,**110,** 977-1003.

Xie, S.-P., C. Deser, G. A. Vecchi, J. Ma, H. Teng, and A. T. Wittenberg, 2010: Global Warming Pattern formation: Sea surface temperature and rainfall. *J. Climate,* **23,** 966–986.

Zahn, M., and R. P. Allan, 2013: Climate warming related strengthening of the tropical hydrological cycle. *J. Climate,* **26,** 562–574.

Zhang, C. D., D. S. Nolan, C. D. Thorncroft, and H. Nguyen, 2008: Shallow meridional circulations in the tropical atmosphere. *J. Climate,* **21,** 3453–3470.

Zhang, C., P. Woodworth, and G. Gu, 2006: The seasonal cycle in the lower troposphere over West Africa from sounding observations. *Quart. J. Roy. Meteor. Soc.,* **132,** 2559–2582.

Zhao, C., X. Liu, L. R. Leung, and S. Hagos, 2011: Radiative impact of mineral dust on monsoon precipitation variability over West Africa. *Atmos. Chem. Phys.,* **11,** 1879–1893.

Zheng, X., and E. A. B. Eltahir, 1998: A soil moisture-rainfall feedback mechanism. 2. Experiments with a simple numerical model. *Water Resour. Res.,* **34,** 777–785.